HAL
open science

Structural insights into the catalytic cycle of a bacterial multidrug ABC efflux pump

Waqas Javed, Sylvain Vallet, Marie-Pierre Clement, Aline Le Roy, Martine Moulin, Michael Härtlein, Cécile Breyton, Odile Burlet-Schiltz, Julien Marcoux, Cédric Orelle, et al.

To cite this version:

Waqas Javed, Sylvain Vallet, Marie-Pierre Clement, Aline Le Roy, Martine Moulin, et al.. Structural insights into the catalytic cycle of a bacterial multidrug ABC efflux pump. Journal of Molecular Biology, 2022, 434 (9), pp.167541. 10.1016/j.jmb.2022.167541 . hal-03715136

HAL Id: hal-03715136
https://hal.science/hal-03715136

Submitted on 11 Oct 2022

HAL is a multi-disciplinary open access archive for the deposit and dissemination of scientific research documents, whether they are published or not. The documents may come from teaching and research institutions in France or abroad, or from public or private research centers.

L'archive ouverte pluridisciplinaire **HAL**, est destinée au dépôt et à la diffusion de documents scientifiques de niveau recherche, publiés ou non, émanant des établissements d'enseignement et de recherche français ou étrangers, des laboratoires publics ou privés.

Structural insights into the catalytic cycle of a bacterial multidrug ABC efflux pump

Waqas Javed[1,2,3], Sylvain Vallet[1], Marie-Pierre Clement[1], Aline Le Roy[2], Martine Moulin[3], Michael Härtlein[3], Cécile Breyton[2], Odile Burlet-Schiltz[4], Julien Marcoux*[4], Cédric Orelle*[1], Christine Ebel*[2], Anne Martel*[3] and Jean-Michel Jault*[1]

[1] Molecular Microbiology & Structural Biochemistry (MMSB) UMR 5086; CNRS/University of Lyon; Lyon, 69367; France. [2] IBS; Univ. Grenoble Alpes, CNRS, CEA; Grenoble, 38000; France. [3]Institut Max Von Laue Paul Langevin (ILL); Grenoble, 38000 ; France. [4]Institut de Pharmacologie et de Biologie Structurale ; Université de Toulouse, CNRS; Toulouse, 31000; France.

Further information and requests for resources and analysis should be directed to the lead contact, Jean-Michel Jault (jean-michel.jault@ibcp.fr). Correspondence: julien.marcoux@ipbs.fr; cedric.orelle@ibcp.fr; christine.ebel@ibs.fr; martela@ill.fr; jean-michel.jault@ibcp.fr

Summary

ABC ("ATP-Binding Cassette") transporters of the type IV subfamily consist of exporters involved in the efflux of many compounds, notably those capable to confer multidrug resistance like the mammalian P-glycoprotein or the bacterial transporter BmrA. They function according to an alternating access mechanism between inward-facing (IF) and outward-facing (OF) conformations, but the extent of physical separation between the two nucleotide-binding domains (NBDs) in different states is still unsettled. Small Angle Neutron Scattering and hydrogen/deuterium exchange coupled to mass spectrometry were used to highlight different conformational states of BmrA during its ATPase cycle. In particular, mutation of the conserved Lysine residue of the Walker-A motif (K380A) captures BmrA in an ATP-bound IF conformation prior to NBD closure. While in the transition-like state induced by vanadate wild-type BmrA is mainly in an OF conformation, the transporter populates only IF conformations in either the apo state or in the presence of ADP/Mg. Importantly, in this post-hydrolytic step, distances between the two NBDs of BmrA seem to be more separated than in the apo state, but they remain shorter than the widest opening found in the related MsbA transporter. Overall, our results highlight the main steps of the catalytic cycle of a homodimeric bacterial multidrug transporter and underline structural and functional commonalities as well as oddities among the type IV subfamily of ABC transporters.

Keywords

Small Angle Neutron Scattering, Hydrogen Deuterium exchange, membrane protein, multidrug transporter, ATP-binding cassette.

Introduction

ATP Binding Cassette (ABC) exporters are ATP-driven ubiquitous proteins that are involved in the translocation of many different compounds across membranes [1, 2]. They play key roles in many physiological functions and in humans their dysfunction is linked to several diseases including cystic fibrosis, tangier disease and Dubin-Johnson syndrome [3, 4]. Some ABC transporters can expel a wide array of molecules with unrelated chemical structures thereby protecting cells from noxious compounds. Hence, their overexpression in cancer cells or pathogens often result in multidrug resistant phenotypes leading to the failure of therapies [5, 6]. All ABC transporters share a common basic architecture including two nucleotide-binding domains (NBDs)[1] that bind and hydrolyze ATP, and two transmembrane domains (TMDs) that form the substrate translocation pathway [7]. Importantly, the 3D structure of exporters of the type IV subfamily reveals that the two intracellular domains (ICD1 and ICD2 in a homodimer) extending from the TMD and connecting the transmembrane helices 2 - 3 and 4 – 5, respectively, are key elements for the coupling between the TMDs and the NBDs. Hence, whereas ICD1 interacts with its own NBD, ICD2 interacts in *trans* with the NBD of the second monomer allowing a permanent cross-talk between the two monomers of homo- or hetero-dimers, or between the two moieties of full-length transporters [8]. The original postulate that ABC exporters of the type IV subfamily work according to an alternating access mechanism [9] is now supported by many pieces of evidence [10]; they switch between an apo state, or inward-facing (IF) conformation with the NBDs physically separated, to an outward-facing (OF) conformation prone to drug release and with the two NBDs engaged in a tight interaction while sandwiching two ATP molecules at their interface [6]. This transition from IF to OF states is triggered by ATP binding while ATP hydrolysis is supposed to reset the transporter to its IF conformation [7]. Yet, the extent of the NBD separation in IF conformations is still a matter of debate [11-13]. It may vary according to the intrinsic property of each transporter, i.e. its energy landscape that is possibly linked to the substrate transported [10], or even depends on the drug

[1] Abbreviations : AUC, Analytical UltraCentrifugation ; BmrA, *Bacillus* multidrug resistance ATP; Cryo-EM, Cryo-Electron Micropscopy; DDM, Dodecyl-β-D-maltoside; ICD, IntraCellular Domain; HDX-MS, H/D exchange coupled to mass spectrometry; IF, Inward Facing; LMNG, Lauryl Maltose Neopentyl Glycol ; MD, Molecular Dynamic; NBD, Nucleotide-Binding Domain ; OF, Outward Facing; Rg, radius of gyration; SANS, Small Angle Neutron Scattering; SEC-LS, Size Exclusion Chromatography coupled to Light Scattering; T_m, melting temperature; TMD, TransMembrane Domain; Vi, Vanadate; woIF, wide-open IF, WT, Wild-Type.

effluxed for multidrug transporters [14]. A large opening between the NBDs of MsbA has been observed by electron microscopy [15, 16], consistent with that found in X-ray structures [17, 18]. Molecular dynamic (MD) simulations also supports a large flexibility of MsbA in its resting state [19]. P-glycoprotein (P-gp), on the other hand, seems to be more constrained for the physical separation of its NBDs [15], yet a large fluctuation in the distance between its NBDs has been observed by MD simulation and EPR spectroscopy [20] and also by cryo-electron microscopy (Cryo-EM) [21]. For asymmetric ABC exporters with two non-equivalent NBDs, the opening in the IF conformation appears rather limited, even in the apo state [22-25]. In addition, the conformational landscape can be affected by the protein environment as well, i.e. detergent, nanodiscs or proteoliposomes [26], or the lipid composition [27].

Here, we investigated a multidrug ABC exporter from *Bacillus subtilis*, BmrA (*Bacillus* multidrug resistance ATP), which confers resistance *in vivo* to the cervimycin C antibiotic [28]. BmrA is a bacterial homologue of mammalian P-gp [29] and it functions as a homodimer [30]. It can be obtained in a detergent solubilized state in a very active ATPase form [31, 32]. H/D exchange coupled to mass spectrometry (HDX-MS) of BmrA in detergent micelles or solid-state NMR after reconstitution of the transporter into a lipidic environment highlighted two very different conformations in apo or ATP-trapped states [33, 34]. Our aim here was to identify and characterize additional conformational states of BmrA during its catalytic cycle to better understand its overall functioning mechanism. In particular, we sought to address IF conformations in the presence of nucleotides. For this purpose, we used the wild-type (WT) BmrA with ADP/Mg to characterize the post-hydrolytic step, and a mutant of the invariant Lysine of the Walker-A motif, K380A, as it was thought to be impaired in the NBD dimerization step [35]. We also took advantage of another ATPase inactive mutant, the E504Q. This glutamate residue is the putative catalytic base for ATPase activity in ABC transporters [36-39]. The inactive E504Q mutant can be trapped in a pre-hydrolytic ATP/Mg-bound state [33, 34, 39] and was compared to the transition-state conformation of WT reached upon vanadate inhibition (ATP/Mg/Vi) [38]. The different proteins were characterized by “in solution” techniques, mainly Small Angle Neutron Scattering (SANS) and HDX-MS, as they both have shown to nicely complement high resolution static

pictures obtained by X-ray crystallography, NMR or Cryo-EM [40, 41]. Overall, we present a dynamic view of the catalytic cycle of BmrA that switches between different IF conformations in the resting state, with a moderate opening between its two NBDs as compared to MsbA, to an OF conformation in the transition state similar to the ATP-bound state of the E504Q mutant. Importantly, in the post-hydrolytic ADP/Mg-bound state, the physical separation between the two NBDs of BmrA is increased as compared to the apo state shedding light on an essential feature of the catalytic cycle of this transporter.

Results

Thermal stability and limited proteolysis reveal that BmrA mutants can be arrested at different steps of the catalytic cycle. Figure 1 reports on the denaturation curves and melting temperatures (T_m) for WT and mutants of BmrA in the apo states, or in the presence of various nucleotides. For WT-ATP/Mg/Vi, a major increase in T_m is observed compared to the apo state, from ~ 44 to 58 °C.

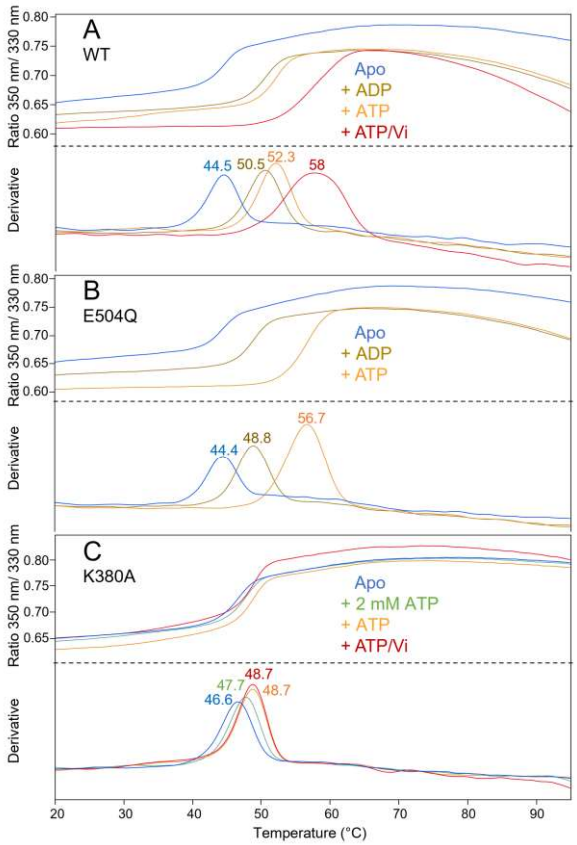

Figure 1. Thermal stability of WT BmrA and mutants and effect of nucleotides. Ratio of fluorescence emitted at 350 and 330 nm and first-derivatives with T_m (upper and lower sub-panels, respectively) for **A**: WT, wild-type BmrA. **B**: E504Q mutant and **C**: K380A mutant. Unless otherwise specified, ADP or ATP were added at 10 mM in the presence of 10 mM $MgCl_2$; When 2 mM ATP was used, 3 mM $MgCl_2$ were added; Vi was added at 1 mM. These experiments were reproduced at least three times from two different batches of purified proteins and with triplicate each time; a representative experiment is shown here.

The enhanced thermal stabilization induced by vanadate trapping is in agreement with previous results [32], and it is consistent with a large conformational change, as the protein switches from IF to OF conformations and remains trapped in this state. In the presence of ATP/Mg or ADP/Mg, the T_m is intermediate at 52 °C and 50 °C, respectively. In the former case, BmrA can hydrolyze ATP (until ADP has accumulated enough to inhibit ATPase activity) and is therefore switching between IF and OF conformations, whereas the binding of ADP/Mg produced an intermediate effect. The catalytically inactive E504Q BmrA mutant, in presence of ATP/Mg, shows an elevated T_m slightly lower than that of WT-ATP/Mg/Vi, providing further evidence of its trapping in the OF conformation [34, 39]. This result is in agreement with the recently solved 3D structure of the E504A mutant in an ATP-Mg bound state [42]. In the presence of ADP/Mg, this mutant shows a T_m similar to the WT. In contrast, the ATPase-inactive K380A mutant shows a modest, but significant, stabilization in the presence of ATP/Mg or ATP/Mg/Vi compared to the Apo form (> 2 °C). This suggests that the binding of ATP/Mg by the K380A, despite its weaker binding ability [35], does not produce a large conformational change, consistent with the assumption that this mutant is unable to reach the OF conformation.

Limited proteolysis was then performed to further analyze the global effect of nucleotides on our different constructs. As previously reported for the WT [32], incubation with ATP/Mg/Vi induced a full protection, up to 4 hours, against trypsin digestion (Figure 2, panels A-B).

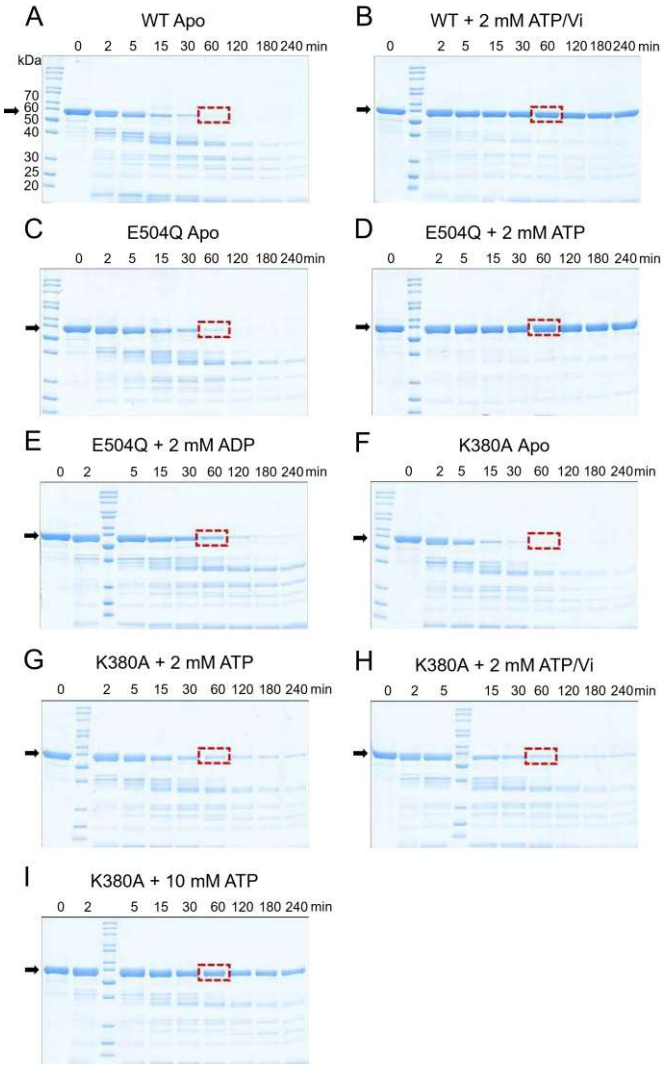

Figure 2. Limited proteolysis of K380A and E504Q mutants compared to WT BmrA. After incubation with the indicated ligands, BmrA WT (**A**-**B**), E504Q (**C**-**E**), or K380A mutants (**F**-**I**) were treated with trypsin for various times. $MgCl_2$ was added at 3 or 10 mM when 2 or 10 mM nucleotides were used, respectively. Vi was added at 1 mM. All samples were in 0.01% LMNG. Time zero was taken just before adding trypsin and the proteins were resolved using a 12% SDS PAGE. The arrows indicate the position of intact BmrA. Red boxes highlight the bands after 60 min of digestion. These experiments were reproduced at least three times from at least two different batches of purified proteins and a representative experiment is shown here.

A similar level of protection was afforded by ATP/Mg for the E504Q mutant while ADP/Mg showed a much-reduced effect (Figure 2, panels C-E). For the K380A mutant, a significant reduction in proteolysis digestion was obtained with 2 mM ATP/3 mM Mg, whether or not Vi was present, and this effect was strongly amplified in the presence of 10 mM ATP/Mg since about half of the proteins remained undigested (Figure 2, panels F-I). These experiments confirm the ability of this mutant to bind nucleotides when ATP is added in large excess, but they do not explain if the protection provided by ATP is due to a local (i.e. ATP binding to NBD) or a global effect on the whole protein (i.e.

conformational change due to NBD closure). To resolve this question, we performed SANS experiments on the different proteins, since this approach is particularly adapted to investigate global conformational changes of macromolecules in solution [41, 43, 44].

SANS data highlight the conformational states of BmrA WT and mutants. The SANS signals of WT BmrA, E504Q and K380A mutants at ~ 2 mg.mL^{-1} were recorded in the absence or presence of ligands, in conditions where the Lauryl Maltose Neopentyl Glycol (LMNG) detergent was invisible to neutrons, i.e. 21.4% D_2O, the contrast match point previously determined for this detergent [32]. BmrA proteins were partially deuterated by over-expression in a deuterated minimal media containing 85% D_2O and unlabeled glycerol as carbon source, to provide sufficient contrast with the partially deuterated buffer. A deuteration level of 67-72% of non-labile hydrogens was estimated for the three purified proteins by MALDI TOF (Table S1). The resulting SANS data therefore reveal the shape of the proteins only, while detergent molecules bound to the proteins remain invisible. Full details on SANS samples, measurements and analysis are given in Table S2.

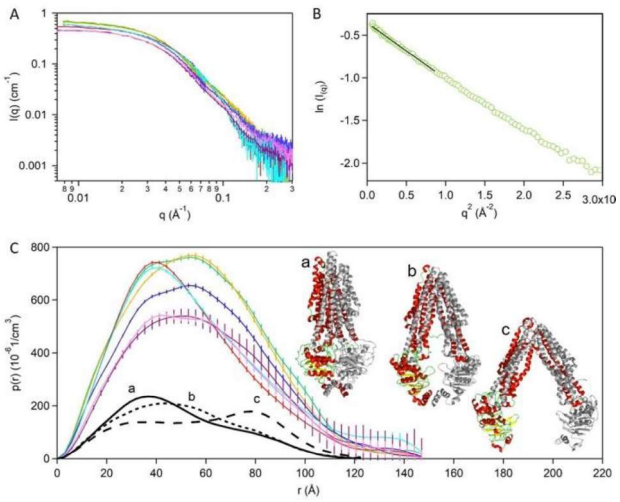

Figure 3. SANS data analysis. A: SANS scattering curves of WT BmrA in the apo state (green), or in the presence of ADP/Mg (yellow) and ATP/Mg/Vi (red), of the E504Q mutant in the apo state (blue) or in the presence of ATP/Mg (cyan), of the K380A mutant in the apo state (purple) or in the presence of ATP/Mg/Vi (pink). **B**: Example of Guinier fit for WT BmrA in the apo state. **C**: Pair distance distribution functions (p(r)) with the same color code as **A**. Note the p(r) are not normalized, the integral depends on sample concentration. Theoretical p(r) based on the PDB 6R81 structure of BmrA (continuous line, a), and on BmrA models built on PDB 3WME (dotted line, b) and 3B5W (discontinuous line, c) at 1 mg/mL. P(r) of BmrA homolog structures are given in Figure S1 for comparison. The error bars on the scattering data represent the uncertainty of each pixel (= sqrt counts / counts) propagated through the radial averaging.

At first glance, the flatness at low angle of all the raw scattering curves suggests the absence of aggregation (Figure 3**A**), as confirmed by the quality control experiments described below. The linearity of the Guinier plots (Figure 3**B**) is also consistent with sample homogeneity. From the Guinier plot, the radius of gyration, Rg, was obtained [43]. The Rgs are in the same range (44-45 Å) for the three proteins

in apo conditions, WT-ADP/Mg, and K380A-ATP/Mg/Vi, but are significantly lower (40 - 42.5 Å) for WT-ATP/Mg/Vi and E504Q-ATP/Mg (Table 1).

BmrA proteins	WT			E504Q		K380A	
conditions	Apo	ADP/Mg	ATP/Mg/Vi	Apo	ATP/Mg	Apo	ATP/Mg/Vi
Rg (Å)	44.3 ± 0.2	43.8 ± 0.3	40.3 ± 0.3	45.0 ± 0.3	42.5 ± 0.4	45.5 ± 0.5	44.3 ± 0.4
Max in p(r) (Å)	(41); 53	53	38	(40); 53	41	50	41; (59)

Table 1. Guinier and pair distribution analysis of BmrA samples in SANS. The precision for the p(r) maxima is ~ 2 Å. Values in parenthesis for the p(r) maxima indicate the position of shoulders.

For the K380A mutant with ATP/Mg, two samples were analyzed either in the presence or absence of vanadate. In view of the precision of the data, K380A-ATP/Mg and K380A-ATP/Mg/Vi had the same scattering curves (Figure S2), consistent with the lack of vanadate effect in the thermal stability assay (Figure 1) and the fact that this mutant was shown to be devoid of ATPase activity [35]. Due to a higher protein concentration, signal intensities were higher for the K380A-ATP/Mg/Vi experiment, and this condition was further processed.

Conditions where interactions between proteins are negligible (i.e. sample exempt of aggregates) are required to extract accurate information on protein structure from SANS data analysis. Sample quality was therefore checked after SANS measurement by analytical ultracentrifugation (AUC) or size exclusion chromatography coupled to light scattering (SEC-LS), showing >97-98% homogeneity (Figure S3) even after a couple of days of storage or freeze/thawing cycles, except for the E504Q mutant that displayed only 92% homogeneity. The corrected sedimentation coefficient, s_{20w} = 8.4 +/- 0.15 S, for WT BmrA in LMNG is in line with the 8.2 and 8.4 S values previously obtained for (hydrogenated) BmrA in LMNG [32] and Dodecyl-β-D-maltoside (DDM) [45], respectively. The molar masses of LMNG-BmrA complexes, derived from SEC-LS using a mean value between detergent and protein for the refractive index increment, are similar to the 240 kDa value found for hydrogenated BmrA [32] (Table S1). Melting temperatures of partially deuterated WT and E504Q BmrA, measured after SANS and AUC were 46.7 and 45.2 °C, respectively, comparable to that of the hydrogenated proteins (Figure 1). The specific activity for WT BmrA samples after SANS was ~ 0.9 µmol ATP hydrolyzed min^{-1} mg^{-1} protein, and it was inhibited at 98% by 200 µM Vi. In addition, the sample incubated in the presence

of ATP/Mg/Vi was still inhibited by ~ 88% after the SANS measurement, showing that the trapping of ADP/Mg/Vi was largely preserved throughout the experiment. Taken together, these features reveal that WT BmrA remains essentially either in an active or inhibited state during SANS data acquisition, depending on the ligands used for incubation, and that SANS data could be further processed.

The Fourier transform of the scattering data, p(r), results in the pair distance distribution functions and informs on the general shape of the molecule. The largest inter-atomic distance within the macromolecule, D_{max}, is determined as the large distance at which p(r) tends to be null. A globular compact protein will present a bell-shape p(r) with a well-defined maximum around $D_{max}/2$, whereas the presence of shoulders or asymmetric p(r) are indicative of multi-domain or elongated shapes [43]. The p(r) analysis of various BmrA samples clearly reveals different conformations (Figure 3**C**, Table 1). WT-ATP/Mg/Vi (red curve) and E504Q-ATP/Mg (cyan curve) display very similar p(r), with a maximum at ~ 40 Å, and very different from all other curves. This profile reflects smaller inter-atomic distances, which is compatible with an expected OF conformation. All the other samples show broader p(r) distributions, with the appearance of another maximum at ~ 53 Å, compatible with a non-compact shape, presumably an open IF conformation. The p(r) of WT-Apo and E504Q-Apo (green and blue curves, respectively) are indistinguishable in the relevant distance range. The p(r) of WT-ADP/Mg (yellow) is significantly different from that of WT-Apo, with a disappearance of the maximum at ~ 40 Å, leading to a distribution centered towards higher values. This suggests that the WT in the ADP/Mg bound state adopts, on average, a more open IF conformation than the apo state. In the presence of ATP/Mg/Vi, the K380A mutant (pink), which binds ATP but does not hydrolyze it [35], is much more open than WT-ATP/Mg/Vi (red) and E504Q-ATP/Mg (cyan), but appears to reside in an IF conformation, on average, more closed than in the apo state (purple). Because of low intensity features at large r (> 120 Å) in the E504Q mutant in the presence of ATP/Mg, possibly related to residual amounts of aggregates, it was not considered further for modelling. Apart from this, the quality of SANS data from all other samples were similar to the WT ones. The analyses in terms of conformations were thus performed on five sets of data from WT BmrA (apo, ATP/Mg/Vi and ADP/Mg) and K380A mutant (apo and ATP/Mg/Vi), as the E504Q mutant in its apo state was similar to that of the WT. The theoretical

p(r) derived from a high resolution structure of BmrA in the OF state (PDB 6R81; E504A BmrA mutant solved by cryo-EM;[42]), and from two models of the apo state of BmrA, are shown for comparison (Figure 3**C**, black curves); the latter are based on IF and wide-open IF (woIF) conformations of P-gp (PDB 3WME; [46]) and MsbA (PDB 3B5W, [17]), respectively. The p(r) of the OF structure, with a maximum at 37 Å is very similar to that of WT-ATP/Mg/Vi and E504Q-ATP/Mg. The maxima of the p(r) of the IF and woIF models are 44 and 77 Å, respectively. Because our experimental curves cannot be fitted satisfactorily with a single theoretical simulation, especially that with the largest opening between the two NBDs, BmrA presumably adopts an alternative conformation or an ensemble of different conformations.

The 3D shape derived from SANS data for the WT-ATP/Mg/Vi fits well the OF 3D structure. *Ab-initio* reconstruction of the 3D shape of a protein from its scattering curve is not trivial as different shapes can lead to the same curve, but the 3D structure of BmrA or homology models can help to narrow down the possibilities. The WT SANS curves were analyzed for their degree of ambiguity by the application "Ambimeter" to estimate whether they relate to a unique structure, or to several structures having a similar scattering signal [47]. Data from all samples were possibly ambiguous, except for WT-ATP/Mg/Vi (Table S2). An *ab*-initio reconstruction was therefore applied only to this data set. The resulting envelope, obtained by the program DAMMIN [48], is shown in Figure S4. It is superimposed with, and fits reasonably well, the 3D structure of the E504A BmrA mutant in an ATP-bound form (i.e. OF structure with closed NBDs; [42]). Some extra densities in the SANS envelope are, however, observed.

Multi-conformation fitting reveals BmrA flexibility in IF conformations and the absence of a woIF conformation. Because the ab-initio reconstruction of the other datasets (WT-Apo, WT-ADP/Mg, K380A-Apo and K380A-ATP/Mg/Vi) could not be reliably performed, we used instead another strategy to fit multiple conformations. The 3 models presented in Figure 3**C** were submitted to MULTIFOXS software to fit the data by adjusting the proportion of each of these 3 conformations [49]. However, no combination of the three models could fit satisfactorily the SANS data ($\chi^2 >> 1$). Thus, to address the possibility of protein flexibility in solution including intermediate openings of the NBDs, a large number

of additional conformations were generated *in silico.* A total of 7006 conformations, built as described in Figure S5 and in the method section, were used to fit the SANS data with MULTIFOXS, either individually or as ensemble of two, three and four conformations with variable proportions. Following this principle, all data sets could be reasonably well fitted ($\chi^2 \sim 1$) by an equilibrium between two main conformations. Figure 4 (panels **A** to **E**) shows a representative conformational set together with data fit.

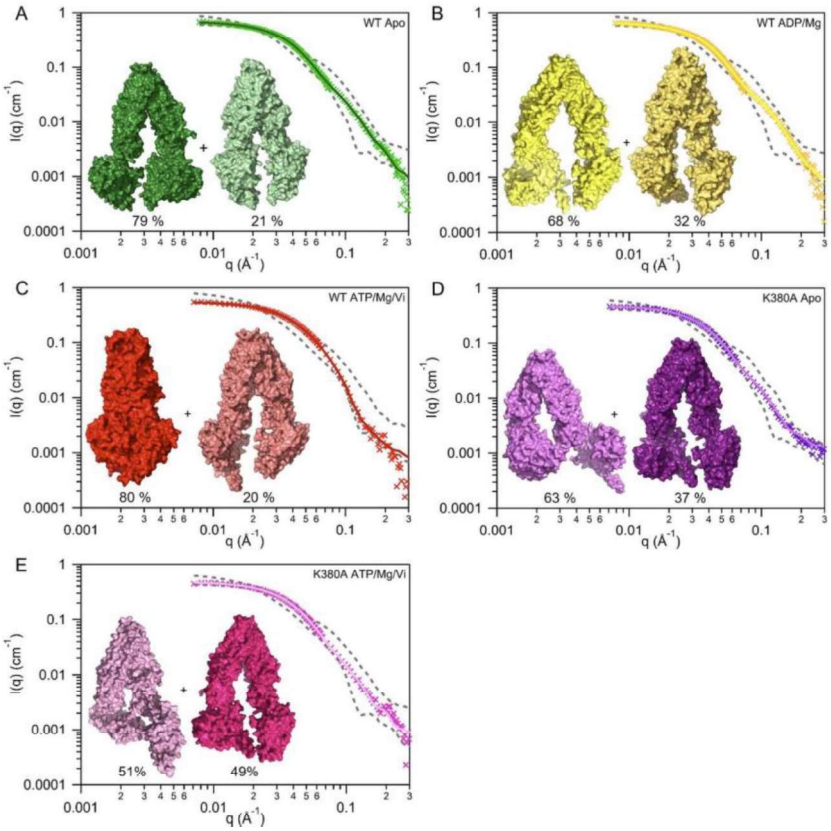

Figure 4. Multi-conformation fits of SANS data using Multifoxs. Each graph shows the best fit of SANS data with two conformations of WT-apo (**A**), WT-ADP/Mg (**B**), WT-ATP/Mg/Vi (**C**), K380A-apo (**D**) and K380A-ATP/Mg/Vi (**E**), together with the two modelled conformations combined to obtain the fit, and their relative proportion. Other conformation pairs fitting equally well the data are presented in figure S6. After the fitting process, the His-tag has been removed from the picture for clarity. On each fit, the grey dash lines show, for each Q-value, the minimum and maximum intensities from the calculated curves of the 7006 possible conformations.

However, several pairs of conformations fit the data equally well (similar χ^2) and they are presented in supplementary information (Figure S6). To estimate the degree of opening/closure between the two TMDs of BmrA homodimer, we measured distances between E212 residues in each monomer (Figure S6). This residue is located at the apex of ICD2 that links transmembrane helices 4 and 5, and is equivalent to G201 (TM287) and G225 (TM288) that were used earlier to visualize the opening between NBDs in different 3D structures of ABC exporters [10]. As a comparison, the distance between these residues in the woIF and IF models and in the OF structure is 62.2, 31.7 and 15.6 Å, respectively. None

of the fits obtained with MULTIFOXS was consistent with the largest distance of the woIF model, as the widest opening found in the case of WT-ADP/Mg was 54.8 Å for about half of the population, while the other half shows an opening of 29.5 Å (Figure S6). The other best fit for this condition gave similar values of opening of 51.5 and 29.5 Å in different proportions, 68 and 32%, respectively. All the other values for the opening between the TMD dropped to less than 42.2 Å. For WT-apo, 39.6 Å was the largest opening estimated for one conformation while the other one fluctuated between 39.3 Å (the most populated one in all fits) and 29.5 Å. Not surprisingly, WT-ATP/Mg/Vi leading to the trapping of ADP/Mg/Vi was the only condition where an OF conformation was found (distance of 15.2 Å) in a large proportion in the two fits (~ 80 %). Yet, a significant proportion of IF conformation appears to remain in this condition (distance of 36.6 Å), in agreement with the inability to properly fit the data with a unique OF conformation ($\chi^2 = 2.8$). This is presumably related to the regain in ATPase activity (~ 12%) reported above for the WT-ATP/Mg/Vi incubated sample after the SANS experiment. The K380A mutant in the apo state adopts different IF conformations similar to those seen in the WT BmrA regarding the opening of the TMD, but additional flexibility/reorientation of the NBDs with respect to the TMD could possibly occur as suggested by MULTIFOXS fitting (Figure 4**D**). This mutant appears unable to reach an OF conformation with a closed NBD state: in the presence of ATP/Mg ± Vi, it always remained in IF conformations with TMD separation varying between 39.3 and 31.6 Å.

HDX-MS supports the existence of multiple IF conformations for WT BmrA in the apo state. For an in-depth comparison of apo and ATP/Mg ± Vi bound states, HDX-MS was performed on WT and K380A mutant. Sequence coverages of ~ 70% were achieved allowing us to get precise information about local conformational changes occurring at the level of NBDs and ICDs during the catalytic cycle (Figure S7). WT-apo shows an overall high deuterium uptake especially in Walker A and B motifs, the D-loop, the C-terminus, and ICD1 and ICD2 (Figure 5**A**).

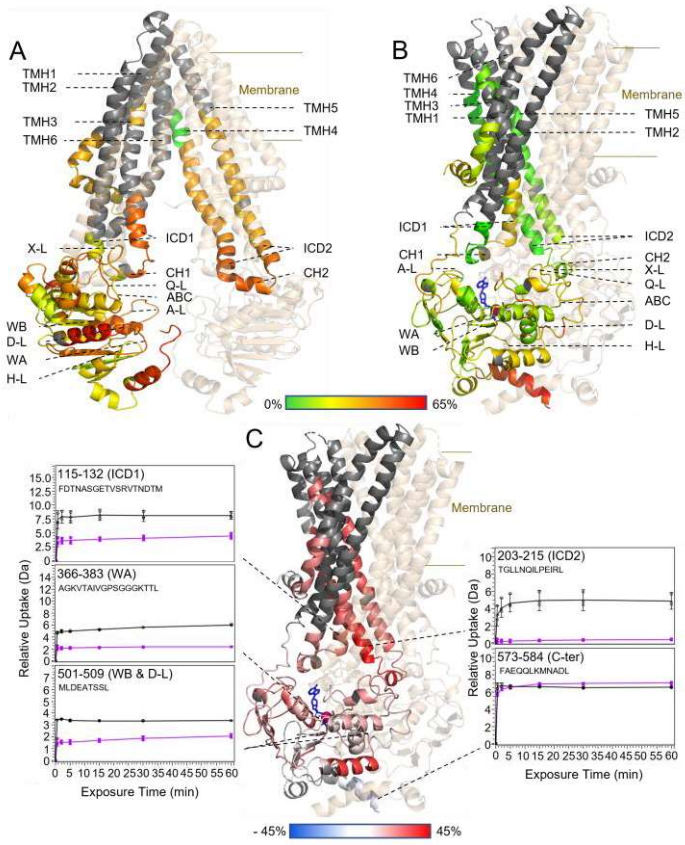

Figure 5. HDX-MS shows that WT BmrA is highly flexible in the apo state, as opposed to the vanadate-inhibited state. Deuterium exchange after 1-h of deuteration, plotted on **A**: apo form, the inward-facing model of BmrA (based on PDB 3WME) and **B**: ATP/Mg/Vi incubated form, the outward-facing structure (PDB 6R81). One monomer is colored according to a green (0%) to red (65%) scale. One ATP molecule is in blue, and Mg^{2+} in magenta. **C**: Differential deuterium uptake, between apo and ATP/Mg/Vi incubated forms, mapped on the OF structure, from -45% to 45% scale with blue: less deuteration, white: no difference, red: more deuteration uptake, in the apo form. In grey, peptides that were not identified. The box inserts show the relative deuterium uptake (Da) in apo (black) and ATP/Mg/Vi bound states (magenta) of selected peptides, with error bars showing the standard deviations between triplicates with sigma multiplier 2. A-L, Q-L, X-L, ABC, D-L and H-L, correspond to A-loop, Q-loop, X-loop, ABC motif, D-loop and H-loop, respectively; C-ter, C-terminal; CH, coupling helix; ICD, intracellular domain; TMH1-6, transmembrane helices 1-6; WA and WB Walker-A and -B motifs.

The only peptide that was completely shielded from exchange, even after 1 h of deuteration, lies in the transmembrane helix 4, presumably surrounded by the detergent belt. The high exchange observed in the ICDs, especially ICD2, implies a high flexibility of these subdomains in LMNG, which is congruent with the high deuterium exchange found in this region when BmrA was studied in a DDM solubilized form [33]. In addition, isotopic envelopes for most of the peptides from ICD2 are observed to be widespread and/or bimodal (e.g. peptide 180-215, Figure S8**A**), typical of EX1 regimes [50] whereby H-bond breathing events are much slower than the rate of proton/deuterium exchange and suggesting the presence of several co-existing conformations. In contrast, in the ATP/Mg/Vi-trapped state, WT BmrA shows a large overall protection against deuteration (Figure 5**B** & S7**A**), in agreement with the compact 3D-structure of the OF conformation. Only the solvent accessible and possibly unstructured C-terminal peptide exchanges very quickly with deuterium. Figure 5**C** shows peptides (in red) with higher

deuterium uptakes in the apo state compared to the WT-ATP/Mg/Vi state. Significant shielding is observed in all NBD conserved sequences involved in ATP/Mg binding, including Walker A- and B-motifs, the A-, C-, and D-loops (Figure S7**A**). The X- and the Q-loops, potentially involved in the NBD-TMD communication, are also protected. We observe a prominent decrease in deuteration of the ICDs, which connects the NBD and TMD, most likely linked to an increased structuration in the WT-ATP/Mg/Vi state. Globally, the large change in deuterium uptake between these two conditions confirms the major conformational change between the apo and ATP/Mg/Vi states. In addition, the presence of bimodal deuteration patterns in the apo state reveals the presence of co-existing conformations as also observed by SANS.

HDX-MS discloses the inability of the K380A mutant to reach the OF conformation. Given the lack of effect of vanadate with this mutant, only the effect of ATP/Mg was studied here. The overall high deuteration observed in the apo condition is comparable to that observed for the WT (Figure 6**A**).

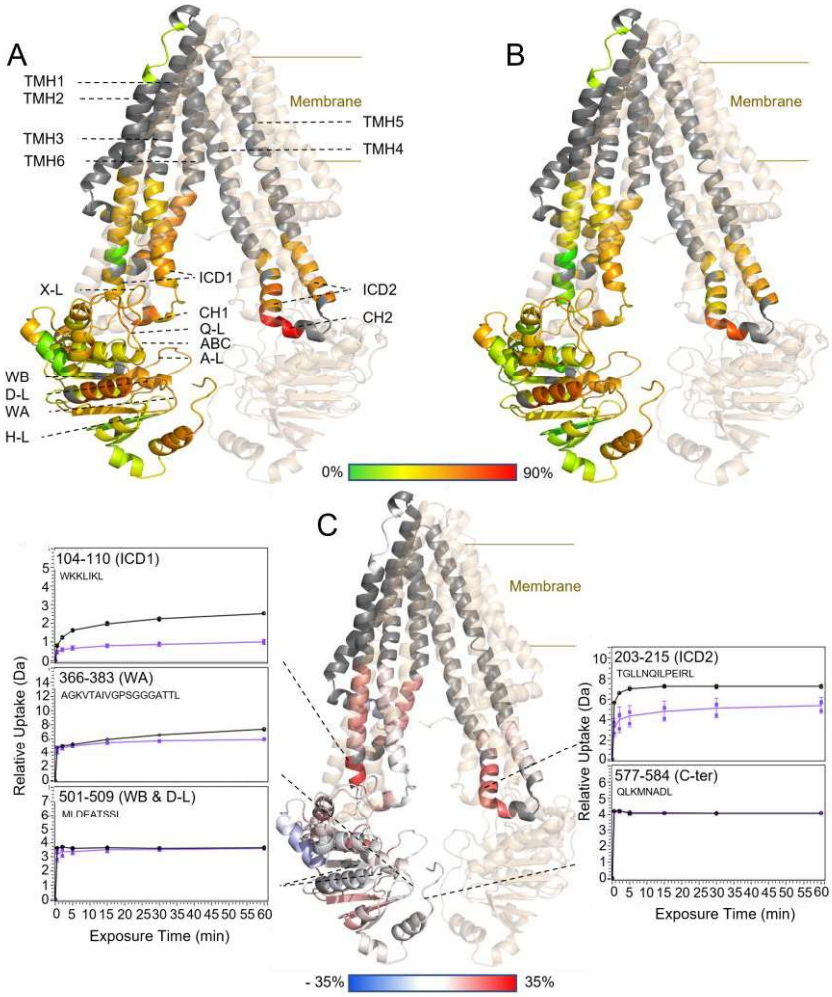

Figure 6. HDX-MS of K380A BmrA reveals its inability to reach an OF conformation in the presence of ATP. Deuterium exchange after 1 h of deuteration, plotted on the inward-facing model of BmrA (based on PDB 3WME) for **A**: apo form, and **B**: ATP/Mg bound form. One monomer is colored according to a green (0%) to red (90%) scale. **C**: Differential deuterium uptake, between apo and ATP/Mg bound forms, from -35% to 35% scale with blue: less deuteration, white: no difference, red: more deuteration, in the apo form. In grey, peptides that were not identified. The box inserts show, in Da, the relative deuterium uptake in apo (black) and ATP-bound forms (purple), of selected peptides, with error bars showing the standard deviations between triplicates with sigma multiplier 2. Abbreviations are the same as on Figure 5.

A striking difference is observed, however, for the ATP/Mg bound state. Here, a very limited protection against deuteration was detected for most peptides in the K380A mutant, ruling out the possibility of a large conformational change when the transporter binds ATP (Figures 6**B** & S7**B**). Interestingly, at shorter deuteration times, a limited but significant protection could be observed in conserved sequences involved in ATP/Mg binding, namely Walker A and B motifs, corroborating the binding of ATP by this mutant (Figure 6**C** box inserts and S7**B**). The most prominent effect afforded by ATP/Mg binding was seen at the level of ICDs, especially ICD2, where a clear reduced deuteration was observed (Figure 6**C**). This suggests that ATP binding to isolated NBDs in IF conformation stabilizes the structure of the ICDs

in the K380A mutant, while this mutation precludes the NBD dimerization and thereby the transition to the OF state.

Discussion

The power of SANS to highlight conformational changes has been illustrated with MsbA in nanodiscs where subtle differences between ADP and ADP/Vi conformations were reported [51]. This approach is, however, limited so far to nanodiscs formed exclusively from phosphatidylcholine as deuterated lipids need to be used to mask their contribution in scattering experiments [52]. For MsbA, this constraint did not seem to have any adverse effect as phosphatidylcholine allowed to regain a significant level of ATPase activity as compared to the detergent-purified transporter [51]. Yet, single molecule FRET showed that MsbA cannot readily switch between woIF and OF conformations in nanodiscs, in contrast to detergent or proteoliposomes states [26], suggesting that the former environment can somehow impede the overall motion of MsbA. Furthermore, a similar variation in distance between spin labels was shown by EPR spectroscopy for the transition of MsbA from IF to OF conformations both in detergent and in liposomes, indicating that the detergent state can be appropriate to study the ATPase cycle of some ABC transporters [53, 54]. For BmrA, the use of LMNG as a solubilizing agent maintains the transporter in a stable highly-active state (~ 1.4 μmol ATP hydrolyzed/min/mg) so this detergent appears suitable to recapitulate the ATPase cycle of BmrA [31, 32, 55].

SANS experiments reported here suggest that in the resting state BmrA has mostly two different IF conformations with, on average, a moderate opening between its two NBDs. This opening seems to be consistent with IF structures of P-gp (i.e. from mouse or *C. merolae*; Figure S9), whose global shape has been recently confirmed by EPR spectroscopy [56]. In contrast, BmrA does not seem capable to adopt a woIF conformation such as those found with MsbA (e.g. EcMsbA or StMsbA), although they are both homodimers with a significant degree of homology (30.9% of identity plus 26.6% of strong similarity between *S. typhimurium* MsbA and BmrA). P-gp is a full-length ABC transporter with two pseudo-symmetric halves connected by a linker of ~ 70 amino acids, and it has been suggested that this linker could restrain the physical separation of the NBDs [15]. BmrA is a homodimer, but the absence

of a linker between its two halves does not seem to allow a wide opening in the resting state. Thus, a more likely explanation for the different degree of opening between the two moieties of ABC exporters possibly lies in the nature of the molecule transported [10]. MsbA is involved in the translocation of a large lipopolysaccharide, and because this molecule is entirely accommodated into a wide cavity within the transporter [57, 58], this might support the physiological relevance of a woIF conformation of MsbA to accommodate such a big substrate [16-18]. P-gp or BmrA, on the other hand, are dedicated to the efflux of toxic compounds whose size appears limited, i.e. < 1200 Da for most P-gp substrates [59]. Larger molecules such as the a-factor pheromone (~ 1600 Da) do not necessarily bind entirely within the P-gp cavity in order to be exported. The IF conformation found in P-gp is nevertheless capable to create a large internal cavity of ~ 6000 $Å^3$ [60, 61], that can potentially accommodate two drugs simultaneously [62-64], presumably due to an inherent flexibility in the apo state [20, 65].

The best fits of our SANS data show an intrinsic flexibility of BmrA in the resting state with possibly two main IF conformations. It should be noted that the SANS models were not subjected to energy minimization; they were mainly used to enlighten the overall conformation of the transporter in a given state, and in particular the distances between the two NBDs. The SANS data might as well be the result of a continuum of several discrete IF conformations but the fitting process would have been much more arduous to achieve, so we limited ourselves to two different conformations. Intrinsic flexibility in the resting state has also been observed for the homologous multidrug transporter LmrA by EPR spectroscopy [66]. In BmrA, this flexibility involves presumably some disengagement and/or rotation of the NBDs relative to the ICDs that might even be exacerbated in the K380A mutant. Considering the rigid body transition from IF to OF states that was anticipated from different 3D structures [17], these SANS results might seem at odds but they are actually supported by our HDX-MS data: a much higher accessibility of the ICDs to deuterium exchange is observed in the resting state as compared to the OF conformation stabilized by ADP/Mg/Vi. This is also congruent with our previous HDX-MS study using a catalytically inactive E504A mutant trapped in an ATP-bound state where its ICDs were quite protected from deuterium exchange in comparison to the WT BmrA in the apo state [33]. Such a protection from deuterium exchange was also reported with P-gp in the ATP-bound state [65]. Interestingly, a disengagement of NBD1 from ICD4 has been proposed to occur in the resting state

of CFTR to explain the nanobody accessibility of an epitope, which would be otherwise buried in the whole transporter if a static 3D structure was maintained throughout the catalytic cycle [67].

The results obtained with the K380A BmrA mutant underline its inability to reach the OF conformation upon ATP binding (Figure 7), as previously hypothesized from a low-resolution cryo-EM study of BmrA in unique ring structures [35].

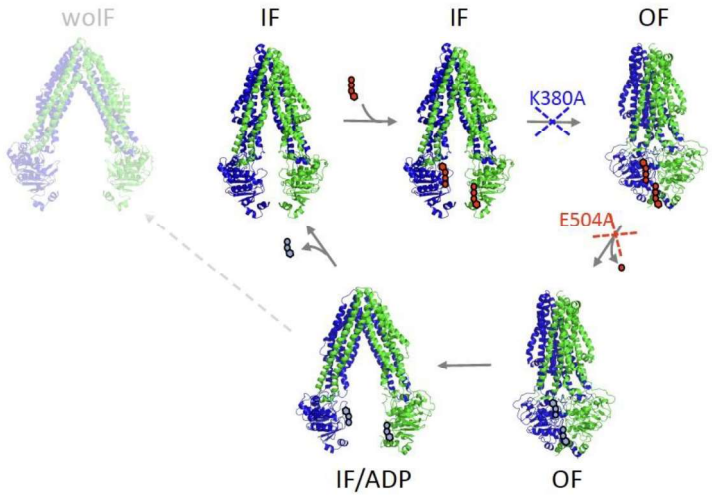

Figure 7. Scheme of the catalytic cycle of WT BmrA and the steps impaired by the two mutations. In the apo state, WT BmrA mainly adopts an IF conformation where the two NBDs are physically separated but the woIF is not, or marginally, populated by BmrA (dotted line for the ghost of the woIF conformation). Binding of ATP (hexagon tethered to three red circles) triggers the dimerization of the NBDs. In this OF conformation, ATPase activity will lead to Pi dissociation (red circle) that will return the transporter to an IF conformation. Based on the SANS results, this conformation (IF/ADP) is on average more open that the apo state. ADP (hexagon tethered to two light blue circles) dissociation resets BmrA in the apo state with a shortened distance between the NBDs. The steps impaired in the K380A and E504Q mutants are indicated on the scheme.

A similar conclusion was drawn from mutations of the equivalent lysine residues in the two NBDs of the P-gp [68] or, more recently, from a mutant in the A-loop of the first NBD of this transporter [69]. Also, a lack of ATP-dependent dimerization of the NBD of ComA was reported in the Walker-A K to A mutant [70]. ATP binding induces, however, a global effect on the conformation of the K380A mutant as revealed by limited proteolysis, thermal denaturation and SANS data. The major effect of ATP binding to this mutant observed by HDX-MS is the structuration of ICDs, and in particular ICD2, presumably mediated by its interaction with the NBD. At the NBD level, changes in local dynamics are visible but no drastic effect is seen on the deuteration rate for a large number of peptides, suggesting that the global conformation of the NBD is unchanged between the apo and ATP-bound states. This is consistent with the 3D structures of ABCB10 [71] or ABCB8 [72] in which the binding of an ATP analog to each NBD did not promote the NBD dimerization, so the transporters remained in an open IF

state; in these 3D structures, the global conformation of the NBD is essentially unaffected by nucleotide binding. This likely explains the weak direct protection observed for the NBD peptides in our HDX-MS experiment with the K380A mutant. Indeed, HDX-MS monitors the exchange of deuterium at the level of the backbone amide hydrogen [40] while nucleotide binding to single NBD involves essentially side-chain residues, except for the Walker-A motif [73]. A comparison of the access to the hydrogen atoms of the amide backbone of ABCB10 with and without nucleotide analog shows that the presence of the nucleotide does not induce any difference, even for the Walker-A motif (Table S3), thereby possibly explaining the lack of strong protection in HDX-MS with the K380A mutant.

Finally, a rather astounding result came from the SANS data suggesting that, on average, BmrA in the presence of ADP/Mg adopts a conformation significantly more open than in the resting state. This suggests that in this post-hydrolytic step, the ADP-Mg end-product induces some repulsion between the two NBDs, as originally proposed [74], but with a larger degree of opening than when the ATP-binding sites are empty. First, it is important to mention that this ADP-bound state is presumably identical to that obtained during the whole ATPase cycle because the same 3D structures were obtained for MalK subunits starting either from ATP/Mg (ending up with two ADP/Mg in the two catalytic sites) or by adding ADP/Mg in the crystallization medium [73]. MD simulations suggest that in contrast to ATP, ADP may lead to the destabilization of the NBD dimer [75, 76], supporting the fact that the OF state was not observed by Cryo-EM for P-gp in the presence of ADP [21]. MsbA, on the contrary, seems capable to reach the OF state to some extent, in the presence of ADP/Mg [15], and it is important to mention that the Sav1866 3D structure was solved in an OF conformation with bound ADP/Mg [77]. Interestingly, two 3D structures of MalK were solved in the resting state, open and semi-open, with different inter-subunit separations [78], while the ADP/Mg-bound structure falls in between these two forms [73]. Here, our results support the contention that BmrA in the apo state remains mostly in two main IF conformations with a moderate opening between its NBDs, whereas ADP/Mg may increase the inter-NBD separation (Figure 7, IF vs IF/ADP). This is also corroborated by a cryo-EM study on human P-gp showing that in the resting state, the transporter fluctuates between IF and OF conformations while addition of ADP keeps the transporter in IF conformations [21]. Because this latter study was performed in the presence of a specific monoclonal antibody, it might have affected the equilibrium between the

IF and OF conformation, and a strong preference for an IF conformation was reported by thermal unfolding of the mouse P-gp in the apo state [79]. Here, our results with BmrA were obtained with the native protein so they clearly support a wider opening of the two NBDs in the post-hydrolytic state as compared to the resting state. This property might be a common trend of symmetrical ABC exporters that has a major implication for their catalytic mechanism. Indeed, the post-hydrolytic ADP-bound state is a required step that precedes the release of ADP from the NBDs, and the subsequent binding of two ATP to engage in a next transport cycle. Because BmrA and the P-gp are in an IF conformation with the two NBDs physically separated in this ADP-bound state, this conformation is therefore relevant for their functioning mechanism. Moreover, it has been argued that the ATP concentration in the cells is far in excess of the K_M value for P-gp, so this transporter will always be saturated by ATP. This is clearly not the case for many micro-organisms which constantly have to face adverse conditions and the ATP concentration might become quite low [80]. In such instances, the IF open state will be physiologically relevant. In fact, the lifetime of this open IF conformation will be primarily dictated by the rate of release of ADP from the NBDs and the subsequent rate of ATP binding.

In conclusion, by using a combination of SANS and HDX-MS, our results uncover the main steps of the catalytic cycle of a homodimeric multidrug ABC transporter and highlight the importance of the ADP-bound IF conformation adopted during the post-hydrolytic step of a transporter from the type IV subfamily.

Acknowledgments

This work was supported by the Agence Nationale de la Recherche (ANR), grants ANR-14-CE09-0024B (JMJ), ANR-19-CE11-0023-01 (CO), and ANR-16-CE92-0001 (CE and CB). It was partially supported by the IDEX-IRS project Pepsi-SAS “Small-angle scattering using polynomial expansions” funded by Univ. Grenoble Alpes. We thank Sergei Grudinin (INRIA Grenoble FR) and Dina Schneidman-Duhovny (Weizmann Institute, Rehovot, IL) for computing support, and Luca Signor (IBS Grenoble FR) who performed the MALDI-TOF-MS analysis. This work used the platforms of the Grenoble Instruct-ERIC center (ISBG; UMS 3518 CNRS-CEA-UGA-EMBL) within the Grenoble

Partnership for Structural Biology (PSB), supported by FRISBI (ANR-10-INBS-05-02) and GRAL, financed within the University Grenoble Alpes graduate school (Ecoles Universitaires de Recherche) CBH-EUR-GS (ANR-17-EURE-0003). IBS acknowledges integration into the Interdisciplinary Research Institute of Grenoble (IRIG, CEA). Waqas Javed benefitted from a doctoral fellowship by the Higher Education Commission of Pakistan as well as a grant from ILL for his fourth year of PhD. This work benefited from the use of the SasView application, originally developed under NSF award DMR-0520547. SasView contains code developed with funding from the European Union's Horizon 2020 research and innovation program under the SINE2020 project, grant agreement No 654000. HDX-MS were supported by the French Ministry of Research (Investissements d'Avenir Program, Proteomics French Infrastructure, ANR-10-INBS-08 to O. B-S) and the Région Midi-Pyrénées (O. B-S). We also thank Dr. Khadija Mathieu for her input in BmrA model based on 3WME made using MODELLER.

Author Contributions

Conceptualization, C.O., C.B., C.E., A.M and. J.-M.J.; Investigation, W.J, C.O., S.V., M.-P.C., A.L.R., M.M., M.H., C.B., J.M., C.E., and A.M.; Original Draft of the MS, J.-M.J. with input from W.J, C.E., and A.M.; Review & Editing, W.J., C.O., J.M., C.E., A.M and J.-M.J.; Supervision, C.O., M.H., J.M., C.E., J.-M.J., and A.M.; Funding Acquisition, O. B-S, C.O., C.E., C.B., A.M. and J.-M.J.

Declaration of Interests

The authors declare no competing interests.

ORCID: Cécile Breyton : 0000-0002-4382-0434 ; Christine EBEL : 0000-0002-6912-500X; Julien Marcoux: 0000-0001-7321-7436; Cédric Orelle: 0000-0003-3418-3290; Anne Martel : 0000-0002-1232-8519; Waqas Javed: 0000-0002-3381-4794; Jean-Michel Jault : 0000-0003-1743-2777

Figure Titles and Legends only

Figure 1. Thermal stability of WT BmrA and mutants and effect of nucleotides. Ratio of fluorescence emitted at 350 and 330 nm and first-derivatives with T_m (upper and lower sub-panels, respectively) for **A**: WT, wild-type BmrA. **B**: E504Q mutant and **C**: K380A mutant. Unless otherwise specified, ADP or ATP were added at 10 mM in the presence of 10 mM $MgCl_2$; When 2 mM ATP was used, 3 mM $MgCl_2$ were added; Vi was added at 1 mM. These experiments were reproduced at least three times from two different batches of purified proteins and with triplicate each time; a representative experiment is shown here.

Figure 2. Limited proteolysis of K380A and E504Q mutants compared to WT BmrA. After incubation with the indicated ligands, BmrA WT (**A**-**B**), E504Q (**C**-**E**), or K380A mutants (**F**-**I**) were treated with trypsin for various times. $MgCl_2$ was added at 3 or 10 mM when 2 or 10 mM nucleotides were used, respectively. Vi was added at 1 mM. All samples were in 0.01% LMNG. Time zero was taken just before adding trypsin and the proteins were resolved using a 12% SDS PAGE. The arrows indicate the position of intact BmrA. Red boxes highlight the bands after 60 min of digestion. These experiments were reproduced at least three times from at least two different batches of purified proteins and a representative experiment is shown here.

Figure 3. SANS data analysis. A: SANS scattering curves of WT BmrA in the apo state (green), or in the presence of ADP/Mg (yellow) and ATP/Mg/Vi (red), of the E504Q mutant in the apo state (blue) or in the presence of ATP/Mg (cyan), of the K380A mutant in the apo state (purple) or in the presence of ATP/Mg/Vi (pink). **B**: Example of Guinier fit for WT BmrA in the apo state. **C**: Pair distance distribution functions (p(r)) with the same color code as **A**. Note the p(r) are not normalized, the integral depends on sample concentration. Theoretical p(r) based on the PDB 6R81 structure of BmrA (continuous line, a), and on BmrA models built on PDB 3WME (dotted line, b) and 3B5W (discontinuous line, c) at 1 mg/mL. P(r) of BmrA homolog structures are given in Figure S1 for comparison. The error bars on the scattering data represent the uncertainty of each pixel (= sqrt counts / counts) propagated through the radial averaging.

Figure 4. Multi-conformation fits of SANS data using Multifoxs. Each graph shows the best fit of SANS data with two conformations of WT-apo (**A**), WT-ADP/Mg (**B**), WT-ATP/Mg/Vi (**C**), K380A-apo (**D**) and K380A-ATP/Mg/Vi (**E**), together with the two modelled conformations combined to obtain the fit, and their relative proportion. Other conformation pairs fitting equally well the data are presented in figure S6. After the fitting process, the His-tag has been removed from the picture for clarity. On each fit, the grey dash lines show, for each Q-value, the minimum and maximum intensities from the calculated curves of the 7006 possible conformations.

Figure 5. HDX-MS shows that WT BmrA is highly flexible in the apo state, as opposed to the vanadate-inhibited state. Deuterium exchange after 1-h of deuteration, plotted on **A**: apo form, the inward-facing model of BmrA (based on PDB 3WME) and **B**: ATP/Mg/Vi incubated form, the outward-facing structure (PDB 6R81). One monomer is colored according to a green (0%) to red (65%) scale. One ATP molecule is in blue, and Mg^{2+} in magenta. **C**: Differential deuterium uptake, between apo and ATP/Mg/Vi incubated forms, mapped on the OF structure, from -45% to 45% scale with blue: less deuteration, white: no difference, red: more deuteration uptake, in the apo form. In grey, peptides that were not identified. The box inserts show the relative deuterium uptake (Da) in apo (black) and ATP/Mg/Vi bound states (magenta) of selected peptides, with error bars showing the standard deviations between triplicates with sigma multiplier 2. A-L, Q-L, X-L, ABC, D-L and H-L, correspond to A-loop, Q-loop, X-loop, ABC motif, D-loop and H-loop, respectively; C-ter, C-terminal; CH, coupling helix; ICD, intracellular domain; TMH1-6, transmembrane helices 1-6; WA and WB Walker-A and -B motifs.

Figure 6. HDX-MS of K380A BmrA reveals its inability to reach an OF conformation in the presence of ATP. Deuterium exchange after 1 h of deuteration, plotted on the inward-facing model of BmrA (based on PDB 3WME) for **A**: apo form, and **B**: ATP/Mg bound form. One monomer is colored according to a green (0%) to red (90%) scale. **C**: Differential deuterium uptake, between apo and ATP/Mg bound forms, from -35% to 35% scale with blue: less deuteration, white: no difference, red: more deuteration, in the apo form. In grey, peptides that were not identified. The box inserts show, in Da, the relative deuterium uptake in apo (black) and ATP-bound forms (purple), of selected peptides,

with error bars showing the standard deviations between triplicates with sigma multiplier 2. Abbreviations are the same as on Figure 5.

Figure 7. Scheme of the catalytic cycle of WT BmrA and the steps impaired by the two mutations. In the apo state, WT BmrA mainly adopts an IF conformation where the two NBDs are physically separated but the woIF is not, or very marginally, populated by BmrA (dotted line for the ghost of the woIF conformation). Binding of ATP (hexagon tethered to three red circles) triggers the dimerization of the NBDs. In this OF conformation, ATPase activity will lead to Pi dissociation (red circle) that will return the transporter to an IF conformation. Based on the SANS results, this conformation (IF/ADP) is on average more open that the apo state. ADP (hexagon tethered to two light blue circles) dissociation resets BmrA in the apo state with a shortened distance between the NBDs. The steps impaired in the K380A and E504Q mutants are indicated on the scheme.

Tables with Titles and Legends

BmrA proteins	WT			E504Q		K380A	
conditions	Apo	ADP/Mg	ATP/Mg/Vi	Apo	ATP/Mg	Apo	ATP/Mg/Vi
Rg (Å)	44.3 ± 0.2	43.8 ± 0.3	40.3 ± 0.3	45.0 ± 0.3	42.5 ± 0.4	45.5 ± 0.5	44.3 ± 0.4
Max in p(r) (Å)	(41); 53	53	38	(40); 53	41	50	41; (59)

Table 1. Guinier and pair distribution analysis of BmrA samples in SANS. The precision for the p(r) maxima is ~ 2 Å. Values in parenthesis for the p(r) maxima indicate the position of shoulders.

MATERIELS AND METHODS

RESOURCE AVAILABILITY

Lead Contact *:*further information and requests for resources and reagents should be directed to and will be fulfilled by the Lead Contact, Jean-Michel Jault (jean-michel.jault@ibcp.fr).

Data and Code Availability Statement*:* The [datasets/code] generated during this study are available at [name of repository] [accession code/web link].

- SANS Data: doi.ill.fr/10.5291/ILL-DATA.BAG-8-36; doi.ill.fr/10.5291/ILL-DATA.BAG-8-37. SANS curves for the analyzed samples are provided in Table S2.
- The HDX-MS data has been deposited to the ProteomeXchange Consortium via the PRIDE partner repository [81] with the dataset identifier PXD028663.
- The quality control data for AUC, SEC-LS, and MALDI-TOF, have not been deposited in a public repository but are available from the corresponding author on request.

METHOD DETAILS

BmrA sample names: WT-Apo: WT without ligand; WT-ADP/Mg: WT + 10 mM ADP + 10 mM $MgCl_2$; WT-ATP/Mg/Vi: WT + 10 mM ATP + 10 mM $MgCl_2$ + 1 mM Vi; E504Q-Apo: E504Q without ligand; E504Q-ATP/Mg: E504Q + 10 mM ATP + 10 mM $MgCl_2$; K380A-Apo: K380A without ligand; K380A-ATP/Mg/Vi: K380A + 10 mM ATP + 10 mM $MgCl_2$ + 1 mM Vi.

Buffers: Buffer A : 50 mM Tris-HCl pH 8, 10% glycerol, 100 mM NaCl, 20 mM imidazole and 0.01% LMNG. Dialysis buffer : 50 mM Hepes-KOH pH 8, 10% glycerol, 50 mM NaCl and 0.01 % LMNG. SANS buffer: 50 mM Tris-HCl pH 8, 150 mM NaCl, 10% Glycerol, 0.01% LMNG and 21.4% D_2O.

Cloning and expression of deuterated BmrA : the plamids for hydrogenated BmrA expression are: *pET23-WT bmrA* [29]; *pET23-E504Q bmrA* [39]; *pET23-K380A bmrA* [35]. For the production of deuterated BmrA requiring kanamycin resistance, the following constructs were designed. Construction of *pET28-WT bmrA*: *bmrA* gene fragment was PCR-amplified from *pET23-WT bmrA* with the primers

TataccatggcaCCAACCAAGAAACAAAAATCTAAAAGTAAATTGAA and *CTTGTCGACCCCGGCTTT*. *WT bmrA* was cloned in *pET28* by using the NcoI and SalI restriction sites. Construction of *pET28-E504Q bmrA*: The plasmid *pET28-bmrA* was digested with SalI and PstI for 3 hours at 37 °C. After electrophoresis, the 6436 bp fragment was extracted from the agarose gel. The plasmid *pET23-E504Q bmrA* was similarly digested with SalI and PstI and the 587 bp fragment was extracted. Next, a ligation with the two fragments was performed with T4 DNA ligase for 4 h at room temperature, before transformation of TOP10 cells. Construction of *pET28-K380A bmrA*: The plasmids *pET23-K380A bmrA* and *pET28-WT bmrA* were digested with StuI and SacII restriction enzymes for 1 h at 37 °C. After electrophoresis, the smaller fragment corresponding to *K380A bmrA* from *pET23* and the bigger fragment lacking *WT bmrA* from *pET28* were extracted from the agarose gel. Next, a ligation with the two fragments was performed with T4 DNA ligase for 1 h at room temperature, before transformation of TOP10 cells. The amino acid sequences of BmrA in *pET28* are given in Table S2.

Preparation of deuterated BmrA bacterial paste: expression of partially deuterated ("match-out labeled") BmrA (d-BmrA) for neutron scattering was carried out by the ILL Deuteration Laboratory (D-Lab) at the Institut Laue-Langevin (ILL), Grenoble, France, according to previously established protocols [82, 83]. After adaptation to growth in deuterated minimal medium, C41(DE3) cells containing the expression vector *pET28a* with the coding sequence for wild-type or mutant BmrA (K380A or E504Q) inserted, were grown in a high-cell density fermenter culture at 30 °C. The deuterated minimal medium contained 85% (v/v) D_2O and unlabeled glycerol as carbon source. During the batch and fed-batch phases, the pD was adjusted to 6.9 by addition of NaOD (Eurisotop, France). The culture was induced with 0.5 mM IPTG at an OD_{600} of around 13 and deuterated cells (about 50 g wet weight from 1-2 L of fermenter culture) were harvested after overnight expression and stored at -80 °C.

Inverted Membrane Vesicles (IMVs) preparation: the preparation of IMVs for the hydrogenated proteins was typically done as detailed in [31]. Briefly, bacterial pellet was resuspended, cellular debris was removed by centrifugation after cell lysis, membrane fraction was obtained by ultracentrifugation, twice, and resuspended in 20 mM Tris-HCl pH 8, 300 mM sucrose, 1 mM EDTA; membranes were stored at -80 °C. The total protein concentration in membrane vesicles was analyzed by BCA assay. For

deuterated pellets, the differences were as follows: bacterial pellet was resuspended with, additionally, 1 mg/mL lysozyme; the bacterial cells were lysed by three 5 min cycles of sonication; membrane fraction was obtained by one ultracentrifugation only.

BmrA purification: BmrA enriched IMVs, at 2 mg/mL final membrane protein concentration, were solubilized for 1 h at 4 °C in 50 mM Tris-HCl pH 8, 10% glycerol, 100 mM NaCl, 1 mM dithiotreitol, 10 mM imidazole, protease inhibitor cocktail tablet (Roche) and 1% LMNG. The soluble fraction obtained after ultra-centrifugation, at 150,000 g for 1 h at 4 °C, was injected into a 1 mL HisTrap HP column (GE Healthcare), which was pre-equilibrated with buffer A. The column was washed first with 3-5 column volumes of 50 mM Tris-HCl pH 8, 10% glycerol, 500 mM NaCl, and 0.01% LMNG, and then with 20 column volumes of the buffer A. Gradient elution was then performed with the imidazole gradient from 20 to 500 mM. The protein fractions were dialyzed twice, overnight, and for 4 h the next day, at 4 °C against dialysis buffer. The protein concentration was determined from UV absorbance at 280 nm by using Nanodrop spectrophotometer, and a $\varepsilon 280nm=38,850\ M^{-1}\ cm^{-1}$. The protein concentration was further assayed with Bradford method. Protein was stored at -80 °C after flash freezing in liquid N_2.

Deuterated BmrA purification and SANS samples: SANS measurements were performed in two sessions, corresponding to two slightly different purification protocols. The initial steps of the two purifications were essentially as above, with the following modifications. The solubilization was done for 1.5 h at 4 °C in 100 mM sodium phosphate (Na-Pi) pH 8 (session 1) or 100 mM Tris-HCl pH 8 (session 2), 15% glycerol, 100 mM NaCl, 1 mM dithiotreitol, 10 mM imidazole and 1% LMNG. The 1 mL HisTrap HP column was pre-equilibrated with 50 mM Na-Pi pH 8 (session 1) or 50 mM Tris-HCl pH 8 (session 2), 15% glycerol, 100 mM NaCl, 20 mM imidazole and 0.01% LMNG. The column was washed with 20 column volumes of the same buffer before the imidazole gradient. Then, the most concentrated fractions were pooled, and dialysed overnight at 4 °C against either 50 mM Hepes pH 8 (session 1) or 50 mM Tris-HCl pH 8 (session 2), 10% glycerol, 50 mM NaCl, 0.01% LMNG, before flash freezing in liquid N_2. Next, protein was concentrated using 4 mL 100 kDa cutoff Millipore concentrator, and injected into a Superdex 200 10/300 GL SEC column equilibrated with SANS buffer,

at a flow rate of 0.25 mL/min. The most concentrated fractions were pooled, concentrated, and re-injected into the same column. The final samples were obtained by pooling the most concentrated fractions. They were, with or without ligands, filled in 1 mm quartz cuvette for SANS measurements. In session 2, where indicated, the ligands were added in the cuvette after acquisition of the data for the Apo form. The BmrA samples measured were, in session 1: WT-Apo (A_{280} = 1.64); WT-ADP (A_{280} = 1.59); WT-ATP/Vi (A_{280} = 1.55); E504Q-Apo (A_{280} = 1.395); E504Q-ATP (A_{280} = 1.35); and in session 2: WT-Apo (A_{280} = 0.55); WT-ATP/Vi (A_{280} = 0.54, and A_{280} = 1.21); K380A-Apo (A_{280} = 0.23, and A_{280} = 0.91); K380A-ATP (A_{280} = 0.22); K380A-ATP/Vi (A_{280} = 0.91).

ATPase activity assay: the activity assays of BmrA were done in a quartz cuvette in a final volume of 700 µL. The buffer, containing 50 mM Hepes-KOH pH 8, 10 mM $MgCl_2$, 4 mM phosphoenolpyruvate, 0.3 mM NADH, 32 µg/mL lactate dehydrogenase, 60 µg/mL pyruvate kinase, 10 mM ATP and 0.01% LMNG, was added into the cuvette and was allowed to attain the desired temperature, i.e. 37 °C for 5 min, before adding 3 µg protein (estimated from Bradford assays), and measuring the absorbance at 340 nm for 20 min at 37 °C.

MALDI TOF Mass spectrometry quality control: the experiments were done using an Autoflex Max mass spectrometer (Bruker Daltonics), after diluting the WT and E504Q BmrA SANS samples to typically 2.5 µM with sinapinic acid matrix (Sigma; 10 mg/ml in acetonitrile/water, 0.1% TFA (50:50)), and depositing 1 µL on the target. In the case of K380A, the sample was diluted 6 times in 5% formic acid, and analyzed according to [84]. From the measured masses of 68998, 69072, and 68830 Da, for WT, E504Q, and K380A BmrA, a deuteration level of 70, 72, and 67% was obtained, respectively, for the non-labile hydrogens (Table S1).

Limited proteolysis of BmrA: purified BmrA was diluted to 0.5 µg/µL in the dialysis buffer. After 15 min of incubation at room temperature, in the presence or abesnce of ligands as indicated below, trypsin (1 µg/25 µg of protein) was added. Samples of 10 µL (5 µg BmrA) were withdrawn at 0, 2, 5, 15, 30, 60, 120, 180 and 240 min. 2.5 µL of 5% trifluoroacetic acid was added immediately to each sample to stop the reaction. 3.2 µL of Laemmli (5x) was then added and the samples were placed in ice before

resolving them by 12% SDS-PAGE. When indicated, the buffer was supplemented with ATP or ADP, $MgCl_2$ and Vi.

Thermal unfolding: thermal denaturation and aggregation analysis were done by differential scanning fluorimetry using the Prometheus NT.48 instrument and analyzed using the PR.thermocontrol V2.0.4. software (Nanotemper technologies, DE). The ratio of fluorescence intensity at 350 nm/330 nm was used to determine the melting temperatures, T_m. All BmrA samples were at 2-3 mg/mL in dialysis buffer and supplemented with ATP and/or ADP, $MgCl_2$, Vi, where specified. Samples were incubated for 15 min at room temperature after the addition of ligands before analysis. T_m of deuterated WT and E504Q BmrA were measured after SANS and AUC, after three-time dilution in the SANS buffer.

Analytical Ultracentrifugation Sedimentation Velocity (AUC-SV): AUC-SV experiments were conducted in an XLI analytical ultracentrifuge (Beckman, Palo Alto, CA) using an ANTi-50 rotor, employing double channel Ti centre pieces of 3 mm optical path length equipped with sapphire windows (Nanolytics, Potsdam, Germany). Samples from the first SANS session were frozen and unfrozen before AUC-SV. The reference channel was filled with solvent without detergent. Acquisition was done at 20 °C and at 42,000 rpm (130,000 g), overnight, using 278 nm absorbance, and interference detection. Data processing and analysis were done using the programs REDATE v0.2.1 [85]. SEDFIT V 15.01b [86] from P. Schuck (NIH, Besthesda, USA), and GUSSI v1.1.0 [87] from C. Brautigam (Univ of Texas South Western, Dallas, USA), and using standard equations described in [45, 88]. Corrected s-values, s_{20w}, were calculated according to [88] considering 1 g/g of bound detergent, and taking into account d-BmrA and LMNG deuteration in 21.4% D_2O.

Size Exclusion Chromatography coupled to Light Scattering (SEC-LS): SEC-LS experiments were conducted at 4 °C on an HPLC consisting of a degasser DGU-20AD, a LC-20AD pump, an autosampler SIL20-ACHT, a communication interface CBM-20A and a UV–vis detector SPD-M20A (Shimadzu, Kyoto, Japan), a column oven XL-Therm (WynSep, Sainte Foy d'Aigrefeuille, France), a static light scattering miniDawn Treos, a dynamic light scattering DynaPro NANOSTAR, and a refractive index Optilab rEX detectors (Wyatt, Santa-Barbara, USA). The analysis was made with the software ASTRA, v5.4.3.20 (Wyatt, Santa-Barbara, USA), using standard methods. The samples of SANS second session

were stored at 4 °C 20-40 h before injection onto SEC-LS. 100, 25, and 100 µL of WT-ATP-Vi (A_{280} =0.54), K380A-Apo (A_{280} = 0.94), and K380-ATP (A_{280} =0.22), respectively, were injected at 0.5 mL min^{-1} on a Superdex 200 10/300 GL (GE Healthcare, Chicago, USA). Samples were in the SANS buffer; the elution buffer was the same but hydrogenated. Bovine serum albumin at 2 mg mL^{-1} in PBS buffer was injected as a control.

Numerical values for AUC, SEC-LS, and SANS analysis: a solvent density of 1.0594 g mL^{-1} and viscosity of 1.531 cp were measured for the SANS buffer at 20 °C using a density-meter DMA 5000 and a viscosity-meter AMVn (Anton PAAR, Graz, Austria). For BmrA, the partial specific volume, $\bar{v}$ = 0.751 mL g^{-1}, and refractive index increment, $\partial n/\partial c$ = 0.185 mL g^{-1}, were calculated from the amino-acid sequence using the program SEDFIT. The extinction coefficient of 0.586 mL mg^{-1} cm^{-1} at 280 nm is known to be only indicative. The 2-component analysis in SEC-LS provided the expected molar mass for the protein-detergent complex (see results part), but false protein molar mass (170 kDa), a point previously noticed for BmrA [45] or for the PatA/PatB multidrug transporter [89] and attributed to an erroneous value of the extinction coefficient calculated from sequence. Molecular weights in solution estimated by combining the forward intensity extracted from the Guinier plots, BmrA concentration, and scattering length density knowledge, consistent for a given protein, are larger by 10% to 50% than the theoretical value for the dimer, which we believe is related to the method used to determine protein concentrations (Table S2). For LMNG: $\bar{v}$ = 0.797 mL g^{-1}, and $\partial n/\partial c$ = 0.146 mL g^{-1} [32]. Ratio, M_D/M_H, of the mass of the molecule in 21.4 % D_2O: 1.044 and 1.045, for the 70% and 72% d- WT and d- E504Q BmrA, respectively, considering 80% of the exchangeable H exchanged in 100% D_2O, and 1.003 for LMNG, was calculated from the chemical structures and used to derive $s_{20,w}$. Numerical values for SANS are given in Table S2.

BmrA structural models for SANS analysis: two homology models were built by SWISS-MODEL [90] using crystal structures of two ABC transporters with PDB codes: 3WME and 3B5W. The histidine tag, ab-initio folded using QUARK online [91] was added to these two models, and to the OF cryo-EM structure of E504A BmrA with a PDB code 6R81.

SANS data recording: SANS curves have been recorded on D22 instrument, at Institut Laue Langevin, using a neutron wavelength $\lambda = 6$ Å ± 10% in two configurations (collimation length: sample-detector distance): (2.8 m: 1.4 m) or (2.8 m: 1.6 m), and (8 m: 8 m), which together enabled to obtain a q-range from 0.007 $Å^{-1}$ to 0.5 $Å^{-1}$. The samples were placed in 1 mm thick suprasil quartz cuvettes (Hellma, Müllheim, Germany), in a 22-position rack thermostated at 20 or 7 °C. The exposure time varied between 15 and 20 min at short detector distance and 30 to 90 min at long distance. The beam measures 40 mm x 55 mm upstream collimation and 7 mm x 10 mm at sample position. Full details are given in Table S2 according to the published guidelines [92].

SANS data reduction : data were scaled to absolute intensity I (q) in absolute scale (cm^{-1}) *vs*. q (where $q = 4\pi\sin\theta/\lambda$, 2q is the scattering angle, λ is the neutron wavelength) as follows. The neutron flux at sample position was used to calibrate scattering intensity to absolute scale. The empty beam transmission was used to set the center of the patterns and to calculate the transmission of the empty cell, the buffers, and the samples. The scattering of the piece of boron-enriched material, absorbing the totality of the beam flux, was subtracted from all other patterns because it results from ambient and electronic noise. The raw data were reduced (detector efficiency, electronic and empty cell background subtraction, angular averaging, transmission, and thickness correction) using GRASP software package developed by C. Dewhurst (https://www.ill.eu/users/support-labs-infrastructure/software-scientific-tools/grasp). The scattering curves measured at the two different configurations and covering different but overlapping q ranges were merged after respective buffer subtraction using SANS reduction macros written by S. Kline for IGOR software [93]. Using the ATSAS suite of software [94] , the resolution column and data at $q > 0.25$ $Å^{-1}$ were removed, and the q-values were expressed in nm^{-1}. For each duplicated samples with the same construct and condition, and for K380A-ATP when compared to K380A-ATP/Vi, after normalization by concentration, scattering curves were superposed within data noise. One representative SANS curve of each condition was thus selected for further analysis (Table S2).

SANS data analysis:

Classical analysis: details are given in Tables S2. SANS data have been submitted to a classical Guinier analysis using NCNR-developed IGOR Macros [93] and PRIMUS [95], to extract the radii of gyration (Rg) and the intensities scattered in the forward direction (I(0)) of all samples. Pair distance distribution functions (p(r)) were obtained using GNOM from PRIMUS and SASVIEW (https://www.sasview.org/). Then, they have been evaluated using AMBIMETER online tool [47]. Finally, the p(r) functions have been used as input for *ab initio* methods.

Ab initio modelling [48]*:* concerning the low-ambiguity WT-ATP/Mg/Vi data, DAMMIN online was run 20 times, without symmetry constraints, to collect 20 independent bead models. The 20 models being very similar and uncorrelated according to CorMap [96], they have been averaged using DAMAVER [97] and the low-occurrence pieces of the structure have been filtered out using DAMFILT [97]. The resulting model has been refined using DAMMIN locally with DAMSTART parameters, in expert mode, with 25 harmonics and 80 knots, according to the advices of C. Jeffries, and superimposed to the BmrA OF structure (PDB 6R81) using SUPCOMB [98]. Concerning the highly ambiguous data of WT-Apo and WT-ADP samples, 40 independent bead models have been generated using DAMMIN online without symmetry constraint. They were not all similar and DAMCLUST [99] classified them in 5 clusters, confirming that *ab initio* modelling is not appropriate.

Model-based modeling: to further analyze the results, we assumed that BmrA was, in these conditions, in a conformational equilibrium. We first generated a large ensemble of conformations, from the 3 BmrA structure / homology models using, first, NOLB [100] to vary the TMD opening, and, second, rrt-sampling from MULTIFOX [49], to move NBD and His-Tag positions. NOLB was used to build a series of 10 intermediates between the BmrA OF structure and IF models. Redundant and conformations with steric clashes were discarded, leading to 2 additional conformations. The first non-linear Normal mode between two rigid bodies was applied to the wide-open IF model to obtain 80 more open and more closed structures, using NOLB and an amplitude parameter of 4. One of the rigid body contained selected amino-acids of A and B chains of BmrA dimer, A1-164, B169-274 and A278-605, the remaining amino-acids constituted the hinge. 32 clash-free models were selected out. From each of the 37 models, rrt conformation sampling routine of MULTIFOX was applied using command line version

and default settings, to move the NBD and His-Tag, sampling about 200 conformations. It resulted in a total of 7006 conformations. MULTIFOX was then used to fit the experimental SANS curves with a combination of 1, 2, 3 or 4 of all these conformations, with variable proportions. The resulting models show a large range of opening between the NBDs.

Hydrogen Deuterium Exchange coupled to Mass Spectrometry (HDX-MS): HDX-MS experiments were performed using an automated HDX system coupled to a Synapt G2Si mass spectrometer from Waters™. The reactions were carried out by a Leap HDX PAL robot (Trajan, USA). Labeling was initiated by diluting 5.5 µL, of typically 15 µM protein, in 104.5 µL D_2O labeling buffer (5 mM Hepes pD 8, 50 mM NaCl, 0.01% LMNG). For the ATP/Mg/Vi- and ATP/Mg-incubated samples, the labeling buffer contained additionally 10 mM ATP, 10 mM $MgCl_2$ and 1 mM Vi or 10 mM ATP, 10 mM $MgCl_2$, respectively. Prior to labeling, the samples were incubated with the respective ligands for 15 min at room temperature. Samples were labeled for 0.5, 2, 5, 15, 30 and 60 min at 20 °C. Subsequently, the reactions were quenched by adding 22 µL of ice-cold quenching buffer to 100 µL of labelled sample at 4 °C. For the WT, the quenching buffer contained 0.5 M glycine pH 2.2, 4 M guanidine-HCl and pepsin with protein to pepsin ratio of 4:1 (wt:wt), and digestion was done for 2 min in quenching buffer before injecting 110 µL of the quenched sample into a 100 µL loop. For the K380A mutant, the quenching buffer consisted of 0.5 M glycine pH 2.2 and 8 M guanidine-HCl and digestion was done on-line at 10 °C using a pepsin column (Waters Enzymate™ BEH Pepsin Column 300Å, 5 µm, 2.1 mm X 30 mm). In both cases, the resulting peptides were desalted for three min and trapped on a C18 precolumn (Waters™ UPLC BEH C18 Vanguard Pre-column) before separating them with a C18 column (Waters™ Acquity UPLC BEH C18 column) using a linear acetonitrile gradient of 5-40% in 13 min and then four alternative cycles of 5% and 95% until 25 min. The valve position was adjusted to divert the sample after 14 min of each run from C18 column to waste to avoid contaminating the mass spectrometer with detergent. Three full kinetics were run for each condition, one after the other, to get triplicates of each timepoint. Blanks with equilibration buffer (5 mM Hepes pH 8, 50 mM NaCl) were injected after each sample injection and pepsin column washed (when present) during each run with pepsin wash (1.5 M guanidine-HCl, 4% acetonitrile, 0.8% formic acid pH 2.5) to minimize the carryover.

Electrospray ionization Mass spectra were acquired in positive mode in the m/z range of 50−2000 and with a scan time of 0.3 s. For the identification of non-deuterated peptides, data were collected in MS^E mode and the resulting peptides were identified using PLGS™ software (ProteinLynx Global SERVER 3.0.2 from Waters™). Deuterated peptides were identified and analyzed using DynamX 3.0 software (Waters™), using the following parameters: minimum products per amino acid of 0.3 for WT BmrA and 0.2 for K380A BmrA and file threshold of 3 out of 7 for WT BmrA and 2 out of 5 for K380A BmrA. Deuteros 2.0 software [101] was used for data visualization and statistical analysis. The online web application HDX-Viewer [102] and PyMOL (The PyMOL Molecular Graphics System, Version 2.3.0 Schrödinger, LLC) were used to represent the HDX-MS data on either the IF model of BmrA based on PDB 3WME, or the OF structure of E504A BmrA (PDB 6R81). The program MODELLER [103] was used to make the IF model of BmrA based on P-gp (PDB identity code 3WME).

QUANTIFICATION AND STATISTICAL ANALYSIS: the program 'Deuteros' was used to assess the significance of the deuteration level of peptides generated by HDX-MS. Hybrid significance test with confidence interval of 98% and p-value<0.02 was used [104].

KEY RESOURCES TABLE

REAGENT or RESOURCE	SOURCE	IDENTIFIER

Bacterial and Virus Strains		
E. coli C41(DE3)	Sigma-Aldrich	https://www.sigmaaldrich.com/catalog/product/sigma/cmc0017?lang=fr&region=FR
Biological Samples		
Chemicals, Peptides, and Recombinant Proteins		
WT BmrA	[29]	https://doi.org/10.1021/bi0362018
E504Q BmrA	[39]	https://doi.org/10.1074/jbc.M308268200
K380A BmrA	[35]	https://doi.org/10.1021/bi702303s
d- WT BmrA	This manuscript	
d- E504Q BmrA	This manuscript	
d- K380A BmrA	This manuscript	
ADP	Sigma-Aldrich	A2754
Agar	Sigma-Aldrich	A7002
Ampicillin	Euromedex	EU0400-C
ATP	Sigma-Aldrich	10519979001
Deuterated minimal media	[82, 83]	https://doi.org/10.1007/s00249-016-1186-2 https://doi.org/10.1016/bs.mie.2015.11.001
Dithiothreitol (DTT)	Sigma-Aldrich	D0632
DNAse 1	Roche	10104159001

D_2O	Euriso-top	D216L
Ethylenediaminetetraacetic acid (EDTA)	Sigma-Aldrich	E9884
Glycerol	Euromedex	EU3550
Hepes	Sigma-Aldrich	H3375
Imidazole	Sigma-Aldrich	56750
Kanamycine	Euromedex	UK0010
Lactate dehydrogenase	Roche	10107085001
Laemmli buffer 5x	[105]	https://doi.org/10.1038/227680a0
LB media	Sigma-Aldrich	L3022
LMNG	Anatrace	NG310
Lysozyme	Sigma-Aldrich	L6876
Magnesium Chloride	Sigma-Aldrich	M8266
NADH	Roche	10128023001
NaOD	Eurisotop	D076Y
Pepsin	Sigma-Aldrich	P6887
Phosphoenol pyruvate	Sigma-Aldrich	P3637
Protease inhibitor cocktail	Roche	04693159001
Pyruvate kinase	Roche	10109045001
Sodium Chloride	Sigma-Aldrich	S5886
Sodium ortho-vanadate	Sigma-Aldrich	S6508
Sodium Phosphate dibasic	Sigma-Aldrich	S7907
Sodium Phosphate monobasic	Sigma-Aldrich	S8282
Sucrose	Sigma-Aldrich	S0389
Trifluoroacetic acid (TFA)	Solvants Distillation Synthese (SDS) Peypin France	
Tris base	Sigma-Aldrich	10708976001
Trypsin	Sigma-Aldrich	T1426

2 YT media	Sigma-Aldrich	Y2377
Critical Commercial Assays		
Pierce BCA protein assay kit	Thermo Fisher Scientific	23227
Deposited Data		
cryo-EM structure of E504A BmrA bound with ATP/Mg	[42]	6R81
SANS Data	This manuscript	doi.ill.fr/10.5291/ILL-DATA.BAG-8-36; doi.ill.fr/10.5291/ILL-DATA.BAG-8-37.
HDX-MS	This manuscript	PXD028663
Experimental Models: Organisms/Strains		
Oligonucleotides		
Primers to amplify *WT BmrA* gene form *pET23-bmrA*	*TataccatggcaCCAACCAAGAAACAAAAATCTAAAAGTAAATTGAA* and *CTTGTCGACCCCGGCTTT*	
Recombinant DNA		
pET23 WT bmrA	[29]	https://doi.org/10.1021/bi0362018
pET23 E504Q bmrA	[39]	https://doi.org/10.1074/jbc.M308268200
pET23 K380A bmrA	[35]	https://doi.org/10.1021/bi702303s
pET28 WT bmrA	This manuscript	

pET28 E504Q bmrA	This manuscript	
pET28 K380A bmrA	This manuscript	
Software and Algorithms		
For AUC & SEC-LS analysis		
ASTRA, v5.4.3.20	Wyatt, Santa-Barbara, USA	https://www.wyatt.com/products/software/astra.html
GUSSI	[87]	http://biophysics.swmed.edu/MBR/software.html
REDATE	[85]	http://biophysics.swmed.edu/MBR/software.html
SEDFIT	[86]	https://sedfitsedphat.nibib.nih.gov/
Software for SANS analysis		
AMBIMETER	[47]	https://doi.org/10.1107/S1399004715002576
CORMAP	[96]	https://doi.org/10.1038/nmeth.3358
DAMAVER	[97]	https://doi.org/10.1107/S0021889803000268
DAMCLUST	[99]	https://doi.org/10.1107/S0021889812007662
DAMFILT	[97]	https://doi.org/10.1107/S0021889803000268
DAMMIN	[48]	https://doi.org/10.1016/S0006-3495(99)77443-6

DAMSTART	[97]	https://doi.org/10.1107/S0021889803000268
IGOR Pro		https://www.wavemetrics.com/
GNOM	[106]	https://doi.org/10.1107/S0021889892001663
GRASP	https://www.ill.eu/users/support-labs-infrastructure/software-scientific-tools/grasp	
MULTIFOXS	[49]	https://doi.org/10.1093/nar/gkw389
NCNR-developped IGOR Macros	[93]	https://doi.org/10.1107/S0021889806035059
NOLB	[100]	https://doi.org/10.1021/acs.jctc.7b00197
PRIMUS qt V2.8.4	[95]	https://doi.org/10.1107/S0021889803012779
SASVIEW	www.sasview.org	
SUPCOMB	[98]	https://doi.org/10.1107/S0021889800014126
Swiss-model	[90]	https://doi.org/10.1093/nar/gky427
Software for HDX-MS analysis		
Deuteros	[101]	https://doi.org/10.1093/bioinformatics/btaa677
DynamX HDX Data Analysis Software 3.0	Waters corporation	https://www.waters.com

HDX Viewer	[102]	https://doi.org/10.1093/bioinformatics/btz550
ProteinLynx Global SERVER (PLGS)	Waters corporation	https://www.waters.com
Other softwares		
PR.thermocontrol V2.0.4	Nanotemper Technologies	https://nanotempertech.com/prometheus/
PyMOL	https://pymol.org	The PyMOL Molecular Graphics System, Version 2.3.0 Schrödinger, LLC
Quark web application (in silico folding of the tag)	[91]	https://doi.org/10.1002/prot.24065
UCSF Chimera	[107]	https://doi.org/10.1002/jcc.20084
Other		
4 mL100 kDa cutoff concentrator (Amicon Ultra-4)	Millipore	UFC810096

REFERENCES

1. Davidson, A.L., et al., *Structure, function, and evolution of bacterial ATP-binding cassette systems.* Microbiol Mol Biol Rev, 2008. **72**(2): p. 317-64.
2. Rees, D.C., E. Johnson, and O. Lewinson, *ABC transporters: the power to change.* Nat Rev Mol Cell Biol, 2009. **10**(3): p. 218-27.
3. Csanady, L., P. Vergani, and D.C. Gadsby, *Structure, Gating, and Regulation of the Cftr Anion Channel.* Physiol Rev, 2019. **99**(1): p. 707-738.
4. Silverton, L., M. Dean, and K. Moitra, *Variation and evolution of the ABC transporter genes ABCB1, ABCC1, ABCG2, ABCG5 and ABCG8: implication for pharmacogenetics and disease.* Drug Metabol Drug Interact, 2011. **26**(4): p. 169-79.
5. Assaraf, Y.G., et al., *The multi-factorial nature of clinical multidrug resistance in cancer.* Drug Resist Updat, 2019. **46**: p. 100645.
6. Orelle, C., K. Mathieu, and J.M. Jault, *Multidrug ABC transporters in bacteria.* Res Microbiol, 2019. **170**(8): p. 381-391.

7. Thomas, C. and R. Tampe, *Structural and Mechanistic Principles of ABC Transporters.* Annu Rev Biochem, 2020. **89**: p. 605-636.
8. Thomas, C., et al., *Structural and functional diversity calls for a new classification of ABC transporters.* FEBS Lett, 2020. **594**(23): p. 3767-3775.
9. Jardetzky, O., *Simple allosteric model for membrane pumps.* Nature, 1966. **211**(5052): p. 969-70.
10. Lewinson, O., C. Orelle, and M.A. Seeger, *Structures of ABC transporters: handle with care.* FEBS Lett, 2020. **594**(23): p. 3799-3814.
11. Jones, P.M. and A.M. George, *Mechanism of the ABC transporter ATPase domains: catalytic models and the biochemical and biophysical record.* Crit Rev Biochem Mol Biol, 2013. **48**(1): p. 39-50.
12. Higgins, C.F. and K.J. Linton, *The ATP switch model for ABC transporters.* Nat Struct Mol Biol, 2004. **11**(10): p. 918-26.
13. van der Does, C. and R. Tampe, *How do ABC transporters drive transport?* Biol Chem, 2004. **385**(10): p. 927-33.
14. Locher, K.P., *Mechanistic diversity in ATP-binding cassette (ABC) transporters.* Nat Struct Mol Biol, 2016. **23**(6): p. 487-93.
15. Moeller, A., et al., *Distinct conformational spectrum of homologous multidrug ABC transporters.* Structure, 2015. **23**(3): p. 450-460.
16. Thelot, F.A., et al., *Distinct allosteric mechanisms of first-generation MsbA inhibitors.* Science, 2021. **374**(6567): p. 580-585.
17. Ward, A., et al., *Flexibility in the ABC transporter MsbA: Alternating access with a twist.* Proc Natl Acad Sci U S A, 2007. **104**(48): p. 19005-19010.
18. Padayatti, P.S., et al., *Structural Insights into the Lipid A Transport Pathway in MsbA.* Structure, 2019. **27**(7): p. 1114-1123 e3.
19. Moradi, M. and E. Tajkhorshid, *Mechanistic picture for conformational transition of a membrane transporter at atomic resolution.* Proc Natl Acad Sci U S A, 2013. **110**(47): p. 18916-21.
20. Wen, P.C., et al., *On the origin of large flexibility of P-glycoprotein in the inward-facing state.* J Biol Chem, 2013. **288**(26): p. 19211-20.
21. Frank, G.A., et al., *Cryo-EM Analysis of the Conformational Landscape of Human P-glycoprotein (ABCB1) During its Catalytic Cycle.* Mol Pharmacol, 2016. **90**(1): p. 35-41.
22. Hofmann, S., et al., *Conformation space of a heterodimeric ABC exporter under turnover conditions.* Nature, 2019. **571**(7766): p. 580-583.
23. Hohl, M., et al., *Crystal structure of a heterodimeric ABC transporter in its inward-facing conformation.* Nat Struct Mol Biol, 2012. **19**(4): p. 395-402.
24. Hohl, M., et al., *Structural basis for allosteric cross-talk between the asymmetric nucleotide binding sites of a heterodimeric ABC exporter.* Proc Natl Acad Sci U S A, 2014. **111**(30): p. 11025-30.
25. Kim, J., et al., *Subnanometre-resolution electron cryomicroscopy structure of a heterodimeric ABC exporter.* Nature, 2015. **517**(7534): p. 396-400.
26. Liu, Y., et al., *Single-molecule fluorescence studies on the conformational change of the ABC transporter MsbA.* Biophys Rep, 2018. **4**(3): p. 153–165.
27. Clouser, A.F., Y.H. Alam, and W.M. Atkins, *Cholesterol Asymmetrically Modulates the Conformational Ensemble of the Nucleotide-Binding Domains of P-Glycoprotein in Lipid Nanodiscs.* Biochemistry, 2021. **60**(1): p. 85-94.
28. Krugel, H., et al., *Cervimycin C resistance in Bacillus subtilis is due to a promoter up-mutation and increased mRNA stability of the constitutive ABC-transporter gene bmrA.* FEMS Microbiol Lett, 2010. **313**(2): p. 155-63.
29. Steinfels, E., et al., *Characterization of YvcC (BmrA), a Multidrug ABC Transporter Constitutively Expressed in Bacillus subtilis.* Biochemistry, 2004. **43**(23): p. 7491-7502.

30. Dalmas, O., et al., *Time-Resolved Fluorescence Resonance Energy Transfer Shows that the Bacterial Multidrug ABC Half-Transporter BmrA Functions as a Homodimer.* Biochemistry, 2005. **44**(11): p. 4312-4321.
31. Mathieu, K., et al., *Functionality of membrane proteins overexpressed and purified from E. coli is highly dependent upon the strain.* Sci Rep, 2019. **9**(1): p. 2654.
32. Breyton, C., et al., *Assemblies of lauryl maltose neopentyl glycol (LMNG) and LMNG-solubilized membrane proteins.* Biochim Biophys Acta Biomembr, 2019. **1861**(5): p. 939-957.
33. Mehmood, S., et al., *Dynamics of a bacterial multidrug ABC transporter in the inward- and outward-facing conformations.* Proc Natl Acad Sci U S A, 2012. **109**(27): p. 10832-6.
34. Lacabanne, D., et al., *Flexible-to-rigid transition is central for substrate transport in the ABC transporter BmrA from Bacillus subtilis.* Commun Biol, 2019. **2**: p. 149.
35. Orelle, C., et al., *Conformational change induced by ATP binding in the multidrug ATP-binding cassette transporter BmrA.* Biochemistry, 2008. **47**(8): p. 2404-12.
36. Geourjon, C., et al., *A common mechanism for ATP hydrolysis in ABC transporter and helicase superfamilies.* Trends Biochem Sci, 2001. **26**(9): p. 539-44.
37. Priess, M., et al., *Molecular Mechanism of ATP Hydrolysis in an ABC Transporter.* ACS Cent Sci, 2018. **4**(10): p. 1334-1343.
38. Oldham, M.L. and J. Chen, *Snapshots of the maltose transporter during ATP hydrolysis.* Proc Natl Acad Sci U S A, 2011. **108**(37): p. 15152-6.
39. Orelle, C., et al., *The Conserved Glutamate Residue Adjacent to the Walker-B Motif Is the Catalytic Base for ATP Hydrolysis in the ATP-binding Cassette Transporter BmrA.* J Biol Chem, 2003. **278**(47): p. 47002-8.
40. Engen, J.R. and E.A. Komives, *Complementarity of Hydrogen/Deuterium Exchange Mass Spectrometry and Cryo-Electron Microscopy.* Trends Biochem Sci, 2020. **45**(10): p. 906-918.
41. Gabel, F., *Applications of SANS to Study Membrane Protein Systems.* Adv Exp Med Biol, 2017. **1009**: p. 201-214.
42. Chaptal, V., et al., *Substrate-bound and substrate-free outward-facing structures of a multidrug ABC exporter.* Sci Adv, 2022. **8**(4): p. eabg9215.
43. Jacrot, B. and G. Zaccai, *Determination of molecular weight by neutron scattering.* Biopolymers, 1981. **20**: p. 2413-2426.
44. Rambo, R.P. and J.A. Tainer, *Accurate assessment of mass, models and resolution by small-angle scattering.* Nature, 2013. **496**(7446): p. 477-81.
45. Le Roy, A., et al., *Sedimentation velocity analytical ultracentrifugation in hydrogenated and deuterated solvents for the characterization of membrane proteins.* Methods Mol Biol, 2013. **1033**: p. 219-51.
46. Kodan, A., et al., *Structural basis for gating mechanisms of a eukaryotic P-glycoprotein homolog.* Proc Natl Acad Sci U S A, 2014. **111**(11): p. 4049-54.
47. Petoukhov, M.V. and D.I. Svergun, *Ambiguity assessment of small-angle scattering curves from monodisperse systems.* Acta Crystallogr D Biol Crystallogr, 2015. **71**(Pt 5): p. 1051-8.
48. Svergun, D.I., *Restoring low resolution structure of biological macromolecules from solution scattering using simulated annealing.* Biophys J, 1999. **76**(6): p. 2879-86.
49. Schneidman-Duhovny, D., et al., *FoXS, FoXSDock and MultiFoXS: Single-state and multi-state structural modeling of proteins and their complexes based on SAXS profiles.* Nucleic Acids Res, 2016. **44**(W1): p. W424-9.
50. Oganesyan, I., C. Lento, and D.J. Wilson, *Contemporary hydrogen deuterium exchange mass spectrometry.* Methods, 2018. **144**: p. 27-42.
51. Josts, I., et al., *Conformational States of ABC Transporter MsbA in a Lipid Environment Investigated by Small-Angle Scattering Using Stealth Carrier Nanodiscs.* Structure, 2018. **26**(8): p. 1072-1079 e4.
52. Maric, S., et al., *Stealth carriers for low-resolution structure determination of membrane proteins in solution.* Acta Crystallogr D Biol Crystallogr, 2014. **70**(Pt 2): p. 317-28.

53. Borbat, P.P., et al., *Conformational Motion of the ABC Transporter MsbA Induced by ATP Hydrolysis.* PLoS Biol, 2007. **5**(10): p. e271.
54. Zou, P., M. Bortolus, and H.S. McHaourab, *Conformational cycle of the ABC transporter MsbA in liposomes: detailed analysis using double electron-electron resonance spectroscopy.* J Mol Biol, 2009. **393**(3): p. 586-97.
55. Wiseman, B., et al., *Stubborn contaminants: influence of detergents on the purity of the multidrug ABC transporter BmrA.* PLoS One, 2014. **9**(12): p. e114864.
56. Carey Hulyer, A.R., et al., *Cross-linking, DEER-spectroscopy and molecular dynamics confirm the inward facing state of P-glycoprotein in a lipid membrane.* J Struct Biol, 2020. **211**(1): p. 107513.
57. Ho, H., et al., *Structural basis for dual-mode inhibition of the ABC transporter MsbA.* Nature, 2018. **557**(7704): p. 196-201.
58. Mi, W., et al., *Structural basis of MsbA-mediated lipopolysaccharide transport.* Nature, 2017. **549**(7671): p. 233-237.
59. Seelig, A., *A general pattern for substrate recognition by P-glycoprotein.* Eur J Biochem, 1998. **251**(1-2): p. 252-61.
60. Aller, S.G., et al., *Structure of P-glycoprotein reveals a molecular basis for poly-specific drug binding.* Science, 2009. **323**(5922): p. 1718-22.
61. Li, J., K.F. Jaimes, and S.G. Aller, *Refined structures of mouse P-glycoprotein.* Protein Sci, 2014. **23**(1): p. 34-46.
62. Shapiro, A.B. and V. Ling, *Positively cooperative sites for drug transport by P-glycoprotein with distinct drug specificities.* Eur J Biochem, 1997. **250**(1): p. 130-7.
63. Martin, C., et al., *Communication between multiple drug binding sites on P-glycoprotein.* Mol Pharmacol, 2000. **58**(3): p. 624-32.
64. Marcoux, J., et al., *Mass spectrometry reveals synergistic effects of nucleotides, lipids, and drugs binding to a multidrug resistance efflux pump.* Proc Natl Acad Sci U S A, 2013. **110**(24): p. 9704-9.
65. Kopcho, N., G. Chang, and E.A. Komives, *Dynamics of ABC Transporter P-glycoprotein in Three Conformational States.* Sci Rep, 2019. **9**(1): p. 15092.
66. Hellmich, U.A., et al., *Probing the ATP hydrolysis cycle of the ABC multidrug transporter LmrA by pulsed EPR spectroscopy.* J Am Chem Soc, 2012. **134**(13): p. 5857-62.
67. Sigoillot, M., et al., *Domain-interface dynamics of CFTR revealed by stabilizing nanobodies.* Nat Commun, 2019. **10**(1): p. 2636.
68. Tombline, G., et al., *Involvement of the "occluded nucleotide conformation" of p-glycoprotein in the catalytic pathway.* Biochemistry, 2005. **44**(38): p. 12879-86.
69. Lusvarghi, S. and S.V. Ambudkar, *ATP-dependent thermostabilization of human P-glycoprotein (ABCB1) is blocked by modulators.* Biochem J, 2019. **476**(24): p. 3737-3750.
70. Ishii, S., et al., *Boundary of the nucleotide-binding domain of Streptococcus ComA based on functional and structural analysis.* Biochemistry, 2013. **52**(15): p. 2545-55.
71. Shintre, C.A., et al., *Structures of ABCB10, a human ATP-binding cassette transporter in apo- and nucleotide-bound states.* Proc Natl Acad Sci U S A, 2013. **110**(24): p. 9710-5.
72. Li, S., et al., *Cryo-EM structure of human ABCB8 transporter in nucleotide binding state.* Biochem Biophys Res Commun, 2021. **557**: p. 187-191.
73. Lu, G., et al., *ATP hydrolysis is required to reset the ATP-binding cassette dimer into the resting-state conformation.* Proc Natl Acad Sci U S A, 2005. **102**(50): p. 17969-74.
74. Smith, P.C., et al., *ATP binding to the motor domain from an ABC transporter drives formation of a nucleotide sandwich dimer.* Mol Cell, 2002. **10**(1): p. 139-49.
75. Jones, P.M. and A.M. George, *Opening of the ADP-bound active site in the ABC transporter ATPase dimer: evidence for a constant contact, alternating sites model for the catalytic cycle.* Proteins, 2009. **75**(2): p. 387-96.
76. Wen, P.C. and E. Tajkhorshid, *Dimer opening of the nucleotide binding domains of ABC transporters after ATP hydrolysis.* Biophys J, 2008. **95**(11): p. 5100-10.

77. Dawson, R.J. and K.P. Locher, *Structure of a bacterial multidrug ABC transporter.* Nature, 2006. **443**(7108): p. 180-5.
78. Chen, J., et al., *A tweezers-like motion of the ATP-binding cassette dimer in an ABC transport cycle.* Mol Cell, 2003. **12**(3): p. 651-61.
79. Yang, Z., et al., *Interactions and cooperativity between P-glycoprotein structural domains determined by thermal unfolding provides insights into its solution structure and function.* Biochim Biophys Acta Biomembr, 2017. **1859**(1): p. 48-60.
80. Orelle, C. and J.M. Jault, *Structures and Transport Mechanisms of the ABC Efflux Pumps*, in *Efflux-Mediated Antimicrobial Resistance in Bacteria*, X.Z. Li, C.A. Elkins, and H.I. Zgurskaya, Editors. 2016, Springer. p. 73-98.
81. Perez-Riverol, Y., et al., *The PRIDE database and related tools and resources in 2019: improving support for quantification data.* Nucleic Acids Res, 2019. **47**(D1): p. D442-D450.
82. Dunne, O., et al., *Matchout deuterium labelling of proteins for small-angle neutron scattering studies using prokaryotic and eukaryotic expression systems and high cell-density cultures.* Eur Biophys J, 2017. **46**(5): p. 425-432.
83. Haertlein, M., et al., *Biomolecular Deuteration for Neutron Structural Biology and Dynamics.* Methods Enzymol, 2016. **566**: p. 113-57.
84. Signor, L. and E. Boeri Erba, *Matrix-assisted laser desorption/ionization time of flight (MALDI-TOF) mass spectrometric analysis of intact proteins larger than 100 kDa.* J Vis Exp, 2013(79).
85. Zhao, H., et al., *Recorded scan times can limit the accuracy of sedimentation coefficients in analytical ultracentrifugation.* Anal Biochem, 2013. **437**(1): p. 104-8.
86. Schuck, P., *Size-distribution analysis of macromolecules by sedimentation velocity ultracentrifugation and lamm equation modeling.* Biophys J, 2000. **78**(3): p. 1606-19.
87. Brautigam, C.A., *Calculations and Publication-Quality Illustrations for Analytical Ultracentrifugation Data.* Methods Enzymol, 2015. **562**: p. 109-33.
88. Le Roy, A., et al., *AUC and Small-Angle Scattering for Membrane Proteins.* Methods Enzymol, 2015. **562**: p. 257-86.
89. Boncoeur, E., et al., *PatA and PatB form a functional heterodimeric ABC multidrug efflux transporter responsible for the resistance of Streptococcus pneumoniae to fluoroquinolones.* Biochemistry, 2012. **51**(39): p. 7755-65.
90. Waterhouse, A., et al., *SWISS-MODEL: homology modelling of protein structures and complexes.* Nucleic Acids Res, 2018. **46**(W1): p. W296-W303.
91. Xu, D. and Y. Zhang, *Ab initio protein structure assembly using continuous structure fragments and optimized knowledge-based force field.* Proteins, 2012. **80**(7): p. 1715-35.
92. Trewhella, J., et al., *2017 publication guidelines for structural modelling of small-angle scattering data from biomolecules in solution: an update.* Acta Crystallogr D Struct Biol, 2017. **73**(Pt 9): p. 710-728.
93. Kline, S.R., *Reduction and analysis of SANS and USANS data using IGOR Pro.* J Appl Crystallogr, 2006. **39**: p. 895-900.
94. Manalastas-Cantos, K., et al., *ATSAS 3.0: expanded functionality and new tools for small-angle scattering data analysis.* J Appl Crystallogr, 2021. **54**(Pt 1): p. 343-355.
95. Konarev, P.V., et al., *PRIMUS: a Windows PC-based system for small-angle scattering data analysis.* J Appl Crystallogr, 2003. **36**: p. 1277-1882.
96. Franke, D., C.M. Jeffries, and D.I. Svergun, *Correlation Map, a goodness-of-fit test for one-dimensional X-ray scattering spectra.* Nat Methods, 2015. **12**(5): p. 419-22.
97. Volkov, V.V. and D.I. Svergun, *Uniqueness of ab initio shape determination in small-angle scattering.* J Appl Crystallogr, 2003. **36**: p. 860-864.
98. Kozin, M.B. and D.I. Svergun, *Automated matching of high- and low-resolution structural models.* J Appl Crystallogr, 2001. **34**: p. 33-41.
99. Petoukhov, M.V., et al., *New developments in the ATSAS program package for small-angle scattering data analysis.* J Appl Crystallogr, 2012. **45**(Pt 2): p. 342-350.

100. Hoffmann, A. and S. Grudinin, *NOLB: Nonlinear Rigid Block Normal-Mode Analysis Method.* J Chem Theory Comput, 2017. **13**(5): p. 2123-2134.
101. Lau, A.M., et al., *Deuteros 2.0: peptide-level significance testing of data from hydrogen deuterium exchange mass spectrometry.* Bioinformatics, 2021. **37**(2): p. 270-272.
102. Bouyssie, D., et al., *HDX-Viewer: interactive 3D visualization of hydrogen-deuterium exchange data.* Bioinformatics, 2019. **35**(24): p. 5331-5333.
103. Webb, B. and A. Sali, *Comparative Protein Structure Modeling Using MODELLER.* Curr Protoc Protein Sci, 2016. **86**: p. 2 9 1-2 9 37.
104. Hageman, T.S. and D.D. Weis, *Reliable Identification of Significant Differences in Differential Hydrogen Exchange-Mass Spectrometry Measurements Using a Hybrid Significance Testing Approach.* Anal Chem, 2019. **91**(13): p. 8008-8016.
105. Laemmli, U.K., *Cleavage of structural proteins during the assembly of the head of bacteriophage T4.* Nature, 1970. **227**(5259): p. 680-5.
106. Svergun, D.I., *Determination of the regularization parameter in indirect-transform methods using perceptual criteria.* J Appl Crystallogr, 1992. **25**(4): p. 495-503.
107. Pettersen, E.F., et al., *UCSF Chimera--a visualization system for exploratory research and analysis.* J Comput Chem, 2004. **25**(13): p. 1605-12.

Revised Manuscript (UNmarked, docx or tex file) Click here to view linked References

Structural insights into the catalytic cycle of a bacterial multidrug ABC efflux pump

Waqas Javed[1,2,3], Sylvain Vallet[1], Marie-Pierre Clement[1], Aline Le Roy[2], Martine Moulin[3], Michael Härtlein[3], Cécile Breyton[2], Odile Burlet-Schiltz[4], Julien Marcoux*[4], Cédric Orelle*[1], Christine Ebel*[2], Anne Martel*[3] and Jean-Michel Jault*[1]

[1] Molecular Microbiology & Structural Biochemistry (MMSB) UMR 5086; CNRS/University of Lyon; Lyon, 69367; France. [2] IBS; Univ. Grenoble Alpes, CNRS, CEA; Grenoble, 38000; France. [3]Institut Max Von Laue Paul Langevin (ILL); Grenoble, 38000 ; France. [4]Institut de Pharmacologie et de Biologie Structurale ; Université de Toulouse, CNRS; Toulouse, 31000; France.

Further information and requests for resources and analysis should be directed to the lead contact, Jean-Michel Jault (jean-michel.jault@ibcp.fr). Correspondence: julien.marcoux@ipbs.fr; cedric.orelle@ibcp.fr; christine.ebel@ibs.fr; martela@ill.fr; jean-michel.jault@ibcp.fr

Summary

ABC ("ATP-Binding Cassette") transporters of the type IV subfamily consist of exporters involved in the efflux of many compounds, notably those capable to confer multidrug resistance like the mammalian P-glycoprotein or the bacterial transporter BmrA. They function according to an alternating access mechanism between inward-facing (IF) and outward-facing (OF) conformations, but the extent of physical separation between the two nucleotide-binding domains (NBDs) in different states is still unsettled. Small Angle Neutron Scattering and hydrogen/deuterium exchange coupled to mass spectrometry were used to highlight different conformational states of BmrA during its ATPase cycle. In particular, mutation of the conserved Lysine residue of the Walker-A motif (K380A) captures BmrA in an ATP-bound IF conformation prior to NBD closure. While in the transition-like state induced by vanadate wild-type BmrA is mainly in an OF conformation, the transporter populates only IF conformations in either the apo state or in the presence of ADP/Mg. Importantly, in this post-hydrolytic step, distances between the two NBDs of BmrA seem to be more separated than in the apo state, but they remain shorter than the widest opening found in the related MsbA transporter. Overall, our results highlight the main steps of the catalytic cycle of a homodimeric bacterial multidrug transporter and underline structural and functional commonalities as well as oddities among the type IV subfamily of ABC transporters.

Keywords

Small Angle Neutron Scattering, Hydrogen Deuterium exchange, membrane protein, multidrug transporter, ATP-binding cassette.

Introduction

ATP Binding Cassette (ABC) exporters are ATP-driven ubiquitous proteins that are involved in the translocation of many different compounds across membranes [1, 2]. They play key roles in many physiological functions and in humans their dysfunction is linked to several diseases including cystic fibrosis, tangier disease and Dubin-Johnson syndrome [3, 4]. Some ABC transporters can expel a wide array of molecules with unrelated chemical structures thereby protecting cells from noxious compounds. Hence, their overexpression in cancer cells or pathogens often result in multidrug resistant phenotypes leading to the failure of therapies [5, 6]. All ABC transporters share a common basic architecture including two nucleotide-binding domains (NBDs)[1] that bind and hydrolyze ATP, and two transmembrane domains (TMDs) that form the substrate translocation pathway [7]. Importantly, the 3D structure of exporters of the type IV subfamily reveals that the two intracellular domains (ICD1 and ICD2 in a homodimer) extending from the TMD and connecting the transmembrane helices 2 - 3 and 4 – 5, respectively, are key elements for the coupling between the TMDs and the NBDs. Hence, whereas ICD1 interacts with its own NBD, ICD2 interacts in *trans* with the NBD of the second monomer allowing a permanent cross-talk between the two monomers of homo- or hetero-dimers, or between the two moieties of full-length transporters [8]. The original postulate that ABC exporters of the type IV subfamily work according to an alternating access mechanism [9] is now supported by many pieces of evidence [10]; they switch between an apo state, or inward-facing (IF) conformation with the NBDs physically separated, to an outward-facing (OF) conformation prone to drug release and with the two NBDs engaged in a tight interaction while sandwiching two ATP molecules at their interface [6]. This transition from IF to OF states is triggered by ATP binding while ATP hydrolysis is supposed to reset the transporter to its IF conformation [7]. Yet, the extent of the NBD separation in IF conformations is still a matter of debate [11-13]. It may vary according to the intrinsic property of each transporter, i.e. its energy landscape that is possibly linked to the substrate transported [10], or even depends on the drug

[1] Abbreviations : AUC, Analytical UltraCentrifugation ; BmrA, *Bacillus* multidrug resistance ATP; Cryo-EM, Cryo-Electron Micropscopy; DDM, Dodecyl-β-D-maltoside; ICD, IntraCellular Domain; HDX-MS, H/D exchange coupled to mass spectrometry; IF, Inward Facing; LMNG, Lauryl Maltose Neopentyl Glycol ; MD, Molecular Dynamic; NBD, Nucleotide-Binding Domain ; OF, Outward Facing; Rg, radius of gyration; SANS, Small Angle Neutron Scattering; SEC-LS, Size Exclusion Chromatography coupled to Light Scattering; T_m, melting temperature; TMD, TransMembrane Domain; Vi, Vanadate; woIF, wide-open IF, WT, Wild-Type.

effluxed for multidrug transporters [14]. A large opening between the NBDs of MsbA has been observed by electron microscopy [15, 16], consistent with that found in X-ray structures [17, 18]. Molecular dynamic (MD) simulations also supports a large flexibility of MsbA in its resting state [19]. P-glycoprotein (P-gp), on the other hand, seems to be more constrained for the physical separation of its NBDs [15], yet a large fluctuation in the distance between its NBDs has been observed by MD simulation and EPR spectroscopy [20] and also by cryo-electron microscopy (Cryo-EM) [21]. For asymmetric ABC exporters with two non-equivalent NBDs, the opening in the IF conformation appears rather limited, even in the apo state [22-25]. In addition, the conformational landscape can be affected by the protein environment as well, i.e. detergent, nanodiscs or proteoliposomes [26], or the lipid composition [27].

Here, we investigated a multidrug ABC exporter from *Bacillus subtilis*, BmrA (*Bacillus* multidrug resistance ATP), which confers resistance *in vivo* to the cervimycin C antibiotic [28]. BmrA is a bacterial homologue of mammalian P-gp [29] and it functions as a homodimer [30]. It can be obtained in a detergent solubilized state in a very active ATPase form [31, 32]. H/D exchange coupled to mass spectrometry (HDX-MS) of BmrA in detergent micelles or solid-state NMR after reconstitution of the transporter into a lipidic environment highlighted two very different conformations in apo or ATP-trapped states [33, 34]. Our aim here was to identify and characterize additional conformational states of BmrA during its catalytic cycle to better understand its overall functioning mechanism. In particular, we sought to address IF conformations in the presence of nucleotides. For this purpose, we used the wild-type (WT) BmrA with ADP/Mg to characterize the post-hydrolytic step, and a mutant of the invariant Lysine of the Walker-A motif, K380A, as it was thought to be impaired in the NBD dimerization step [35]. We also took advantage of another ATPase inactive mutant, the E504Q. This glutamate residue is the putative catalytic base for ATPase activity in ABC transporters [36-39]. The inactive E504Q mutant can be trapped in a pre-hydrolytic ATP/Mg-bound state [33, 34, 39] and was compared to the transition-state conformation of WT reached upon vanadate inhibition (ATP/Mg/Vi) [38]. The different proteins were characterized by “in solution” techniques, mainly Small Angle Neutron Scattering (SANS) and HDX-MS, as they both have shown to nicely complement high resolution static

pictures obtained by X-ray crystallography, NMR or Cryo-EM [40, 41]. Overall, we present a dynamic view of the catalytic cycle of BmrA that switches between different IF conformations in the resting state, with a moderate opening between its two NBDs as compared to MsbA, to an OF conformation in the transition state similar to the ATP-bound state of the E504Q mutant. Importantly, in the post-hydrolytic ADP/Mg-bound state, the physical separation between the two NBDs of BmrA is increased as compared to the apo state shedding light on an essential feature of the catalytic cycle of this transporter.

Results

Thermal stability and limited proteolysis reveal that BmrA mutants can be arrested at different steps of the catalytic cycle. Figure 1 reports on the denaturation curves and melting temperatures (T_m) for WT and mutants of BmrA in the apo states, or in the presence of various nucleotides. For WT-ATP/Mg/Vi, a major increase in T_m is observed compared to the apo state, from ~ 44 to 58 °C.

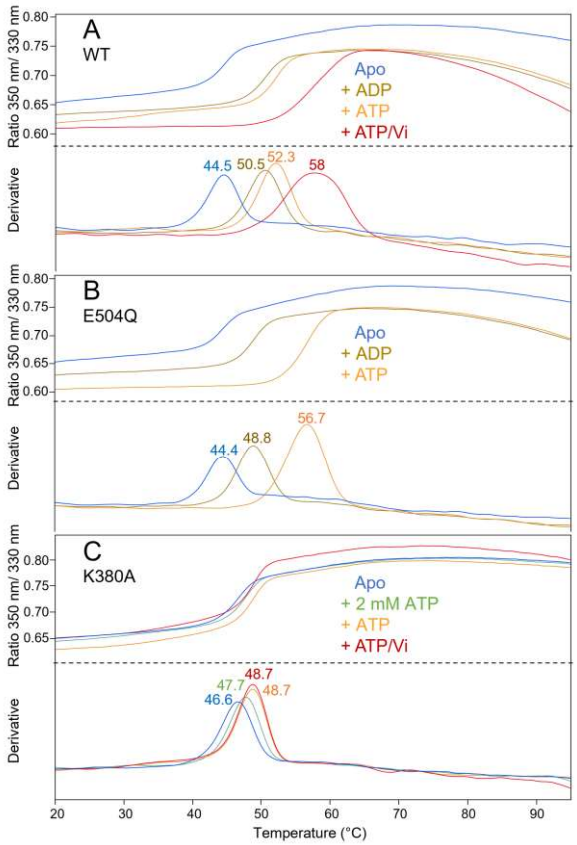

Figure 1. Thermal stability of WT BmrA and mutants and effect of nucleotides. Ratio of fluorescence emitted at 350 and 330 nm and first-derivatives with T_m (upper and lower sub-panels, respectively) for **A**: WT, wild-type BmrA. **B**: E504Q mutant and **C**: K380A mutant. Unless otherwise specified, ADP or ATP were added at 10 mM in the presence of 10 mM $MgCl_2$; When 2 mM ATP was used, 3 mM $MgCl_2$ were added; Vi was added at 1 mM. These experiments were reproduced at least three times from two different batches of purified proteins and with triplicate each time; a representative experiment is shown here.

The enhanced thermal stabilization induced by vanadate trapping is in agreement with previous results [32], and it is consistent with a large conformational change, as the protein switches from IF to OF conformations and remains trapped in this state. In the presence of ATP/Mg or ADP/Mg, the T_m is intermediate at 52 °C and 50 °C, respectively. In the former case, BmrA can hydrolyze ATP (until ADP has accumulated enough to inhibit ATPase activity) and is therefore switching between IF and OF conformations, whereas the binding of ADP/Mg produced an intermediate effect. The catalytically inactive E504Q BmrA mutant, in presence of ATP/Mg, shows an elevated T_m slightly lower than that of WT-ATP/Mg/Vi, providing further evidence of its trapping in the OF conformation [34, 39]. This result is in agreement with the recently solved 3D structure of the E504A mutant in an ATP-Mg bound state [42]. In the presence of ADP/Mg, this mutant shows a T_m similar to the WT. In contrast, the ATPase-inactive K380A mutant shows a modest, but significant, stabilization in the presence of ATP/Mg or ATP/Mg/Vi compared to the Apo form (> 2 °C). This suggests that the binding of ATP/Mg by the K380A, despite its weaker binding ability [35], does not produce a large conformational change, consistent with the assumption that this mutant is unable to reach the OF conformation.

Limited proteolysis was then performed to further analyze the global effect of nucleotides on our different constructs. As previously reported for the WT [32], incubation with ATP/Mg/Vi induced a full protection, up to 4 hours, against trypsin digestion (Figure 2, panels A-B).

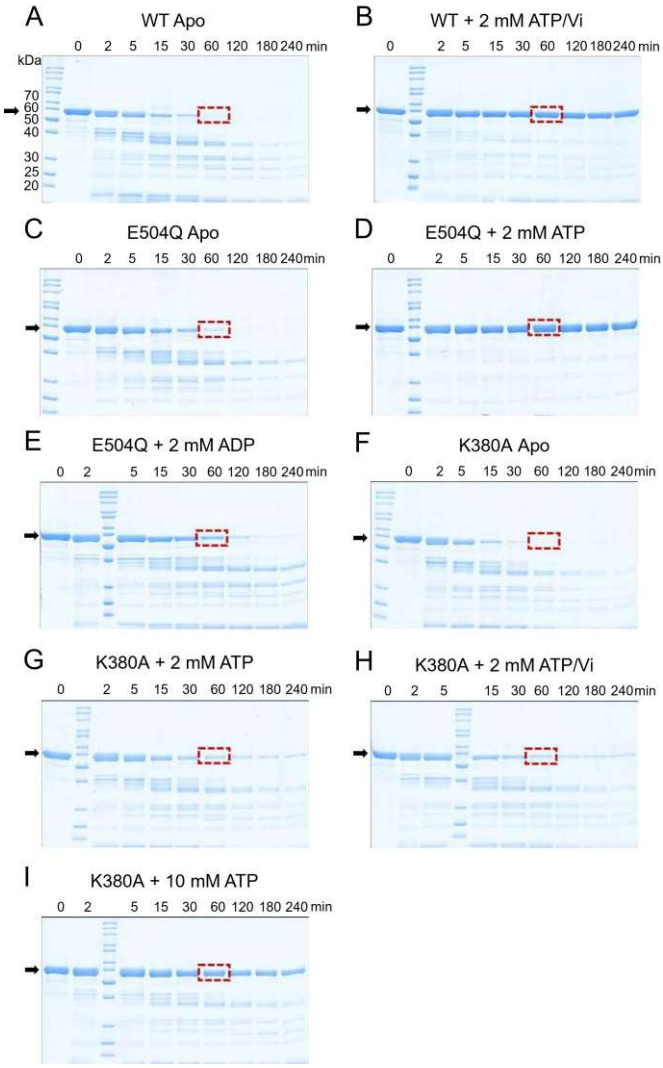

Figure 2. Limited proteolysis of K380A and E504Q mutants compared to WT BmrA. After incubation with the indicated ligands, BmrA WT (**A**-**B**), E504Q (**C**-**E**), or K380A mutants (**F**-**I**) were treated with trypsin for various times. $MgCl_2$ was added at 3 or 10 mM when 2 or 10 mM nucleotides were used, respectively. Vi was added at 1 mM. All samples were in 0.01% LMNG. Time zero was taken just before adding trypsin and the proteins were resolved using a 12% SDS PAGE. The arrows indicate the position of intact BmrA. Red boxes highlight the bands after 60 min of digestion. These experiments were reproduced at least three times from at least two different batches of purified proteins and a representative experiment is shown here.

A similar level of protection was afforded by ATP/Mg for the E504Q mutant while ADP/Mg showed a much-reduced effect (Figure 2, panels C-E). For the K380A mutant, a significant reduction in proteolysis digestion was obtained with 2 mM ATP/3 mM Mg, whether or not Vi was present, and this effect was strongly amplified in the presence of 10 mM ATP/Mg since about half of the proteins remained undigested (Figure 2, panels F-I). These experiments confirm the ability of this mutant to bind nucleotides when ATP is added in large excess, but they do not explain if the protection provided by ATP is due to a local (i.e. ATP binding to NBD) or a global effect on the whole protein (i.e.

conformational change due to NBD closure). To resolve this question, we performed SANS experiments on the different proteins, since this approach is particularly adapted to investigate global conformational changes of macromolecules in solution [41, 43, 44].

SANS data highlight the conformational states of BmrA WT and mutants. The SANS signals of WT BmrA, E504Q and K380A mutants at ~ 2 mg.mL^{-1} were recorded in the absence or presence of ligands, in conditions where the Lauryl Maltose Neopentyl Glycol (LMNG) detergent was invisible to neutrons, i.e. 21.4% D_2O, the contrast match point previously determined for this detergent [32]. BmrA proteins were partially deuterated by over-expression in a deuterated minimal media containing 85% D_2O and unlabeled glycerol as carbon source, to provide sufficient contrast with the partially deuterated buffer. A deuteration level of 67-72% of non-labile hydrogens was estimated for the three purified proteins by MALDI TOF (Table S1). The resulting SANS data therefore reveal the shape of the proteins only, while detergent molecules bound to the proteins remain invisible. Full details on SANS samples, measurements and analysis are given in Table S2.

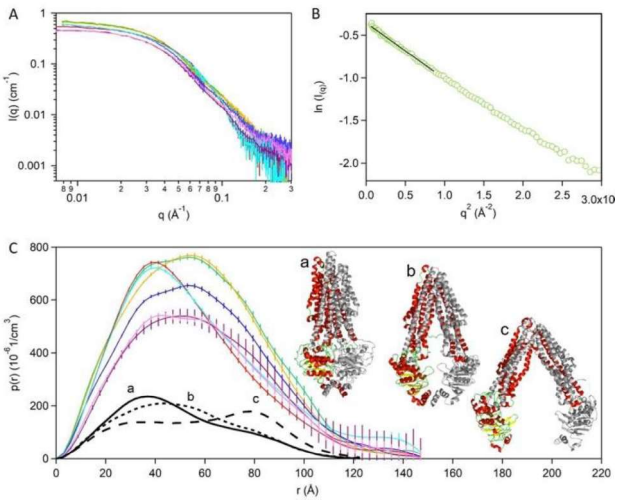

Figure 3. SANS data analysis. A: SANS scattering curves of WT BmrA in the apo state (green), or in the presence of ADP/Mg (yellow) and ATP/Mg/Vi (red), of the E504Q mutant in the apo state (blue) or in the presence of ATP/Mg (cyan), of the K380A mutant in the apo state (purple) or in the presence of ATP/Mg/Vi (pink). **B**: Example of Guinier fit for WT BmrA in the apo state. **C**: Pair distance distribution functions (p(r)) with the same color code as **A**. Note the p(r) are not normalized, the integral depends on sample concentration. Theoretical p(r) based on the PDB 6R81 structure of BmrA (continuous line, a), and on BmrA models built on PDB 3WME (dotted line, b) and 3B5W (discontinuous line, c) at 1 mg/mL. P(r) of BmrA homolog structures are given in Figure S1 for comparison. The error bars on the scattering data represent the uncertainty of each pixel (= sqrt counts / counts) propagated through the radial averaging.

At first glance, the flatness at low angle of all the raw scattering curves suggests the absence of aggregation (Figure 3**A**), as confirmed by the quality control experiments described below. The linearity of the Guinier plots (Figure 3**B**) is also consistent with sample homogeneity. From the Guinier plot, the radius of gyration, Rg, was obtained [43]. The Rgs are in the same range (44-45 Å) for the three proteins

in apo conditions, WT-ADP/Mg, and K380A-ATP/Mg/Vi, but are significantly lower (40 - 42.5 Å) for WT-ATP/Mg/Vi and E504Q-ATP/Mg (Table 1).

BmrA proteins	WT			E504Q		K380A	
conditions	Apo	ADP/Mg	ATP/Mg/Vi	Apo	ATP/Mg	Apo	ATP/Mg/Vi
Rg (Å)	44.3 ± 0.2	43.8 ± 0.3	40.3 ± 0.3	45.0 ± 0.3	42.5 ± 0.4	45.5 ± 0.5	44.3 ± 0.4
Max in p(r) (Å)	(41); 53	53	38	(40); 53	41	50	41; (59)

Table 1. Guinier and pair distribution analysis of BmrA samples in SANS. The precision for the p(r) maxima is ~ 2 Å. Values in parenthesis for the p(r) maxima indicate the position of shoulders.

For the K380A mutant with ATP/Mg, two samples were analyzed either in the presence or absence of vanadate. In view of the precision of the data, K380A-ATP/Mg and K380A-ATP/Mg/Vi had the same scattering curves (Figure S2), consistent with the lack of vanadate effect in the thermal stability assay (Figure 1) and the fact that this mutant was shown to be devoid of ATPase activity [35]. Due to a higher protein concentration, signal intensities were higher for the K380A-ATP/Mg/Vi experiment, and this condition was further processed.

Conditions where interactions between proteins are negligible (i.e. sample exempt of aggregates) are required to extract accurate information on protein structure from SANS data analysis. Sample quality was therefore checked after SANS measurement by analytical ultracentrifugation (AUC) or size exclusion chromatography coupled to light scattering (SEC-LS), showing >97-98% homogeneity (Figure S3) even after a couple of days of storage or freeze/thawing cycles, except for the E504Q mutant that displayed only 92% homogeneity. The corrected sedimentation coefficient, s_{20w} = 8.4 +/- 0.15 S, for WT BmrA in LMNG is in line with the 8.2 and 8.4 S values previously obtained for (hydrogenated) BmrA in LMNG [32] and Dodecyl-β-D-maltoside (DDM) [45], respectively. The molar masses of LMNG-BmrA complexes, derived from SEC-LS using a mean value between detergent and protein for the refractive index increment, are similar to the 240 kDa value found for hydrogenated BmrA [32] (Table S1). Melting temperatures of partially deuterated WT and E504Q BmrA, measured after SANS and AUC were 46.7 and 45.2 °C, respectively, comparable to that of the hydrogenated proteins (Figure 1). The specific activity for WT BmrA samples after SANS was ~ 0.9 µmol ATP hydrolyzed min^{-1} mg^{-1} protein, and it was inhibited at 98% by 200 µM Vi. In addition, the sample incubated in the presence

of ATP/Mg/Vi was still inhibited by ~ 88% after the SANS measurement, showing that the trapping of ADP/Mg/Vi was largely preserved throughout the experiment. Taken together, these features reveal that WT BmrA remains essentially either in an active or inhibited state during SANS data acquisition, depending on the ligands used for incubation, and that SANS data could be further processed.

The Fourier transform of the scattering data, p(r), results in the pair distance distribution functions and informs on the general shape of the molecule. The largest inter-atomic distance within the macromolecule, D_{max}, is determined as the large distance at which p(r) tends to be null. A globular compact protein will present a bell-shape p(r) with a well-defined maximum around $D_{max}/2$, whereas the presence of shoulders or asymmetric p(r) are indicative of multi-domain or elongated shapes [43]. The p(r) analysis of various BmrA samples clearly reveals different conformations (Figure 3**C**, Table 1). WT-ATP/Mg/Vi (red curve) and E504Q-ATP/Mg (cyan curve) display very similar p(r), with a maximum at ~ 40 Å, and very different from all other curves. This profile reflects smaller inter-atomic distances, which is compatible with an expected OF conformation. All the other samples show broader p(r) distributions, with the appearance of another maximum at ~ 53 Å, compatible with a non-compact shape, presumably an open IF conformation. The p(r) of WT-Apo and E504Q-Apo (green and blue curves, respectively) are indistinguishable in the relevant distance range. The p(r) of WT-ADP/Mg (yellow) is significantly different from that of WT-Apo, with a disappearance of the maximum at ~ 40 Å, leading to a distribution centered towards higher values. This suggests that the WT in the ADP/Mg bound state adopts, on average, a more open IF conformation than the apo state. In the presence of ATP/Mg/Vi, the K380A mutant (pink), which binds ATP but does not hydrolyze it [35], is much more open than WT-ATP/Mg/Vi (red) and E504Q-ATP/Mg (cyan), but appears to reside in an IF conformation, on average, more closed than in the apo state (purple). Because of low intensity features at large r (> 120 Å) in the E504Q mutant in the presence of ATP/Mg, possibly related to residual amounts of aggregates, it was not considered further for modelling. Apart from this, the quality of SANS data from all other samples were similar to the WT ones. The analyses in terms of conformations were thus performed on five sets of data from WT BmrA (apo, ATP/Mg/Vi and ADP/Mg) and K380A mutant (apo and ATP/Mg/Vi), as the E504Q mutant in its apo state was similar to that of the WT. The theoretical

p(r) derived from a high resolution structure of BmrA in the OF state (PDB 6R81; E504A BmrA mutant solved by cryo-EM;[42]), and from two models of the apo state of BmrA, are shown for comparison (Figure 3**C**, black curves); the latter are based on IF and wide-open IF (woIF) conformations of P-gp (PDB 3WME; [46]) and MsbA (PDB 3B5W, [17]), respectively. The p(r) of the OF structure, with a maximum at 37 Å is very similar to that of WT-ATP/Mg/Vi and E504Q-ATP/Mg. The maxima of the p(r) of the IF and woIF models are 44 and 77 Å, respectively. Because our experimental curves cannot be fitted satisfactorily with a single theoretical simulation, especially that with the largest opening between the two NBDs, BmrA presumably adopts an alternative conformation or an ensemble of different conformations.

The 3D shape derived from SANS data for the WT-ATP/Mg/Vi fits well the OF 3D structure. *Ab-initio* reconstruction of the 3D shape of a protein from its scattering curve is not trivial as different shapes can lead to the same curve, but the 3D structure of BmrA or homology models can help to narrow down the possibilities. The WT SANS curves were analyzed for their degree of ambiguity by the application "Ambimeter" to estimate whether they relate to a unique structure, or to several structures having a similar scattering signal [47]. Data from all samples were possibly ambiguous, except for WT-ATP/Mg/Vi (Table S2). An *ab*-initio reconstruction was therefore applied only to this data set. The resulting envelope, obtained by the program DAMMIN [48], is shown in Figure S4. It is superimposed with, and fits reasonably well, the 3D structure of the E504A BmrA mutant in an ATP-bound form (i.e. OF structure with closed NBDs; [42]). Some extra densities in the SANS envelope are, however, observed.

Multi-conformation fitting reveals BmrA flexibility in IF conformations and the absence of a woIF conformation. Because the ab-initio reconstruction of the other datasets (WT-Apo, WT-ADP/Mg, K380A-Apo and K380A-ATP/Mg/Vi) could not be reliably performed, we used instead another strategy to fit multiple conformations. The 3 models presented in Figure 3**C** were submitted to MULTIFOXS software to fit the data by adjusting the proportion of each of these 3 conformations [49]. However, no combination of the three models could fit satisfactorily the SANS data ($\chi^2 >> 1$). Thus, to address the possibility of protein flexibility in solution including intermediate openings of the NBDs, a large number

of additional conformations were generated *in silico.* A total of 7006 conformations, built as described in Figure S5 and in the method section, were used to fit the SANS data with MULTIFOXS, either individually or as ensemble of two, three and four conformations with variable proportions. Following this principle, all data sets could be reasonably well fitted ($\chi^2 \sim 1$) by an equilibrium between two main conformations. Figure 4 (panels **A** to **E**) shows a representative conformational set together with data fit.

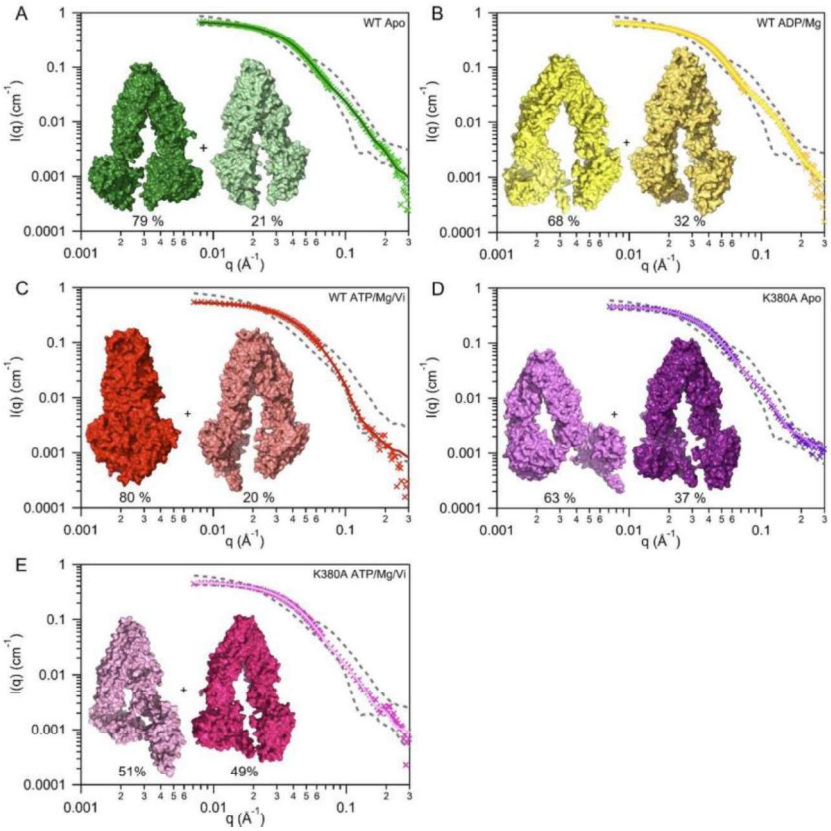

Figure 4. Multi-conformation fits of SANS data using Multifoxs. Each graph shows the best fit of SANS data with two conformations of WT-apo (**A**), WT-ADP/Mg (**B**), WT-ATP/Mg/Vi (**C**), K380A-apo (**D**) and K380A-ATP/Mg/Vi (**E**), together with the two modelled conformations combined to obtain the fit, and their relative proportion. Other conformation pairs fitting equally well the data are presented in figure S6. After the fitting process, the His-tag has been removed from the picture for clarity. On each fit, the grey dash lines show, for each Q-value, the minimum and maximum intensities from the calculated curves of the 7006 possible conformations.

However, several pairs of conformations fit the data equally well (similar χ^2) and they are presented in supplementary information (Figure S6). To estimate the degree of opening/closure between the two TMDs of BmrA homodimer, we measured distances between E212 residues in each monomer (Figure S6). This residue is located at the apex of ICD2 that links transmembrane helices 4 and 5, and is equivalent to G201 (TM287) and G225 (TM288) that were used earlier to visualize the opening between NBDs in different 3D structures of ABC exporters [10]. As a comparison, the distance between these residues in the woIF and IF models and in the OF structure is 62.2, 31.7 and 15.6 Å, respectively. None

of the fits obtained with MULTIFOXS was consistent with the largest distance of the woIF model, as the widest opening found in the case of WT-ADP/Mg was 54.8 Å for about half of the population, while the other half shows an opening of 29.5 Å (Figure S6). The other best fit for this condition gave similar values of opening of 51.5 and 29.5 Å in different proportions, 68 and 32%, respectively. All the other values for the opening between the TMD dropped to less than 42.2 Å. For WT-apo, 39.6 Å was the largest opening estimated for one conformation while the other one fluctuated between 39.3 Å (the most populated one in all fits) and 29.5 Å. Not surprisingly, WT-ATP/Mg/Vi leading to the trapping of ADP/Mg/Vi was the only condition where an OF conformation was found (distance of 15.2 Å) in a large proportion in the two fits (~ 80 %). Yet, a significant proportion of IF conformation appears to remain in this condition (distance of 36.6 Å), in agreement with the inability to properly fit the data with a unique OF conformation ($\chi^2 = 2.8$). This is presumably related to the regain in ATPase activity (~ 12%) reported above for the WT-ATP/Mg/Vi incubated sample after the SANS experiment. The K380A mutant in the apo state adopts different IF conformations similar to those seen in the WT BmrA regarding the opening of the TMD, but additional flexibility/reorientation of the NBDs with respect to the TMD could possibly occur as suggested by MULTIFOXS fitting (Figure 4**D**). This mutant appears unable to reach an OF conformation with a closed NBD state: in the presence of ATP/Mg ± Vi, it always remained in IF conformations with TMD separation varying between 39.3 and 31.6 Å.

HDX-MS supports the existence of multiple IF conformations for WT BmrA in the apo state. For an in-depth comparison of apo and ATP/Mg ± Vi bound states, HDX-MS was performed on WT and K380A mutant. Sequence coverages of ~ 70% were achieved allowing us to get precise information about local conformational changes occurring at the level of NBDs and ICDs during the catalytic cycle (Figure S7). WT-apo shows an overall high deuterium uptake especially in Walker A and B motifs, the D-loop, the C-terminus, and ICD1 and ICD2 (Figure 5**A**).

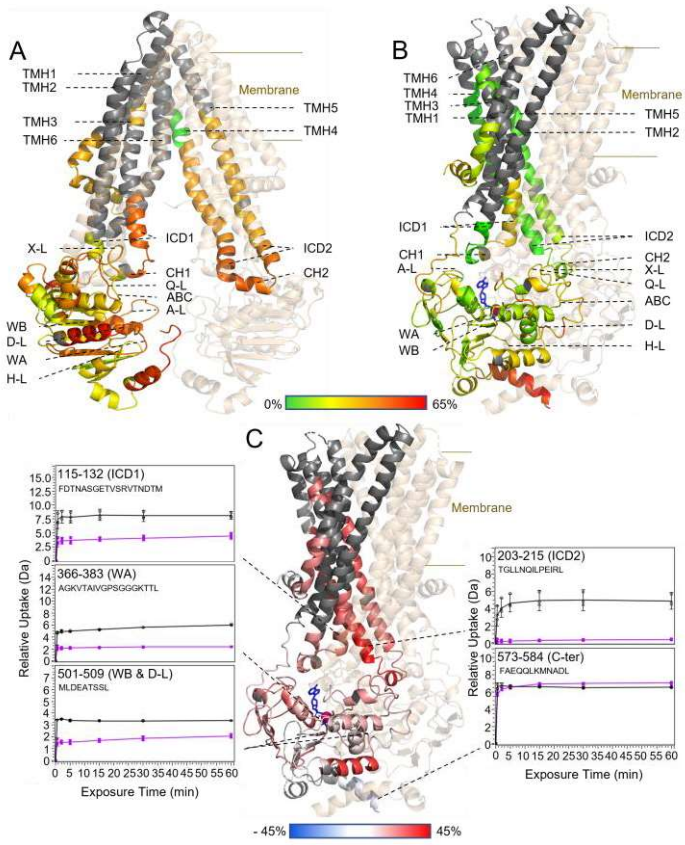

Figure 5. HDX-MS shows that WT BmrA is highly flexible in the apo state, as opposed to the vanadate-inhibited state. Deuterium exchange after 1-h of deuteration, plotted on **A**: apo form, the inward-facing model of BmrA (based on PDB 3WME) and **B**: ATP/Mg/Vi incubated form, the outward-facing structure (PDB 6R81). One monomer is colored according to a green (0%) to red (65%) scale. One ATP molecule is in blue, and Mg^{2+} in magenta. **C**: Differential deuterium uptake, between apo and ATP/Mg/Vi incubated forms, mapped on the OF structure, from -45% to 45% scale with blue: less deuteration, white: no difference, red: more deuteration uptake, in the apo form. In grey, peptides that were not identified. The box inserts show the relative deuterium uptake (Da) in apo (black) and ATP/Mg/Vi bound states (magenta) of selected peptides, with error bars showing the standard deviations between triplicates with sigma multiplier 2. A-L, Q-L, X-L, ABC, D-L and H-L, correspond to A-loop, Q-loop, X-loop, ABC motif, D-loop and H-loop, respectively; C-ter, C-terminal; CH, coupling helix; ICD, intracellular domain; TMH1-6, transmembrane helices 1-6; WA and WB Walker-A and -B motifs.

The only peptide that was completely shielded from exchange, even after 1 h of deuteration, lies in the transmembrane helix 4, presumably surrounded by the detergent belt. The high exchange observed in the ICDs, especially ICD2, implies a high flexibility of these subdomains in LMNG, which is congruent with the high deuterium exchange found in this region when BmrA was studied in a DDM solubilized form [33]. In addition, isotopic envelopes for most of the peptides from ICD2 are observed to be widespread and/or bimodal (e.g. peptide 180-215, Figure S8**A**), typical of EX1 regimes [50] whereby H-bond breathing events are much slower than the rate of proton/deuterium exchange and suggesting the presence of several co-existing conformations. In contrast, in the ATP/Mg/Vi-trapped state, WT BmrA shows a large overall protection against deuteration (Figure 5**B** & S7**A**), in agreement with the compact 3D-structure of the OF conformation. Only the solvent accessible and possibly unstructured C-terminal peptide exchanges very quickly with deuterium. Figure 5**C** shows peptides (in red) with higher

deuterium uptakes in the apo state compared to the WT-ATP/Mg/Vi state. Significant shielding is observed in all NBD conserved sequences involved in ATP/Mg binding, including Walker A- and B-motifs, the A-, C-, and D-loops (Figure S7**A**). The X- and the Q-loops, potentially involved in the NBD-TMD communication, are also protected. We observe a prominent decrease in deuteration of the ICDs, which connects the NBD and TMD, most likely linked to an increased structuration in the WT-ATP/Mg/Vi state. Globally, the large change in deuterium uptake between these two conditions confirms the major conformational change between the apo and ATP/Mg/Vi states. In addition, the presence of bimodal deuteration patterns in the apo state reveals the presence of co-existing conformations as also observed by SANS.

HDX-MS discloses the inability of the K380A mutant to reach the OF conformation. Given the lack of effect of vanadate with this mutant, only the effect of ATP/Mg was studied here. The overall high deuteration observed in the apo condition is comparable to that observed for the WT (Figure 6**A**).

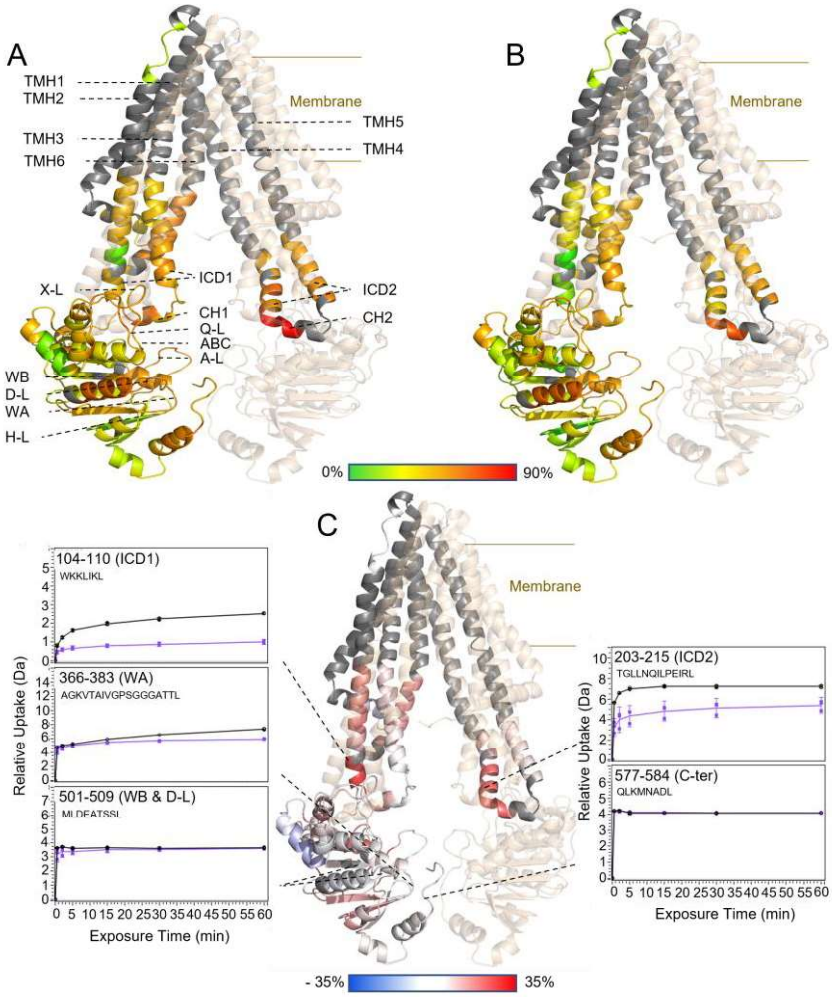

Figure 6. HDX-MS of K380A BmrA reveals its inability to reach an OF conformation in the presence of ATP. Deuterium exchange after 1 h of deuteration, plotted on the inward-facing model of BmrA (based on PDB 3WME) for **A**: apo form, and **B**: ATP/Mg bound form. One monomer is colored according to a green (0%) to red (90%) scale. **C**: Differential deuterium uptake, between apo and ATP/Mg bound forms, from -35% to 35% scale with blue: less deuteration, white: no difference, red: more deuteration, in the apo form. In grey, peptides that were not identified. The box inserts show, in Da, the relative deuterium uptake in apo (black) and ATP-bound forms (purple), of selected peptides, with error bars showing the standard deviations between triplicates with sigma multiplier 2. Abbreviations are the same as on Figure 5.

A striking difference is observed, however, for the ATP/Mg bound state. Here, a very limited protection against deuteration was detected for most peptides in the K380A mutant, ruling out the possibility of a large conformational change when the transporter binds ATP (Figures 6**B** & S7**B**). Interestingly, at shorter deuteration times, a limited but significant protection could be observed in conserved sequences involved in ATP/Mg binding, namely Walker A and B motifs, corroborating the binding of ATP by this mutant (Figure 6**C** box inserts and S7**B**). The most prominent effect afforded by ATP/Mg binding was seen at the level of ICDs, especially ICD2, where a clear reduced deuteration was observed (Figure 6**C**). This suggests that ATP binding to isolated NBDs in IF conformation stabilizes the structure of the ICDs

in the K380A mutant, while this mutation precludes the NBD dimerization and thereby the transition to the OF state.

Discussion

The power of SANS to highlight conformational changes has been illustrated with MsbA in nanodiscs where subtle differences between ADP and ADP/Vi conformations were reported [51]. This approach is, however, limited so far to nanodiscs formed exclusively from phosphatidylcholine as deuterated lipids need to be used to mask their contribution in scattering experiments [52]. For MsbA, this constraint did not seem to have any adverse effect as phosphatidylcholine allowed to regain a significant level of ATPase activity as compared to the detergent-purified transporter [51]. Yet, single molecule FRET showed that MsbA cannot readily switch between woIF and OF conformations in nanodiscs, in contrast to detergent or proteoliposomes states [26], suggesting that the former environment can somehow impede the overall motion of MsbA. Furthermore, a similar variation in distance between spin labels was shown by EPR spectroscopy for the transition of MsbA from IF to OF conformations both in detergent and in liposomes, indicating that the detergent state can be appropriate to study the ATPase cycle of some ABC transporters [53, 54]. For BmrA, the use of LMNG as a solubilizing agent maintains the transporter in a stable highly-active state (~ 1.4 μmol ATP hydrolyzed/min/mg) so this detergent appears suitable to recapitulate the ATPase cycle of BmrA [31, 32, 55].

SANS experiments reported here suggest that in the resting state BmrA has mostly two different IF conformations with, on average, a moderate opening between its two NBDs. This opening seems to be consistent with IF structures of P-gp (i.e. from mouse or *C. merolae*; Figure S9), whose global shape has been recently confirmed by EPR spectroscopy [56]. In contrast, BmrA does not seem capable to adopt a woIF conformation such as those found with MsbA (e.g. EcMsbA or StMsbA), although they are both homodimers with a significant degree of homology (30.9% of identity plus 26.6% of strong similarity between *S. typhimurium* MsbA and BmrA). P-gp is a full-length ABC transporter with two pseudo-symmetric halves connected by a linker of ~ 70 amino acids, and it has been suggested that this linker could restrain the physical separation of the NBDs [15]. BmrA is a homodimer, but the absence

of a linker between its two halves does not seem to allow a wide opening in the resting state. Thus, a more likely explanation for the different degree of opening between the two moieties of ABC exporters possibly lies in the nature of the molecule transported [10]. MsbA is involved in the translocation of a large lipopolysaccharide, and because this molecule is entirely accommodated into a wide cavity within the transporter [57, 58], this might support the physiological relevance of a woIF conformation of MsbA to accommodate such a big substrate [16-18]. P-gp or BmrA, on the other hand, are dedicated to the efflux of toxic compounds whose size appears limited, i.e. < 1200 Da for most P-gp substrates [59]. Larger molecules such as the a-factor pheromone (~ 1600 Da) do not necessarily bind entirely within the P-gp cavity in order to be exported. The IF conformation found in P-gp is nevertheless capable to create a large internal cavity of ~ 6000 $Å^3$ [60, 61], that can potentially accommodate two drugs simultaneously [62-64], presumably due to an inherent flexibility in the apo state [20, 65].

The best fits of our SANS data show an intrinsic flexibility of BmrA in the resting state with possibly two main IF conformations. It should be noted that the SANS models were not subjected to energy minimization; they were mainly used to enlighten the overall conformation of the transporter in a given state, and in particular the distances between the two NBDs. The SANS data might as well be the result of a continuum of several discrete IF conformations but the fitting process would have been much more arduous to achieve, so we limited ourselves to two different conformations. Intrinsic flexibility in the resting state has also been observed for the homologous multidrug transporter LmrA by EPR spectroscopy [66]. In BmrA, this flexibility involves presumably some disengagement and/or rotation of the NBDs relative to the ICDs that might even be exacerbated in the K380A mutant. Considering the rigid body transition from IF to OF states that was anticipated from different 3D structures [17], these SANS results might seem at odds but they are actually supported by our HDX-MS data: a much higher accessibility of the ICDs to deuterium exchange is observed in the resting state as compared to the OF conformation stabilized by ADP/Mg/Vi. This is also congruent with our previous HDX-MS study using a catalytically inactive E504A mutant trapped in an ATP-bound state where its ICDs were quite protected from deuterium exchange in comparison to the WT BmrA in the apo state [33]. Such a protection from deuterium exchange was also reported with P-gp in the ATP-bound state [65]. Interestingly, a disengagement of NBD1 from ICD4 has been proposed to occur in the resting state

of CFTR to explain the nanobody accessibility of an epitope, which would be otherwise buried in the whole transporter if a static 3D structure was maintained throughout the catalytic cycle [67].

The results obtained with the K380A BmrA mutant underline its inability to reach the OF conformation upon ATP binding (Figure 7), as previously hypothesized from a low-resolution cryo-EM study of BmrA in unique ring structures [35].

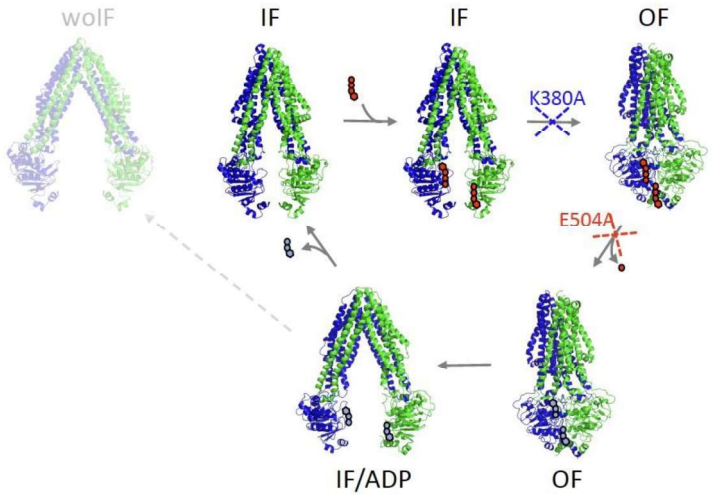

Figure 7. Scheme of the catalytic cycle of WT BmrA and the steps impaired by the two mutations. In the apo state, WT BmrA mainly adopts an IF conformation where the two NBDs are physically separated but the woIF is not, or marginally, populated by BmrA (dotted line for the ghost of the woIF conformation). Binding of ATP (hexagon tethered to three red circles) triggers the dimerization of the NBDs. In this OF conformation, ATPase activity will lead to Pi dissociation (red circle) that will return the transporter to an IF conformation. Based on the SANS results, this conformation (IF/ADP) is on average more open that the apo state. ADP (hexagon tethered to two light blue circles) dissociation resets BmrA in the apo state with a shortened distance between the NBDs. The steps impaired in the K380A and E504Q mutants are indicated on the scheme.

A similar conclusion was drawn from mutations of the equivalent lysine residues in the two NBDs of the P-gp [68] or, more recently, from a mutant in the A-loop of the first NBD of this transporter [69]. Also, a lack of ATP-dependent dimerization of the NBD of ComA was reported in the Walker-A K to A mutant [70]. ATP binding induces, however, a global effect on the conformation of the K380A mutant as revealed by limited proteolysis, thermal denaturation and SANS data. The major effect of ATP binding to this mutant observed by HDX-MS is the structuration of ICDs, and in particular ICD2, presumably mediated by its interaction with the NBD. At the NBD level, changes in local dynamics are visible but no drastic effect is seen on the deuteration rate for a large number of peptides, suggesting that the global conformation of the NBD is unchanged between the apo and ATP-bound states. This is consistent with the 3D structures of ABCB10 [71] or ABCB8 [72] in which the binding of an ATP analog to each NBD did not promote the NBD dimerization, so the transporters remained in an open IF

state; in these 3D structures, the global conformation of the NBD is essentially unaffected by nucleotide binding. This likely explains the weak direct protection observed for the NBD peptides in our HDX-MS experiment with the K380A mutant. Indeed, HDX-MS monitors the exchange of deuterium at the level of the backbone amide hydrogen [40] while nucleotide binding to single NBD involves essentially side-chain residues, except for the Walker-A motif [73]. A comparison of the access to the hydrogen atoms of the amide backbone of ABCB10 with and without nucleotide analog shows that the presence of the nucleotide does not induce any difference, even for the Walker-A motif (Table S3), thereby possibly explaining the lack of strong protection in HDX-MS with the K380A mutant.

Finally, a rather astounding result came from the SANS data suggesting that, on average, BmrA in the presence of ADP/Mg adopts a conformation significantly more open than in the resting state. This suggests that in this post-hydrolytic step, the ADP-Mg end-product induces some repulsion between the two NBDs, as originally proposed [74], but with a larger degree of opening than when the ATP-binding sites are empty. First, it is important to mention that this ADP-bound state is presumably identical to that obtained during the whole ATPase cycle because the same 3D structures were obtained for MalK subunits starting either from ATP/Mg (ending up with two ADP/Mg in the two catalytic sites) or by adding ADP/Mg in the crystallization medium [73]. MD simulations suggest that in contrast to ATP, ADP may lead to the destabilization of the NBD dimer [75, 76], supporting the fact that the OF state was not observed by Cryo-EM for P-gp in the presence of ADP [21]. MsbA, on the contrary, seems capable to reach the OF state to some extent, in the presence of ADP/Mg [15], and it is important to mention that the Sav1866 3D structure was solved in an OF conformation with bound ADP/Mg [77]. Interestingly, two 3D structures of MalK were solved in the resting state, open and semi-open, with different inter-subunit separations [78], while the ADP/Mg-bound structure falls in between these two forms [73]. Here, our results support the contention that BmrA in the apo state remains mostly in two main IF conformations with a moderate opening between its NBDs, whereas ADP/Mg may increase the inter-NBD separation (Figure 7, IF vs IF/ADP). This is also corroborated by a cryo-EM study on human P-gp showing that in the resting state, the transporter fluctuates between IF and OF conformations while addition of ADP keeps the transporter in IF conformations [21]. Because this latter study was performed in the presence of a specific monoclonal antibody, it might have affected the equilibrium between the

IF and OF conformation, and a strong preference for an IF conformation was reported by thermal unfolding of the mouse P-gp in the apo state [79]. Here, our results with BmrA were obtained with the native protein so they clearly support a wider opening of the two NBDs in the post-hydrolytic state as compared to the resting state. This property might be a common trend of symmetrical ABC exporters that has a major implication for their catalytic mechanism. Indeed, the post-hydrolytic ADP-bound state is a required step that precedes the release of ADP from the NBDs, and the subsequent binding of two ATP to engage in a next transport cycle. Because BmrA and the P-gp are in an IF conformation with the two NBDs physically separated in this ADP-bound state, this conformation is therefore relevant for their functioning mechanism. Moreover, it has been argued that the ATP concentration in the cells is far in excess of the K_M value for P-gp, so this transporter will always be saturated by ATP. This is clearly not the case for many micro-organisms which constantly have to face adverse conditions and the ATP concentration might become quite low [80]. In such instances, the IF open state will be physiologically relevant. In fact, the lifetime of this open IF conformation will be primarily dictated by the rate of release of ADP from the NBDs and the subsequent rate of ATP binding.

In conclusion, by using a combination of SANS and HDX-MS, our results uncover the main steps of the catalytic cycle of a homodimeric multidrug ABC transporter and highlight the importance of the ADP-bound IF conformation adopted during the post-hydrolytic step of a transporter from the type IV subfamily.

Acknowledgments

This work was supported by the Agence Nationale de la Recherche (ANR), grants ANR-14-CE09-0024B (JMJ), ANR-19-CE11-0023-01 (CO), and ANR-16-CE92-0001 (CE and CB). It was partially supported by the IDEX-IRS project Pepsi-SAS “Small-angle scattering using polynomial expansions” funded by Univ. Grenoble Alpes. We thank Sergei Grudinin (INRIA Grenoble FR) and Dina Schneidman-Duhovny (Weizmann Institute, Rehovot, IL) for computing support, and Luca Signor (IBS Grenoble FR) who performed the MALDI-TOF-MS analysis. This work used the platforms of the Grenoble Instruct-ERIC center (ISBG; UMS 3518 CNRS-CEA-UGA-EMBL) within the Grenoble

Partnership for Structural Biology (PSB), supported by FRISBI (ANR-10-INBS-05-02) and GRAL, financed within the University Grenoble Alpes graduate school (Ecoles Universitaires de Recherche) CBH-EUR-GS (ANR-17-EURE-0003). IBS acknowledges integration into the Interdisciplinary Research Institute of Grenoble (IRIG, CEA). Waqas Javed benefitted from a doctoral fellowship by the Higher Education Commission of Pakistan as well as a grant from ILL for his fourth year of PhD. This work benefited from the use of the SasView application, originally developed under NSF award DMR-0520547. SasView contains code developed with funding from the European Union's Horizon 2020 research and innovation program under the SINE2020 project, grant agreement No 654000. HDX-MS were supported by the French Ministry of Research (Investissements d'Avenir Program, Proteomics French Infrastructure, ANR-10-INBS-08 to O. B-S) and the Région Midi-Pyrénées (O. B-S). We also thank Dr. Khadija Mathieu for her input in BmrA model based on 3WME made using MODELLER.

Author Contributions

Conceptualization, C.O., C.B., C.E., A.M and. J.-M.J.; Investigation, W.J, C.O., S.V., M.-P.C., A.L.R., M.M., M.H., C.B., J.M., C.E., and A.M.; Original Draft of the MS, J.-M.J. with input from W.J, C.E., and A.M.; Review & Editing, W.J., C.O., J.M., C.E., A.M and J.-M.J.; Supervision, C.O., M.H., J.M., C.E., J.-M.J., and A.M.; Funding Acquisition, O. B-S, C.O., C.E., C.B., A.M. and J.-M.J.

Declaration of Interests

The authors declare no competing interests.

ORCID: Cécile Breyton : 0000-0002-4382-0434 ; Christine EBEL : 0000-0002-6912-500X; Julien Marcoux: 0000-0001-7321-7436; Cédric Orelle: 0000-0003-3418-3290; Anne Martel : 0000-0002-1232-8519; Waqas Javed: 0000-0002-3381-4794; Jean-Michel Jault : 0000-0003-1743-2777

Figure Titles and Legends only

Figure 1. Thermal stability of WT BmrA and mutants and effect of nucleotides. Ratio of fluorescence emitted at 350 and 330 nm and first-derivatives with T_m (upper and lower sub-panels, respectively) for **A**: WT, wild-type BmrA. **B**: E504Q mutant and **C**: K380A mutant. Unless otherwise specified, ADP or ATP were added at 10 mM in the presence of 10 mM $MgCl_2$; When 2 mM ATP was used, 3 mM $MgCl_2$ were added; Vi was added at 1 mM. These experiments were reproduced at least three times from two different batches of purified proteins and with triplicate each time; a representative experiment is shown here.

Figure 2. Limited proteolysis of K380A and E504Q mutants compared to WT BmrA. After incubation with the indicated ligands, BmrA WT (**A**-**B**), E504Q (**C**-**E**), or K380A mutants (**F**-**I**) were treated with trypsin for various times. $MgCl_2$ was added at 3 or 10 mM when 2 or 10 mM nucleotides were used, respectively. Vi was added at 1 mM. All samples were in 0.01% LMNG. Time zero was taken just before adding trypsin and the proteins were resolved using a 12% SDS PAGE. The arrows indicate the position of intact BmrA. Red boxes highlight the bands after 60 min of digestion. These experiments were reproduced at least three times from at least two different batches of purified proteins and a representative experiment is shown here.

Figure 3. SANS data analysis. A: SANS scattering curves of WT BmrA in the apo state (green), or in the presence of ADP/Mg (yellow) and ATP/Mg/Vi (red), of the E504Q mutant in the apo state (blue) or in the presence of ATP/Mg (cyan), of the K380A mutant in the apo state (purple) or in the presence of ATP/Mg/Vi (pink). **B**: Example of Guinier fit for WT BmrA in the apo state. **C**: Pair distance distribution functions (p(r)) with the same color code as **A**. Note the p(r) are not normalized, the integral depends on sample concentration. Theoretical p(r) based on the PDB 6R81 structure of BmrA (continuous line, a), and on BmrA models built on PDB 3WME (dotted line, b) and 3B5W (discontinuous line, c) at 1 mg/mL. P(r) of BmrA homolog structures are given in Figure S1 for comparison. The error bars on the scattering data represent the uncertainty of each pixel (= sqrt counts / counts) propagated through the radial averaging.

Figure 4. Multi-conformation fits of SANS data using Multifoxs. Each graph shows the best fit of SANS data with two conformations of WT-apo (**A**), WT-ADP/Mg (**B**), WT-ATP/Mg/Vi (**C**), K380A-apo (**D**) and K380A-ATP/Mg/Vi (**E**), together with the two modelled conformations combined to obtain the fit, and their relative proportion. Other conformation pairs fitting equally well the data are presented in figure S6. After the fitting process, the His-tag has been removed from the picture for clarity. On each fit, the grey dash lines show, for each Q-value, the minimum and maximum intensities from the calculated curves of the 7006 possible conformations.

Figure 5. HDX-MS shows that WT BmrA is highly flexible in the apo state, as opposed to the vanadate-inhibited state. Deuterium exchange after 1-h of deuteration, plotted on **A**: apo form, the inward-facing model of BmrA (based on PDB 3WME) and **B**: ATP/Mg/Vi incubated form, the outward-facing structure (PDB 6R81). One monomer is colored according to a green (0%) to red (65%) scale. One ATP molecule is in blue, and Mg^{2+} in magenta. **C**: Differential deuterium uptake, between apo and ATP/Mg/Vi incubated forms, mapped on the OF structure, from -45% to 45% scale with blue: less deuteration, white: no difference, red: more deuteration uptake, in the apo form. In grey, peptides that were not identified. The box inserts show the relative deuterium uptake (Da) in apo (black) and ATP/Mg/Vi bound states (magenta) of selected peptides, with error bars showing the standard deviations between triplicates with sigma multiplier 2. A-L, Q-L, X-L, ABC, D-L and H-L, correspond to A-loop, Q-loop, X-loop, ABC motif, D-loop and H-loop, respectively; C-ter, C-terminal; CH, coupling helix; ICD, intracellular domain; TMH1-6, transmembrane helices 1-6; WA and WB Walker-A and -B motifs.

Figure 6. HDX-MS of K380A BmrA reveals its inability to reach an OF conformation in the presence of ATP. Deuterium exchange after 1 h of deuteration, plotted on the inward-facing model of BmrA (based on PDB 3WME) for **A**: apo form, and **B**: ATP/Mg bound form. One monomer is colored according to a green (0%) to red (90%) scale. **C**: Differential deuterium uptake, between apo and ATP/Mg bound forms, from -35% to 35% scale with blue: less deuteration, white: no difference, red: more deuteration, in the apo form. In grey, peptides that were not identified. The box inserts show, in Da, the relative deuterium uptake in apo (black) and ATP-bound forms (purple), of selected peptides,

with error bars showing the standard deviations between triplicates with sigma multiplier 2. Abbreviations are the same as on Figure 5.

Figure 7. Scheme of the catalytic cycle of WT BmrA and the steps impaired by the two mutations. In the apo state, WT BmrA mainly adopts an IF conformation where the two NBDs are physically separated but the woIF is not, or very marginally, populated by BmrA (dotted line for the ghost of the woIF conformation). Binding of ATP (hexagon tethered to three red circles) triggers the dimerization of the NBDs. In this OF conformation, ATPase activity will lead to Pi dissociation (red circle) that will return the transporter to an IF conformation. Based on the SANS results, this conformation (IF/ADP) is on average more open that the apo state. ADP (hexagon tethered to two light blue circles) dissociation resets BmrA in the apo state with a shortened distance between the NBDs. The steps impaired in the K380A and E504Q mutants are indicated on the scheme.

Tables with Titles and Legends

BmrA proteins	WT			E504Q		K380A	
conditions	Apo	ADP/Mg	ATP/Mg/Vi	Apo	ATP/Mg	Apo	ATP/Mg/Vi
Rg (Å)	44.3 ± 0.2	43.8 ± 0.3	40.3 ± 0.3	45.0 ± 0.3	42.5 ± 0.4	45.5 ± 0.5	44.3 ± 0.4
Max in p(r) (Å)	(41); 53	53	38	(40); 53	41	50	41; (59)

Table 1. Guinier and pair distribution analysis of BmrA samples in SANS. The precision for the p(r) maxima is ~ 2 Å. Values in parenthesis for the p(r) maxima indicate the position of shoulders.

MATERIELS AND METHODS

RESOURCE AVAILABILITY

Lead Contact *:*further information and requests for resources and reagents should be directed to and will be fulfilled by the Lead Contact, Jean-Michel Jault (jean-michel.jault@ibcp.fr).

Data and Code Availability Statement*:* The [datasets/code] generated during this study are available at [name of repository] [accession code/web link].

- SANS Data: doi.ill.fr/10.5291/ILL-DATA.BAG-8-36; doi.ill.fr/10.5291/ILL-DATA.BAG-8-37. SANS curves for the analyzed samples are provided in Table S2.
- The HDX-MS data has been deposited to the ProteomeXchange Consortium via the PRIDE partner repository [81] with the dataset identifier PXD028663.
- The quality control data for AUC, SEC-LS, and MALDI-TOF, have not been deposited in a public repository but are available from the corresponding author on request.

METHOD DETAILS

BmrA sample names: WT-Apo: WT without ligand; WT-ADP/Mg: WT + 10 mM ADP + 10 mM $MgCl_2$; WT-ATP/Mg/Vi: WT + 10 mM ATP + 10 mM $MgCl_2$ + 1 mM Vi; E504Q-Apo: E504Q without ligand; E504Q-ATP/Mg: E504Q + 10 mM ATP + 10 mM $MgCl_2$; K380A-Apo: K380A without ligand; K380A-ATP/Mg/Vi: K380A + 10 mM ATP + 10 mM $MgCl_2$ + 1 mM Vi.

Buffers: Buffer A : 50 mM Tris-HCl pH 8, 10% glycerol, 100 mM NaCl, 20 mM imidazole and 0.01% LMNG. Dialysis buffer : 50 mM Hepes-KOH pH 8, 10% glycerol, 50 mM NaCl and 0.01 % LMNG. SANS buffer: 50 mM Tris-HCl pH 8, 150 mM NaCl, 10% Glycerol, 0.01% LMNG and 21.4% D_2O.

Cloning and expression of deuterated BmrA : the plamids for hydrogenated BmrA expression are: *pET23-WT bmrA* [29]; *pET23-E504Q bmrA* [39]; *pET23-K380A bmrA* [35]. For the production of deuterated BmrA requiring kanamycin resistance, the following constructs were designed. Construction of *pET28-WT bmrA*: *bmrA* gene fragment was PCR-amplified from *pET23-WT bmrA* with the primers

TataccatggcaCCAACCAAGAAACAAAAATCTAAAAGTAAATTGAA and *CTTGTCGACCCCGGCTTT*. *WT bmrA* was cloned in *pET28* by using the NcoI and SalI restriction sites. Construction of *pET28-E504Q bmrA*: The plasmid *pET28-bmrA* was digested with SalI and PstI for 3 hours at 37 °C. After electrophoresis, the 6436 bp fragment was extracted from the agarose gel. The plasmid *pET23-E504Q bmrA* was similarly digested with SalI and PstI and the 587 bp fragment was extracted. Next, a ligation with the two fragments was performed with T4 DNA ligase for 4 h at room temperature, before transformation of TOP10 cells. Construction of *pET28-K380A bmrA*: The plasmids *pET23-K380A bmrA* and *pET28-WT bmrA* were digested with StuI and SacII restriction enzymes for 1 h at 37 °C. After electrophoresis, the smaller fragment corresponding to *K380A bmrA* from *pET23* and the bigger fragment lacking *WT bmrA* from *pET28* were extracted from the agarose gel. Next, a ligation with the two fragments was performed with T4 DNA ligase for 1 h at room temperature, before transformation of TOP10 cells. The amino acid sequences of BmrA in *pET28* are given in Table S2.

Preparation of deuterated BmrA bacterial paste: expression of partially deuterated ("match-out labeled") BmrA (d-BmrA) for neutron scattering was carried out by the ILL Deuteration Laboratory (D-Lab) at the Institut Laue-Langevin (ILL), Grenoble, France, according to previously established protocols [82, 83]. After adaptation to growth in deuterated minimal medium, C41(DE3) cells containing the expression vector *pET28a* with the coding sequence for wild-type or mutant BmrA (K380A or E504Q) inserted, were grown in a high-cell density fermenter culture at 30 °C. The deuterated minimal medium contained 85% (v/v) D_2O and unlabeled glycerol as carbon source. During the batch and fed-batch phases, the pD was adjusted to 6.9 by addition of NaOD (Eurisotop, France). The culture was induced with 0.5 mM IPTG at an OD_{600} of around 13 and deuterated cells (about 50 g wet weight from 1-2 L of fermenter culture) were harvested after overnight expression and stored at -80 °C.

Inverted Membrane Vesicles (IMVs) preparation: the preparation of IMVs for the hydrogenated proteins was typically done as detailed in [31]. Briefly, bacterial pellet was resuspended, cellular debris was removed by centrifugation after cell lysis, membrane fraction was obtained by ultracentrifugation, twice, and resuspended in 20 mM Tris-HCl pH 8, 300 mM sucrose, 1 mM EDTA; membranes were stored at -80 °C. The total protein concentration in membrane vesicles was analyzed by BCA assay. For

deuterated pellets, the differences were as follows: bacterial pellet was resuspended with, additionally, 1 mg/mL lysozyme; the bacterial cells were lysed by three 5 min cycles of sonication; membrane fraction was obtained by one ultracentrifugation only.

BmrA purification: BmrA enriched IMVs, at 2 mg/mL final membrane protein concentration, were solubilized for 1 h at 4 °C in 50 mM Tris-HCl pH 8, 10% glycerol, 100 mM NaCl, 1 mM dithiotreitol, 10 mM imidazole, protease inhibitor cocktail tablet (Roche) and 1% LMNG. The soluble fraction obtained after ultra-centrifugation, at 150,000 g for 1 h at 4 °C, was injected into a 1 mL HisTrap HP column (GE Healthcare), which was pre-equilibrated with buffer A. The column was washed first with 3-5 column volumes of 50 mM Tris-HCl pH 8, 10% glycerol, 500 mM NaCl, and 0.01% LMNG, and then with 20 column volumes of the buffer A. Gradient elution was then performed with the imidazole gradient from 20 to 500 mM. The protein fractions were dialyzed twice, overnight, and for 4 h the next day, at 4 °C against dialysis buffer. The protein concentration was determined from UV absorbance at 280 nm by using Nanodrop spectrophotometer, and a $\varepsilon 280nm=38,850\ M^{-1}\ cm^{-1}$. The protein concentration was further assayed with Bradford method. Protein was stored at -80 °C after flash freezing in liquid N_2.

Deuterated BmrA purification and SANS samples: SANS measurements were performed in two sessions, corresponding to two slightly different purification protocols. The initial steps of the two purifications were essentially as above, with the following modifications. The solubilization was done for 1.5 h at 4 °C in 100 mM sodium phosphate (Na-Pi) pH 8 (session 1) or 100 mM Tris-HCl pH 8 (session 2), 15% glycerol, 100 mM NaCl, 1 mM dithiotreitol, 10 mM imidazole and 1% LMNG. The 1 mL HisTrap HP column was pre-equilibrated with 50 mM Na-Pi pH 8 (session 1) or 50 mM Tris-HCl pH 8 (session 2), 15% glycerol, 100 mM NaCl, 20 mM imidazole and 0.01% LMNG. The column was washed with 20 column volumes of the same buffer before the imidazole gradient. Then, the most concentrated fractions were pooled, and dialysed overnight at 4 °C against either 50 mM Hepes pH 8 (session 1) or 50 mM Tris-HCl pH 8 (session 2), 10% glycerol, 50 mM NaCl, 0.01% LMNG, before flash freezing in liquid N_2. Next, protein was concentrated using 4 mL 100 kDa cutoff Millipore concentrator, and injected into a Superdex 200 10/300 GL SEC column equilibrated with SANS buffer,

at a flow rate of 0.25 mL/min. The most concentrated fractions were pooled, concentrated, and re-injected into the same column. The final samples were obtained by pooling the most concentrated fractions. They were, with or without ligands, filled in 1 mm quartz cuvette for SANS measurements. In session 2, where indicated, the ligands were added in the cuvette after acquisition of the data for the Apo form. The BmrA samples measured were, in session 1: WT-Apo (A_{280} = 1.64); WT-ADP (A_{280} = 1.59); WT-ATP/Vi (A_{280} = 1.55); E504Q-Apo (A_{280} = 1.395); E504Q-ATP (A_{280} = 1.35); and in session 2: WT-Apo (A_{280} = 0.55); WT-ATP/Vi (A_{280} = 0.54, and A_{280} = 1.21); K380A-Apo (A_{280} = 0.23, and A_{280} = 0.91); K380A-ATP (A_{280} = 0.22); K380A-ATP/Vi (A_{280} = 0.91).

ATPase activity assay: the activity assays of BmrA were done in a quartz cuvette in a final volume of 700 µL. The buffer, containing 50 mM Hepes-KOH pH 8, 10 mM $MgCl_2$, 4 mM phosphoenolpyruvate, 0.3 mM NADH, 32 µg/mL lactate dehydrogenase, 60 µg/mL pyruvate kinase, 10 mM ATP and 0.01% LMNG, was added into the cuvette and was allowed to attain the desired temperature, i.e. 37 °C for 5 min, before adding 3 µg protein (estimated from Bradford assays), and measuring the absorbance at 340 nm for 20 min at 37 °C.

MALDI TOF Mass spectrometry quality control: the experiments were done using an Autoflex Max mass spectrometer (Bruker Daltonics), after diluting the WT and E504Q BmrA SANS samples to typically 2.5 µM with sinapinic acid matrix (Sigma; 10 mg/ml in acetonitrile/water, 0.1% TFA (50:50)), and depositing 1 µL on the target. In the case of K380A, the sample was diluted 6 times in 5% formic acid, and analyzed according to [84]. From the measured masses of 68998, 69072, and 68830 Da, for WT, E504Q, and K380A BmrA, a deuteration level of 70, 72, and 67% was obtained, respectively, for the non-labile hydrogens (Table S1).

Limited proteolysis of BmrA: purified BmrA was diluted to 0.5 µg/µL in the dialysis buffer. After 15 min of incubation at room temperature, in the presence or abesnce of ligands as indicated below, trypsin (1 µg/25 µg of protein) was added. Samples of 10 µL (5 µg BmrA) were withdrawn at 0, 2, 5, 15, 30, 60, 120, 180 and 240 min. 2.5 µL of 5% trifluoroacetic acid was added immediately to each sample to stop the reaction. 3.2 µL of Laemmli (5x) was then added and the samples were placed in ice before

resolving them by 12% SDS-PAGE. When indicated, the buffer was supplemented with ATP or ADP, $MgCl_2$ and Vi.

Thermal unfolding: thermal denaturation and aggregation analysis were done by differential scanning fluorimetry using the Prometheus NT.48 instrument and analyzed using the PR.thermocontrol V2.0.4. software (Nanotemper technologies, DE). The ratio of fluorescence intensity at 350 nm/330 nm was used to determine the melting temperatures, T_m. All BmrA samples were at 2-3 mg/mL in dialysis buffer and supplemented with ATP and/or ADP, $MgCl_2$, Vi, where specified. Samples were incubated for 15 min at room temperature after the addition of ligands before analysis. T_m of deuterated WT and E504Q BmrA were measured after SANS and AUC, after three-time dilution in the SANS buffer.

Analytical Ultracentrifugation Sedimentation Velocity (AUC-SV): AUC-SV experiments were conducted in an XLI analytical ultracentrifuge (Beckman, Palo Alto, CA) using an ANTi-50 rotor, employing double channel Ti centre pieces of 3 mm optical path length equipped with sapphire windows (Nanolytics, Potsdam, Germany). Samples from the first SANS session were frozen and unfrozen before AUC-SV. The reference channel was filled with solvent without detergent. Acquisition was done at 20 °C and at 42,000 rpm (130,000 g), overnight, using 278 nm absorbance, and interference detection. Data processing and analysis were done using the programs REDATE v0.2.1 [85]. SEDFIT V 15.01b [86] from P. Schuck (NIH, Besthesda, USA), and GUSSI v1.1.0 [87] from C. Brautigam (Univ of Texas South Western, Dallas, USA), and using standard equations described in [45, 88]. Corrected s-values, s_{20w}, were calculated according to [88] considering 1 g/g of bound detergent, and taking into account d-BmrA and LMNG deuteration in 21.4% D_2O.

Size Exclusion Chromatography coupled to Light Scattering (SEC-LS): SEC-LS experiments were conducted at 4 °C on an HPLC consisting of a degasser DGU-20AD, a LC-20AD pump, an autosampler SIL20-ACHT, a communication interface CBM-20A and a UV–vis detector SPD-M20A (Shimadzu, Kyoto, Japan), a column oven XL-Therm (WynSep, Sainte Foy d'Aigrefeuille, France), a static light scattering miniDawn Treos, a dynamic light scattering DynaPro NANOSTAR, and a refractive index Optilab rEX detectors (Wyatt, Santa-Barbara, USA). The analysis was made with the software ASTRA, v5.4.3.20 (Wyatt, Santa-Barbara, USA), using standard methods. The samples of SANS second session

were stored at 4 °C 20-40 h before injection onto SEC-LS. 100, 25, and 100 µL of WT-ATP-Vi (A_{280} =0.54), K380A-Apo (A_{280} = 0.94), and K380-ATP (A_{280} =0.22), respectively, were injected at 0.5 mL min^{-1} on a Superdex 200 10/300 GL (GE Healthcare, Chicago, USA). Samples were in the SANS buffer; the elution buffer was the same but hydrogenated. Bovine serum albumin at 2 mg mL^{-1} in PBS buffer was injected as a control.

Numerical values for AUC, SEC-LS, and SANS analysis: a solvent density of 1.0594 g mL^{-1} and viscosity of 1.531 cp were measured for the SANS buffer at 20 °C using a density-meter DMA 5000 and a viscosity-meter AMVn (Anton PAAR, Graz, Austria). For BmrA, the partial specific volume, $\bar{v}$ = 0.751 mL g^{-1}, and refractive index increment, $\partial n/\partial c$ = 0.185 mL g^{-1}, were calculated from the amino-acid sequence using the program SEDFIT. The extinction coefficient of 0.586 mL mg^{-1} cm^{-1} at 280 nm is known to be only indicative. The 2-component analysis in SEC-LS provided the expected molar mass for the protein-detergent complex (see results part), but false protein molar mass (170 kDa), a point previously noticed for BmrA [45] or for the PatA/PatB multidrug transporter [89] and attributed to an erroneous value of the extinction coefficient calculated from sequence. Molecular weights in solution estimated by combining the forward intensity extracted from the Guinier plots, BmrA concentration, and scattering length density knowledge, consistent for a given protein, are larger by 10% to 50% than the theoretical value for the dimer, which we believe is related to the method used to determine protein concentrations (Table S2). For LMNG: $\bar{v}$ = 0.797 mL g^{-1}, and $\partial n/\partial c$ = 0.146 mL g^{-1} [32]. Ratio, M_D/M_H, of the mass of the molecule in 21.4 % D_2O: 1.044 and 1.045, for the 70% and 72% d- WT and d- E504Q BmrA, respectively, considering 80% of the exchangeable H exchanged in 100% D_2O, and 1.003 for LMNG, was calculated from the chemical structures and used to derive $s_{20,w}$. Numerical values for SANS are given in Table S2.

BmrA structural models for SANS analysis: two homology models were built by SWISS-MODEL [90] using crystal structures of two ABC transporters with PDB codes: 3WME and 3B5W. The histidine tag, ab-initio folded using QUARK online [91] was added to these two models, and to the OF cryo-EM structure of E504A BmrA with a PDB code 6R81.

SANS data recording: SANS curves have been recorded on D22 instrument, at Institut Laue Langevin, using a neutron wavelength $\lambda = 6$ Å ± 10% in two configurations (collimation length: sample-detector distance): (2.8 m: 1.4 m) or (2.8 m: 1.6 m), and (8 m: 8 m), which together enabled to obtain a q-range from 0.007 $Å^{-1}$ to 0.5 $Å^{-1}$. The samples were placed in 1 mm thick suprasil quartz cuvettes (Hellma, Müllheim, Germany), in a 22-position rack thermostated at 20 or 7 °C. The exposure time varied between 15 and 20 min at short detector distance and 30 to 90 min at long distance. The beam measures 40 mm x 55 mm upstream collimation and 7 mm x 10 mm at sample position. Full details are given in Table S2 according to the published guidelines [92].

SANS data reduction : data were scaled to absolute intensity I (q) in absolute scale (cm^{-1}) *vs*. q (where $q = 4\pi\sin\theta/\lambda$, 2q is the scattering angle, λ is the neutron wavelength) as follows. The neutron flux at sample position was used to calibrate scattering intensity to absolute scale. The empty beam transmission was used to set the center of the patterns and to calculate the transmission of the empty cell, the buffers, and the samples. The scattering of the piece of boron-enriched material, absorbing the totality of the beam flux, was subtracted from all other patterns because it results from ambient and electronic noise. The raw data were reduced (detector efficiency, electronic and empty cell background subtraction, angular averaging, transmission, and thickness correction) using GRASP software package developed by C. Dewhurst (https://www.ill.eu/users/support-labs-infrastructure/software-scientific-tools/grasp). The scattering curves measured at the two different configurations and covering different but overlapping q ranges were merged after respective buffer subtraction using SANS reduction macros written by S. Kline for IGOR software [93]. Using the ATSAS suite of software [94] , the resolution column and data at $q > 0.25$ $Å^{-1}$ were removed, and the q-values were expressed in nm^{-1}. For each duplicated samples with the same construct and condition, and for K380A-ATP when compared to K380A-ATP/Vi, after normalization by concentration, scattering curves were superposed within data noise. One representative SANS curve of each condition was thus selected for further analysis (Table S2).

SANS data analysis:

Classical analysis: details are given in Tables S2. SANS data have been submitted to a classical Guinier analysis using NCNR-developed IGOR Macros [93] and PRIMUS [95], to extract the radii of gyration (Rg) and the intensities scattered in the forward direction (I(0)) of all samples. Pair distance distribution functions (p(r)) were obtained using GNOM from PRIMUS and SASVIEW (https://www.sasview.org/). Then, they have been evaluated using AMBIMETER online tool [47]. Finally, the p(r) functions have been used as input for *ab initio* methods.

Ab initio modelling [48]*:* concerning the low-ambiguity WT-ATP/Mg/Vi data, DAMMIN online was run 20 times, without symmetry constraints, to collect 20 independent bead models. The 20 models being very similar and uncorrelated according to CorMap [96], they have been averaged using DAMAVER [97] and the low-occurrence pieces of the structure have been filtered out using DAMFILT [97]. The resulting model has been refined using DAMMIN locally with DAMSTART parameters, in expert mode, with 25 harmonics and 80 knots, according to the advices of C. Jeffries, and superimposed to the BmrA OF structure (PDB 6R81) using SUPCOMB [98]. Concerning the highly ambiguous data of WT-Apo and WT-ADP samples, 40 independent bead models have been generated using DAMMIN online without symmetry constraint. They were not all similar and DAMCLUST [99] classified them in 5 clusters, confirming that *ab initio* modelling is not appropriate.

Model-based modeling: to further analyze the results, we assumed that BmrA was, in these conditions, in a conformational equilibrium. We first generated a large ensemble of conformations, from the 3 BmrA structure / homology models using, first, NOLB [100] to vary the TMD opening, and, second, rrt-sampling from MULTIFOX [49], to move NBD and His-Tag positions. NOLB was used to build a series of 10 intermediates between the BmrA OF structure and IF models. Redundant and conformations with steric clashes were discarded, leading to 2 additional conformations. The first non-linear Normal mode between two rigid bodies was applied to the wide-open IF model to obtain 80 more open and more closed structures, using NOLB and an amplitude parameter of 4. One of the rigid body contained selected amino-acids of A and B chains of BmrA dimer, A1-164, B169-274 and A278-605, the remaining amino-acids constituted the hinge. 32 clash-free models were selected out. From each of the 37 models, rrt conformation sampling routine of MULTIFOX was applied using command line version

and default settings, to move the NBD and His-Tag, sampling about 200 conformations. It resulted in a total of 7006 conformations. MULTIFOX was then used to fit the experimental SANS curves with a combination of 1, 2, 3 or 4 of all these conformations, with variable proportions. The resulting models show a large range of opening between the NBDs.

Hydrogen Deuterium Exchange coupled to Mass Spectrometry (HDX-MS): HDX-MS experiments were performed using an automated HDX system coupled to a Synapt G2Si mass spectrometer from Waters™. The reactions were carried out by a Leap HDX PAL robot (Trajan, USA). Labeling was initiated by diluting 5.5 µL, of typically 15 µM protein, in 104.5 µL D_2O labeling buffer (5 mM Hepes pD 8, 50 mM NaCl, 0.01% LMNG). For the ATP/Mg/Vi- and ATP/Mg-incubated samples, the labeling buffer contained additionally 10 mM ATP, 10 mM $MgCl_2$ and 1 mM Vi or 10 mM ATP, 10 mM $MgCl_2$, respectively. Prior to labeling, the samples were incubated with the respective ligands for 15 min at room temperature. Samples were labeled for 0.5, 2, 5, 15, 30 and 60 min at 20 °C. Subsequently, the reactions were quenched by adding 22 µL of ice-cold quenching buffer to 100 µL of labelled sample at 4 °C. For the WT, the quenching buffer contained 0.5 M glycine pH 2.2, 4 M guanidine-HCl and pepsin with protein to pepsin ratio of 4:1 (wt:wt), and digestion was done for 2 min in quenching buffer before injecting 110 µL of the quenched sample into a 100 µL loop. For the K380A mutant, the quenching buffer consisted of 0.5 M glycine pH 2.2 and 8 M guanidine-HCl and digestion was done on-line at 10 °C using a pepsin column (Waters Enzymate™ BEH Pepsin Column 300Å, 5 µm, 2.1 mm X 30 mm). In both cases, the resulting peptides were desalted for three min and trapped on a C18 precolumn (Waters™ UPLC BEH C18 Vanguard Pre-column) before separating them with a C18 column (Waters™ Acquity UPLC BEH C18 column) using a linear acetonitrile gradient of 5-40% in 13 min and then four alternative cycles of 5% and 95% until 25 min. The valve position was adjusted to divert the sample after 14 min of each run from C18 column to waste to avoid contaminating the mass spectrometer with detergent. Three full kinetics were run for each condition, one after the other, to get triplicates of each timepoint. Blanks with equilibration buffer (5 mM Hepes pH 8, 50 mM NaCl) were injected after each sample injection and pepsin column washed (when present) during each run with pepsin wash (1.5 M guanidine-HCl, 4% acetonitrile, 0.8% formic acid pH 2.5) to minimize the carryover.

Electrospray ionization Mass spectra were acquired in positive mode in the m/z range of 50−2000 and with a scan time of 0.3 s. For the identification of non-deuterated peptides, data were collected in MS^E mode and the resulting peptides were identified using PLGS™ software (ProteinLynx Global SERVER 3.0.2 from Waters™). Deuterated peptides were identified and analyzed using DynamX 3.0 software (Waters™), using the following parameters: minimum products per amino acid of 0.3 for WT BmrA and 0.2 for K380A BmrA and file threshold of 3 out of 7 for WT BmrA and 2 out of 5 for K380A BmrA. Deuteros 2.0 software [101] was used for data visualization and statistical analysis. The online web application HDX-Viewer [102] and PyMOL (The PyMOL Molecular Graphics System, Version 2.3.0 Schrödinger, LLC) were used to represent the HDX-MS data on either the IF model of BmrA based on PDB 3WME, or the OF structure of E504A BmrA (PDB 6R81). The program MODELLER [103] was used to make the IF model of BmrA based on P-gp (PDB identity code 3WME).

QUANTIFICATION AND STATISTICAL ANALYSIS: the program 'Deuteros' was used to assess the significance of the deuteration level of peptides generated by HDX-MS. Hybrid significance test with confidence interval of 98% and p-value<0.02 was used [104].

KEY RESOURCES TABLE

REAGENT or RESOURCE	SOURCE	IDENTIFIER

Bacterial and Virus Strains		
E. coli C41(DE3)	Sigma-Aldrich	https://www.sigmaaldrich.com/catalog/product/sigma/cmc0017?lang=fr&region=FR
Biological Samples		
Chemicals, Peptides, and Recombinant Proteins		
WT BmrA	[29]	https://doi.org/10.1021/bi0362018
E504Q BmrA	[39]	https://doi.org/10.1074/jbc.M308268200
K380A BmrA	[35]	https://doi.org/10.1021/bi702303s
d- WT BmrA	This manuscript	
d- E504Q BmrA	This manuscript	
d- K380A BmrA	This manuscript	
ADP	Sigma-Aldrich	A2754
Agar	Sigma-Aldrich	A7002
Ampicillin	Euromedex	EU0400-C
ATP	Sigma-Aldrich	10519979001
Deuterated minimal media	[82, 83]	https://doi.org/10.1007/s00249-016-1186-2 https://doi.org/10.1016/bs.mie.2015.11.001
Dithiothreitol (DTT)	Sigma-Aldrich	D0632
DNAse 1	Roche	10104159001

D_2O	Euriso-top	D216L
Ethylenediaminetetraacetic acid (EDTA)	Sigma-Aldrich	E9884
Glycerol	Euromedex	EU3550
Hepes	Sigma-Aldrich	H3375
Imidazole	Sigma-Aldrich	56750
Kanamycine	Euromedex	UK0010
Lactate dehydrogenase	Roche	10107085001
Laemmli buffer 5x	[105]	https://doi.org/10.1038/227680a0
LB media	Sigma-Aldrich	L3022
LMNG	Anatrace	NG310
Lysozyme	Sigma-Aldrich	L6876
Magnesium Chloride	Sigma-Aldrich	M8266
NADH	Roche	10128023001
NaOD	Eurisotop	D076Y
Pepsin	Sigma-Aldrich	P6887
Phosphoenol pyruvate	Sigma-Aldrich	P3637
Protease inhibitor cocktail	Roche	04693159001
Pyruvate kinase	Roche	10109045001
Sodium Chloride	Sigma-Aldrich	S5886
Sodium ortho-vanadate	Sigma-Aldrich	S6508
Sodium Phosphate dibasic	Sigma-Aldrich	S7907
Sodium Phosphate monobasic	Sigma-Aldrich	S8282
Sucrose	Sigma-Aldrich	S0389
Trifluoroacetic acid (TFA)	Solvants Distillation Synthese (SDS) Peypin France	
Tris base	Sigma-Aldrich	10708976001
Trypsin	Sigma-Aldrich	T1426

2 YT media	Sigma-Aldrich	Y2377
Critical Commercial Assays		
Pierce BCA protein assay kit	Thermo Fisher Scientific	23227
Deposited Data		
cryo-EM structure of E504A BmrA bound with ATP/Mg	[42]	6R81
SANS Data	This manuscript	doi.ill.fr/10.5291/ILL-DATA.BAG-8-36; doi.ill.fr/10.5291/ILL-DATA.BAG-8-37.
HDX-MS	This manuscript	PXD028663
Experimental Models: Organisms/Strains		
Oligonucleotides		
Primers to amplify *WT BmrA* gene form *pET23-bmrA*	*TataccatggcaCCAACCAAGAAACAAAAATCTAAAAGTAAATTGAA* and *CTTGTCGACCCCGGCTTT*	
Recombinant DNA		
pET23 WT bmrA	[29]	https://doi.org/10.1021/bi0362018
pET23 E504Q bmrA	[39]	https://doi.org/10.1074/jbc.M308268200
pET23 K380A bmrA	[35]	https://doi.org/10.1021/bi702303s
pET28 WT bmrA	This manuscript	

pET28 E504Q bmrA	This manuscript	
pET28 K380A bmrA	This manuscript	
Software and Algorithms		
For AUC & SEC-LS analysis		
ASTRA, v5.4.3.20	Wyatt, Santa-Barbara, USA	https://www.wyatt.com/products/software/astra.html
GUSSI	[87]	http://biophysics.swmed.edu/MBR/software.html
REDATE	[85]	http://biophysics.swmed.edu/MBR/software.html
SEDFIT	[86]	https://sedfitsedphat.nibib.nih.gov/
Software for SANS analysis		
AMBIMETER	[47]	https://doi.org/10.1107/S1399004715002576
CORMAP	[96]	https://doi.org/10.1038/nmeth.3358
DAMAVER	[97]	https://doi.org/10.1107/S0021889803000268
DAMCLUST	[99]	https://doi.org/10.1107/S0021889812007662
DAMFILT	[97]	https://doi.org/10.1107/S0021889803000268
DAMMIN	[48]	https://doi.org/10.1016/S0006-3495(99)77443-6

DAMSTART	[97]	https://doi.org/10.1107/S0021889803000268
IGOR Pro		https://www.wavemetrics.com/
GNOM	[106]	https://doi.org/10.1107/S0021889892001663
GRASP	https://www.ill.eu/users/support-labs-infrastructure/software-scientific-tools/grasp	
MULTIFOXS	[49]	https://doi.org/10.1093/nar/gkw389
NCNR-developped IGOR Macros	[93]	https://doi.org/10.1107/S0021889806035059
NOLB	[100]	https://doi.org/10.1021/acs.jctc.7b00197
PRIMUS qt V2.8.4	[95]	https://doi.org/10.1107/S0021889803012779
SASVIEW	www.sasview.org	
SUPCOMB	[98]	https://doi.org/10.1107/S0021889800014126
Swiss-model	[90]	https://doi.org/10.1093/nar/gky427
Software for HDX-MS analysis		
Deuteros	[101]	https://doi.org/10.1093/bioinformatics/btaa677
DynamX HDX Data Analysis Software 3.0	Waters corporation	https://www.waters.com

HDX Viewer	[102]	https://doi.org/10.1093/bioinformatics/btz550
ProteinLynx Global SERVER (PLGS)	Waters corporation	https://www.waters.com
Other softwares		
PR.thermocontrol V2.0.4	Nanotemper Technologies	https://nanotempertech.com/prometheus/
PyMOL	https://pymol.org	The PyMOL Molecular Graphics System, Version 2.3.0 Schrödinger, LLC
Quark web application (in silico folding of the tag)	[91]	https://doi.org/10.1002/prot.24065
UCSF Chimera	[107]	https://doi.org/10.1002/jcc.20084
Other		
4 mL100 kDa cutoff concentrator (Amicon Ultra-4)	Millipore	UFC810096

REFERENCES

1. Davidson, A.L., et al., *Structure, function, and evolution of bacterial ATP-binding cassette systems.* Microbiol Mol Biol Rev, 2008. **72**(2): p. 317-64.
2. Rees, D.C., E. Johnson, and O. Lewinson, *ABC transporters: the power to change.* Nat Rev Mol Cell Biol, 2009. **10**(3): p. 218-27.
3. Csanady, L., P. Vergani, and D.C. Gadsby, *Structure, Gating, and Regulation of the Cftr Anion Channel.* Physiol Rev, 2019. **99**(1): p. 707-738.
4. Silverton, L., M. Dean, and K. Moitra, *Variation and evolution of the ABC transporter genes ABCB1, ABCC1, ABCG2, ABCG5 and ABCG8: implication for pharmacogenetics and disease.* Drug Metabol Drug Interact, 2011. **26**(4): p. 169-79.
5. Assaraf, Y.G., et al., *The multi-factorial nature of clinical multidrug resistance in cancer.* Drug Resist Updat, 2019. **46**: p. 100645.
6. Orelle, C., K. Mathieu, and J.M. Jault, *Multidrug ABC transporters in bacteria.* Res Microbiol, 2019. **170**(8): p. 381-391.

7. Thomas, C. and R. Tampe, *Structural and Mechanistic Principles of ABC Transporters.* Annu Rev Biochem, 2020. **89**: p. 605-636.
8. Thomas, C., et al., *Structural and functional diversity calls for a new classification of ABC transporters.* FEBS Lett, 2020. **594**(23): p. 3767-3775.
9. Jardetzky, O., *Simple allosteric model for membrane pumps.* Nature, 1966. **211**(5052): p. 969-70.
10. Lewinson, O., C. Orelle, and M.A. Seeger, *Structures of ABC transporters: handle with care.* FEBS Lett, 2020. **594**(23): p. 3799-3814.
11. Jones, P.M. and A.M. George, *Mechanism of the ABC transporter ATPase domains: catalytic models and the biochemical and biophysical record.* Crit Rev Biochem Mol Biol, 2013. **48**(1): p. 39-50.
12. Higgins, C.F. and K.J. Linton, *The ATP switch model for ABC transporters.* Nat Struct Mol Biol, 2004. **11**(10): p. 918-26.
13. van der Does, C. and R. Tampe, *How do ABC transporters drive transport?* Biol Chem, 2004. **385**(10): p. 927-33.
14. Locher, K.P., *Mechanistic diversity in ATP-binding cassette (ABC) transporters.* Nat Struct Mol Biol, 2016. **23**(6): p. 487-93.
15. Moeller, A., et al., *Distinct conformational spectrum of homologous multidrug ABC transporters.* Structure, 2015. **23**(3): p. 450-460.
16. Thelot, F.A., et al., *Distinct allosteric mechanisms of first-generation MsbA inhibitors.* Science, 2021. **374**(6567): p. 580-585.
17. Ward, A., et al., *Flexibility in the ABC transporter MsbA: Alternating access with a twist.* Proc Natl Acad Sci U S A, 2007. **104**(48): p. 19005-19010.
18. Padayatti, P.S., et al., *Structural Insights into the Lipid A Transport Pathway in MsbA.* Structure, 2019. **27**(7): p. 1114-1123 e3.
19. Moradi, M. and E. Tajkhorshid, *Mechanistic picture for conformational transition of a membrane transporter at atomic resolution.* Proc Natl Acad Sci U S A, 2013. **110**(47): p. 18916-21.
20. Wen, P.C., et al., *On the origin of large flexibility of P-glycoprotein in the inward-facing state.* J Biol Chem, 2013. **288**(26): p. 19211-20.
21. Frank, G.A., et al., *Cryo-EM Analysis of the Conformational Landscape of Human P-glycoprotein (ABCB1) During its Catalytic Cycle.* Mol Pharmacol, 2016. **90**(1): p. 35-41.
22. Hofmann, S., et al., *Conformation space of a heterodimeric ABC exporter under turnover conditions.* Nature, 2019. **571**(7766): p. 580-583.
23. Hohl, M., et al., *Crystal structure of a heterodimeric ABC transporter in its inward-facing conformation.* Nat Struct Mol Biol, 2012. **19**(4): p. 395-402.
24. Hohl, M., et al., *Structural basis for allosteric cross-talk between the asymmetric nucleotide binding sites of a heterodimeric ABC exporter.* Proc Natl Acad Sci U S A, 2014. **111**(30): p. 11025-30.
25. Kim, J., et al., *Subnanometre-resolution electron cryomicroscopy structure of a heterodimeric ABC exporter.* Nature, 2015. **517**(7534): p. 396-400.
26. Liu, Y., et al., *Single-molecule fluorescence studies on the conformational change of the ABC transporter MsbA.* Biophys Rep, 2018. **4**(3): p. 153–165.
27. Clouser, A.F., Y.H. Alam, and W.M. Atkins, *Cholesterol Asymmetrically Modulates the Conformational Ensemble of the Nucleotide-Binding Domains of P-Glycoprotein in Lipid Nanodiscs.* Biochemistry, 2021. **60**(1): p. 85-94.
28. Krugel, H., et al., *Cervimycin C resistance in Bacillus subtilis is due to a promoter up-mutation and increased mRNA stability of the constitutive ABC-transporter gene bmrA.* FEMS Microbiol Lett, 2010. **313**(2): p. 155-63.
29. Steinfels, E., et al., *Characterization of YvcC (BmrA), a Multidrug ABC Transporter Constitutively Expressed in Bacillus subtilis.* Biochemistry, 2004. **43**(23): p. 7491-7502.

30. Dalmas, O., et al., *Time-Resolved Fluorescence Resonance Energy Transfer Shows that the Bacterial Multidrug ABC Half-Transporter BmrA Functions as a Homodimer.* Biochemistry, 2005. **44**(11): p. 4312-4321.
31. Mathieu, K., et al., *Functionality of membrane proteins overexpressed and purified from E. coli is highly dependent upon the strain.* Sci Rep, 2019. **9**(1): p. 2654.
32. Breyton, C., et al., *Assemblies of lauryl maltose neopentyl glycol (LMNG) and LMNG-solubilized membrane proteins.* Biochim Biophys Acta Biomembr, 2019. **1861**(5): p. 939-957.
33. Mehmood, S., et al., *Dynamics of a bacterial multidrug ABC transporter in the inward- and outward-facing conformations.* Proc Natl Acad Sci U S A, 2012. **109**(27): p. 10832-6.
34. Lacabanne, D., et al., *Flexible-to-rigid transition is central for substrate transport in the ABC transporter BmrA from Bacillus subtilis.* Commun Biol, 2019. **2**: p. 149.
35. Orelle, C., et al., *Conformational change induced by ATP binding in the multidrug ATP-binding cassette transporter BmrA.* Biochemistry, 2008. **47**(8): p. 2404-12.
36. Geourjon, C., et al., *A common mechanism for ATP hydrolysis in ABC transporter and helicase superfamilies.* Trends Biochem Sci, 2001. **26**(9): p. 539-44.
37. Priess, M., et al., *Molecular Mechanism of ATP Hydrolysis in an ABC Transporter.* ACS Cent Sci, 2018. **4**(10): p. 1334-1343.
38. Oldham, M.L. and J. Chen, *Snapshots of the maltose transporter during ATP hydrolysis.* Proc Natl Acad Sci U S A, 2011. **108**(37): p. 15152-6.
39. Orelle, C., et al., *The Conserved Glutamate Residue Adjacent to the Walker-B Motif Is the Catalytic Base for ATP Hydrolysis in the ATP-binding Cassette Transporter BmrA.* J Biol Chem, 2003. **278**(47): p. 47002-8.
40. Engen, J.R. and E.A. Komives, *Complementarity of Hydrogen/Deuterium Exchange Mass Spectrometry and Cryo-Electron Microscopy.* Trends Biochem Sci, 2020. **45**(10): p. 906-918.
41. Gabel, F., *Applications of SANS to Study Membrane Protein Systems.* Adv Exp Med Biol, 2017. **1009**: p. 201-214.
42. Chaptal, V., et al., *Substrate-bound and substrate-free outward-facing structures of a multidrug ABC exporter.* Sci Adv, 2022. **8**(4): p. eabg9215.
43. Jacrot, B. and G. Zaccai, *Determination of molecular weight by neutron scattering.* Biopolymers, 1981. **20**: p. 2413-2426.
44. Rambo, R.P. and J.A. Tainer, *Accurate assessment of mass, models and resolution by small-angle scattering.* Nature, 2013. **496**(7446): p. 477-81.
45. Le Roy, A., et al., *Sedimentation velocity analytical ultracentrifugation in hydrogenated and deuterated solvents for the characterization of membrane proteins.* Methods Mol Biol, 2013. **1033**: p. 219-51.
46. Kodan, A., et al., *Structural basis for gating mechanisms of a eukaryotic P-glycoprotein homolog.* Proc Natl Acad Sci U S A, 2014. **111**(11): p. 4049-54.
47. Petoukhov, M.V. and D.I. Svergun, *Ambiguity assessment of small-angle scattering curves from monodisperse systems.* Acta Crystallogr D Biol Crystallogr, 2015. **71**(Pt 5): p. 1051-8.
48. Svergun, D.I., *Restoring low resolution structure of biological macromolecules from solution scattering using simulated annealing.* Biophys J, 1999. **76**(6): p. 2879-86.
49. Schneidman-Duhovny, D., et al., *FoXS, FoXSDock and MultiFoXS: Single-state and multi-state structural modeling of proteins and their complexes based on SAXS profiles.* Nucleic Acids Res, 2016. **44**(W1): p. W424-9.
50. Oganesyan, I., C. Lento, and D.J. Wilson, *Contemporary hydrogen deuterium exchange mass spectrometry.* Methods, 2018. **144**: p. 27-42.
51. Josts, I., et al., *Conformational States of ABC Transporter MsbA in a Lipid Environment Investigated by Small-Angle Scattering Using Stealth Carrier Nanodiscs.* Structure, 2018. **26**(8): p. 1072-1079 e4.
52. Maric, S., et al., *Stealth carriers for low-resolution structure determination of membrane proteins in solution.* Acta Crystallogr D Biol Crystallogr, 2014. **70**(Pt 2): p. 317-28.

53. Borbat, P.P., et al., *Conformational Motion of the ABC Transporter MsbA Induced by ATP Hydrolysis.* PLoS Biol, 2007. **5**(10): p. e271.
54. Zou, P., M. Bortolus, and H.S. McHaourab, *Conformational cycle of the ABC transporter MsbA in liposomes: detailed analysis using double electron-electron resonance spectroscopy.* J Mol Biol, 2009. **393**(3): p. 586-97.
55. Wiseman, B., et al., *Stubborn contaminants: influence of detergents on the purity of the multidrug ABC transporter BmrA.* PLoS One, 2014. **9**(12): p. e114864.
56. Carey Hulyer, A.R., et al., *Cross-linking, DEER-spectroscopy and molecular dynamics confirm the inward facing state of P-glycoprotein in a lipid membrane.* J Struct Biol, 2020. **211**(1): p. 107513.
57. Ho, H., et al., *Structural basis for dual-mode inhibition of the ABC transporter MsbA.* Nature, 2018. **557**(7704): p. 196-201.
58. Mi, W., et al., *Structural basis of MsbA-mediated lipopolysaccharide transport.* Nature, 2017. **549**(7671): p. 233-237.
59. Seelig, A., *A general pattern for substrate recognition by P-glycoprotein.* Eur J Biochem, 1998. **251**(1-2): p. 252-61.
60. Aller, S.G., et al., *Structure of P-glycoprotein reveals a molecular basis for poly-specific drug binding.* Science, 2009. **323**(5922): p. 1718-22.
61. Li, J., K.F. Jaimes, and S.G. Aller, *Refined structures of mouse P-glycoprotein.* Protein Sci, 2014. **23**(1): p. 34-46.
62. Shapiro, A.B. and V. Ling, *Positively cooperative sites for drug transport by P-glycoprotein with distinct drug specificities.* Eur J Biochem, 1997. **250**(1): p. 130-7.
63. Martin, C., et al., *Communication between multiple drug binding sites on P-glycoprotein.* Mol Pharmacol, 2000. **58**(3): p. 624-32.
64. Marcoux, J., et al., *Mass spectrometry reveals synergistic effects of nucleotides, lipids, and drugs binding to a multidrug resistance efflux pump.* Proc Natl Acad Sci U S A, 2013. **110**(24): p. 9704-9.
65. Kopcho, N., G. Chang, and E.A. Komives, *Dynamics of ABC Transporter P-glycoprotein in Three Conformational States.* Sci Rep, 2019. **9**(1): p. 15092.
66. Hellmich, U.A., et al., *Probing the ATP hydrolysis cycle of the ABC multidrug transporter LmrA by pulsed EPR spectroscopy.* J Am Chem Soc, 2012. **134**(13): p. 5857-62.
67. Sigoillot, M., et al., *Domain-interface dynamics of CFTR revealed by stabilizing nanobodies.* Nat Commun, 2019. **10**(1): p. 2636.
68. Tombline, G., et al., *Involvement of the "occluded nucleotide conformation" of p-glycoprotein in the catalytic pathway.* Biochemistry, 2005. **44**(38): p. 12879-86.
69. Lusvarghi, S. and S.V. Ambudkar, *ATP-dependent thermostabilization of human P-glycoprotein (ABCB1) is blocked by modulators.* Biochem J, 2019. **476**(24): p. 3737-3750.
70. Ishii, S., et al., *Boundary of the nucleotide-binding domain of Streptococcus ComA based on functional and structural analysis.* Biochemistry, 2013. **52**(15): p. 2545-55.
71. Shintre, C.A., et al., *Structures of ABCB10, a human ATP-binding cassette transporter in apo- and nucleotide-bound states.* Proc Natl Acad Sci U S A, 2013. **110**(24): p. 9710-5.
72. Li, S., et al., *Cryo-EM structure of human ABCB8 transporter in nucleotide binding state.* Biochem Biophys Res Commun, 2021. **557**: p. 187-191.
73. Lu, G., et al., *ATP hydrolysis is required to reset the ATP-binding cassette dimer into the resting-state conformation.* Proc Natl Acad Sci U S A, 2005. **102**(50): p. 17969-74.
74. Smith, P.C., et al., *ATP binding to the motor domain from an ABC transporter drives formation of a nucleotide sandwich dimer.* Mol Cell, 2002. **10**(1): p. 139-49.
75. Jones, P.M. and A.M. George, *Opening of the ADP-bound active site in the ABC transporter ATPase dimer: evidence for a constant contact, alternating sites model for the catalytic cycle.* Proteins, 2009. **75**(2): p. 387-96.
76. Wen, P.C. and E. Tajkhorshid, *Dimer opening of the nucleotide binding domains of ABC transporters after ATP hydrolysis.* Biophys J, 2008. **95**(11): p. 5100-10.

77. Dawson, R.J. and K.P. Locher, *Structure of a bacterial multidrug ABC transporter.* Nature, 2006. **443**(7108): p. 180-5.
78. Chen, J., et al., *A tweezers-like motion of the ATP-binding cassette dimer in an ABC transport cycle.* Mol Cell, 2003. **12**(3): p. 651-61.
79. Yang, Z., et al., *Interactions and cooperativity between P-glycoprotein structural domains determined by thermal unfolding provides insights into its solution structure and function.* Biochim Biophys Acta Biomembr, 2017. **1859**(1): p. 48-60.
80. Orelle, C. and J.M. Jault, *Structures and Transport Mechanisms of the ABC Efflux Pumps*, in *Efflux-Mediated Antimicrobial Resistance in Bacteria*, X.Z. Li, C.A. Elkins, and H.I. Zgurskaya, Editors. 2016, Springer. p. 73-98.
81. Perez-Riverol, Y., et al., *The PRIDE database and related tools and resources in 2019: improving support for quantification data.* Nucleic Acids Res, 2019. **47**(D1): p. D442-D450.
82. Dunne, O., et al., *Matchout deuterium labelling of proteins for small-angle neutron scattering studies using prokaryotic and eukaryotic expression systems and high cell-density cultures.* Eur Biophys J, 2017. **46**(5): p. 425-432.
83. Haertlein, M., et al., *Biomolecular Deuteration for Neutron Structural Biology and Dynamics.* Methods Enzymol, 2016. **566**: p. 113-57.
84. Signor, L. and E. Boeri Erba, *Matrix-assisted laser desorption/ionization time of flight (MALDI-TOF) mass spectrometric analysis of intact proteins larger than 100 kDa.* J Vis Exp, 2013(79).
85. Zhao, H., et al., *Recorded scan times can limit the accuracy of sedimentation coefficients in analytical ultracentrifugation.* Anal Biochem, 2013. **437**(1): p. 104-8.
86. Schuck, P., *Size-distribution analysis of macromolecules by sedimentation velocity ultracentrifugation and lamm equation modeling.* Biophys J, 2000. **78**(3): p. 1606-19.
87. Brautigam, C.A., *Calculations and Publication-Quality Illustrations for Analytical Ultracentrifugation Data.* Methods Enzymol, 2015. **562**: p. 109-33.
88. Le Roy, A., et al., *AUC and Small-Angle Scattering for Membrane Proteins.* Methods Enzymol, 2015. **562**: p. 257-86.
89. Boncoeur, E., et al., *PatA and PatB form a functional heterodimeric ABC multidrug efflux transporter responsible for the resistance of Streptococcus pneumoniae to fluoroquinolones.* Biochemistry, 2012. **51**(39): p. 7755-65.
90. Waterhouse, A., et al., *SWISS-MODEL: homology modelling of protein structures and complexes.* Nucleic Acids Res, 2018. **46**(W1): p. W296-W303.
91. Xu, D. and Y. Zhang, *Ab initio protein structure assembly using continuous structure fragments and optimized knowledge-based force field.* Proteins, 2012. **80**(7): p. 1715-35.
92. Trewhella, J., et al., *2017 publication guidelines for structural modelling of small-angle scattering data from biomolecules in solution: an update.* Acta Crystallogr D Struct Biol, 2017. **73**(Pt 9): p. 710-728.
93. Kline, S.R., *Reduction and analysis of SANS and USANS data using IGOR Pro.* J Appl Crystallogr, 2006. **39**: p. 895-900.
94. Manalastas-Cantos, K., et al., *ATSAS 3.0: expanded functionality and new tools for small-angle scattering data analysis.* J Appl Crystallogr, 2021. **54**(Pt 1): p. 343-355.
95. Konarev, P.V., et al., *PRIMUS: a Windows PC-based system for small-angle scattering data analysis.* J Appl Crystallogr, 2003. **36**: p. 1277-1882.
96. Franke, D., C.M. Jeffries, and D.I. Svergun, *Correlation Map, a goodness-of-fit test for one-dimensional X-ray scattering spectra.* Nat Methods, 2015. **12**(5): p. 419-22.
97. Volkov, V.V. and D.I. Svergun, *Uniqueness of ab initio shape determination in small-angle scattering.* J Appl Crystallogr, 2003. **36**: p. 860-864.
98. Kozin, M.B. and D.I. Svergun, *Automated matching of high- and low-resolution structural models.* J Appl Crystallogr, 2001. **34**: p. 33-41.
99. Petoukhov, M.V., et al., *New developments in the ATSAS program package for small-angle scattering data analysis.* J Appl Crystallogr, 2012. **45**(Pt 2): p. 342-350.

100. Hoffmann, A. and S. Grudinin, *NOLB: Nonlinear Rigid Block Normal-Mode Analysis Method.* J Chem Theory Comput, 2017. **13**(5): p. 2123-2134.
101. Lau, A.M., et al., *Deuteros 2.0: peptide-level significance testing of data from hydrogen deuterium exchange mass spectrometry.* Bioinformatics, 2021. **37**(2): p. 270-272.
102. Bouyssie, D., et al., *HDX-Viewer: interactive 3D visualization of hydrogen-deuterium exchange data.* Bioinformatics, 2019. **35**(24): p. 5331-5333.
103. Webb, B. and A. Sali, *Comparative Protein Structure Modeling Using MODELLER.* Curr Protoc Protein Sci, 2016. **86**: p. 2 9 1-2 9 37.
104. Hageman, T.S. and D.D. Weis, *Reliable Identification of Significant Differences in Differential Hydrogen Exchange-Mass Spectrometry Measurements Using a Hybrid Significance Testing Approach.* Anal Chem, 2019. **91**(13): p. 8008-8016.
105. Laemmli, U.K., *Cleavage of structural proteins during the assembly of the head of bacteriophage T4.* Nature, 1970. **227**(5259): p. 680-5.
106. Svergun, D.I., *Determination of the regularization parameter in indirect-transform methods using perceptual criteria.* J Appl Crystallogr, 1992. **25**(4): p. 495-503.
107. Pettersen, E.F., et al., *UCSF Chimera--a visualization system for exploratory research and analysis.* J Comput Chem, 2004. **25**(13): p. 1605-12.